

## INFORMATION TO USERS

This manuscript has been reproduced from the microfilm master. UMI films the text directly from the original or copy submitted. Thus, some thesis and dissertation copies are in typewriter face, while others may be from any type of computer printer.

**The quality of this reproduction is dependent upon the quality of the copy submitted.** Broken or indistinct print, colored or poor quality illustrations and photographs, print bleedthrough, substandard margins, and improper alignment can adversely affect reproduction.

In the unlikely event that the author did not send UMI a complete manuscript and there are missing pages, these will be noted. Also, if unauthorized copyright material had to be removed, a note will indicate the deletion.

Oversize materials (e.g., maps, drawings, charts) are reproduced by sectioning the original, beginning at the upper left-hand corner and continuing from left to right in equal sections with small overlaps. Each original is also photographed in one exposure and is included in reduced form at the back of the book.

Photographs included in the original manuscript have been reproduced xerographically in this copy. Higher quality 6" x 9" black and white photographic prints are available for any photographs or illustrations appearing in this copy for an additional charge. Contact UMI directly to order.

# UMI

A Bell & Howell Information Company  
300 North Zeeb Road, Ann Arbor MI 48106-1346 USA  
313/761-4700 800/521-0600



## **NOTE TO USERS**

**The original manuscript received by UMI contains pages with slanted print. Pages were microfilmed as received.**

**This reproduction is the best copy available**

**UMI**



# Phenomenological Separation in a Three-Phase Hydrocyclone

by

Robert M.M. Changirwa

A Thesis Submitted to the  
Faculty of Engineering  
in Partial Fulfilment of the Requirements  
for the Degree of

DOCTOR OF PHILOSOPHY

Major Subject: Mining Engineering

APPROVED:

  
Dr. M.C. Rockwell, Supervisor

  
Dr. D.H. Zou

  
Dr. M. Rahman

  
Dr. Hani S. Mitri, External Examiner, McGill University

TECHNICAL UNIVERSITY OF NOVA SCOTIA

Halifax, Nova Scotia

1997



**National Library  
of Canada**

**Acquisitions and  
Bibliographic Services**

**395 Wellington Street  
Ottawa ON K1A 0N4  
Canada**

**Bibliothèque nationale  
du Canada**

**Acquisitions et  
services bibliographiques**

**395, rue Wellington  
Ottawa ON K1A 0N4  
Canada**

*Your file Votre référence*

*Our file Notre référence*

**The author has granted a non-exclusive licence allowing the National Library of Canada to reproduce, loan, distribute or sell copies of this thesis in microform, paper or electronic formats.**

**The author retains ownership of the copyright in this thesis. Neither the thesis nor substantial extracts from it may be printed or otherwise reproduced without the author's permission.**

**L'auteur a accordé une licence non exclusive permettant à la Bibliothèque nationale du Canada de reproduire, prêter, distribuer ou vendre des copies de cette thèse sous la forme de microfiche/film, de reproduction sur papier ou sur format électronique.**

**L'auteur conserve la propriété du droit d'auteur qui protège cette thèse. Ni la thèse ni des extraits substantiels de celle-ci ne doivent être imprimés ou autrement reproduits sans son autorisation.**

0-612-31520-7

**Canada**

TECHNICAL UNIVERSITY OF NOVA SCOTIA LIBRARY


"AUTHORITY TO DISTRIBUTE MANUSCRIPT THESIS"

Title:

**Phenomenological Separation in a Three-Phase Hydrocyclone**

The above library may make available or authorize another library to make available individual photo/microfilm copies of this thesis without restrictions.

Name of Author: Robert M.M. Changirwa

Signature of Author:  \_\_\_\_\_

Date: April 9, 1998

## TABLE OF CONTENTS

TABLE OF CONTENTS	iii
LIST OF TABLES	vi
LIST OF FIGURES	vii
LIST OF ABBREVIATIONS AND SYMBOLS	ix
DEFINITION OF TERMS	xii
ACKNOWLEDGEMENTS	xiii
ABSTRACT	xiv
1.0 INTRODUCTION	1
1.1 Objectives and Scope of Study	3
1.2 Possible Industrial Applications	5
1.3 A Three-Phase Hydrocyclone	6
1.3.1 Development	7
1.4 Research Methodology	8
1.5 Structure of Study	9
1.6 Literature Review	9
1.6.1 Theoretical Models	10
1.6.2 Experimental Models	13
2.0 NON-DIMENSIONAL PERFORMANCE PARAMETERS	17
2.1 Basic Equations	17
2.2 Relation Between Parameters	19
2.3 Split Ratios in a Three-Phase Hydrocyclone	21
2.4 Prediction of Separation Efficiency	25
2.5 Feed Concentration and Flow Parameters	26
2.5.1 Pressure Drop	30
2.5.2 Computing Efficiencies and Parameters	31



3.0	MODELLING FLUID FLOW FIELD	32
3.1	Governing Equations	32
3.1.1	Vorticity-Stream Function Method	35
3.1.2	Normalizing the Primitive Equations	37
3.1.3	Turbulent Diffusion - Hsieh's Approach	38
3.2	Computational Solution Outline	40
3.2.1	Finite-Difference Formulation	43
3.2.2	Solution Grid Selection	44
3.2.3	Hopscotch Method	46
3.2.4	Successive Over-Relaxation (SOR) Method	48
3.3	Boundary Conditions	50
3.3.1	Solid Walls	51
3.3.2	Feed Flow	54
3.3.3	Outflow	56
3.3.4	Lighter - Liquid Interface Absent Air Core	57
3.3.5	Sharp Corners	58
4.0	EXPERIMENTAL WORK	60
4.1	Experimental Set-up	60
4.2	The Three-Phase Hydrocyclone Design	63
4.3	Fluid Flow Visualization	67
4.4	Test Materials	69
4.5	Experimental Procedure	70
5.0	RESULTS AND DISCUSSION	73
5.1	Separation Tests	73
5.1.1	Efficiency Data	73
5.1.2	Pressure Drop Data	77
5.2	Fluid Flow Visualization	82

5.2.1	Reverse Flow Vortex Stability . . . . .	82
5.3	Computed Velocity Spectra . . . . .	88
5.3.1	Axial Velocity Spectra . . . . .	88
5.3.2	Tangential Velocity Spectra . . . . .	88
5.3.3	Radial Velocity Spectra . . . . .	88
5.4	Droplet/Particle Size Statistical Analysis . . . . .	91
5.4.1	Microscopic Examination of Droplets/Particles . . . . .	94
5.5	Comparisons of Predicted and Experimental Results . . . . .	94
6.0	CONCLUSIONS . . . . .	99
6.1	Recommendations . . . . .	101
7.0	REFERENCES . . . . .	102
APPENDICES . . . . .		113
A	COMPUTED AND EXPERIMENTAL DATA ON DISKETTE . . . . .	113
B	FORTRAN PROGRAM FOR PERFORMANCE PARAMETERS . . . . .	114
C	DETERMINATION OF OIL AND SAND CONCENTRATIONS . . . . .	119
D	DROPLET AND PARTICLE SIZE DETERMINATION . . . . .	121
E	STATISTICAL ANALYSIS OF OIL DROPLETS AND SAND PARTICLES . . . . .	123
F	ISO-KINETIC SAMPLER . . . . .	126
G	GENERAL ORTHOGONAL COORDINATES ( $x_1, x_2, x_3$ ) . . . . .	129

## LIST OF TABLES

Table 4.1	Flow Visualization at Feed Pressure . . . . .	68
Table 4.2	Physical Properties of Test Materials . . . . .	69
Table 4.3	Sieve Analysis of Quartz Sand . . . . .	69
Table B1	Input Data for Computer Program HGF.FOR . . . . .	117
Table B2	Output Data for Computer Program HGF.FOR . . . . .	118
Table F1	Calibration of Iso-kinetic Samplers . . . . .	128

## LIST OF FIGURES

Figure 1.1	A Two-Phase (Solid-Liquid) Separation Hydrocyclone . . . . .	2
Figure 1.2	Schematic of Spiral Flow in a Three-Phase Hydrocyclone . . . . .	6
Figure 1.3	Traditional Three-Phase Separation Utilizing Dual-Stage Hydrocyclones . . . . .	8
Figure 2.1	Schematic for the Separation of a Three-Component Mixture in a Three-Phase Hydrocyclone . . . . .	20
Figure 3.1	Schematic Three-Phase Hydrocyclone Separation . . . . .	33
Figure 3.2	A Three-Phase Hydrocyclone Displaying the Co-ordinate System . . . . .	34
Figure 3.3	A Flow Chart for Computation . . . . .	42
Figure 3.4	Three-Phase Hydrocyclone Spidering . . . . .	45
Figure 3.5	Hopscotch Method . . . . .	46
Figure 4.1	Experimental Set-up for Testing the Three-Phase Hydrocyclone Design in the Current Study . . . . .	61
Figure 4.2	Three-Phase Separation Hydrocyclone Design Used in the Current Study . . . . .	64
Figure 4.3	Three-Phase Separation Hydrocyclone Conical Length/Nominal Diameter Ratios . . . . .	65
Figure 4.4	Photograph of the Physical Three-Phase Hydrocyclone . . . . .	67
Figure 4.5	Hypodermic Dye Injector . . . . .	68
Figure 4.6	Determination of Vortex Amplitude . . . . .	69
Figure 4.7	A Ten Funnel-Beaker Arrangement for Sample Gravimetric Analysis . . . . .	71
Figure 4.8	Schematic of a Laser Droplet and Particle Sizer . . . . .	72
Figure 5.1	The Effect of Inlet Flow Rate on Oil Efficiency . . . . .	74
Figure 5.2	The Effect of Feed Discharge on Three-Phase Efficiency . . . . .	75
Figure 5.3	Influence of Feed Concentration on Oil Efficiency . . . . .	76
Figure 5.4	Influence of Feed Concentration on Three-Phase Oil Efficiency . . . . .	76

Figure 5.5	Influence of Feed Concentration on Three-Phase Sand Efficiency . . .	77
Figure 5.6	Pressure Drop at Inlet Velocity of 2 m/s . . . . .	78
Figure 5.7	Pressure Drop at Inlet Velocity of 4 m/s . . . . .	79
Figure 5.8	Pressure Drop at Inlet Velocity of 6 m/s . . . . .	79
Figure 5.9	A Family of Computed Pressure Drop Coefficients in a Dilute Feed .	81
Figure 5.10	Effect of Feed Concentration on Pressure Drop Coefficients . . . . .	82
Figure 5.11	Effect of Inlet Velocity on Absolute Vortex Amplitude . . . . .	83
Figure 5.12	Operating Zones for Three-Phase Hydrocyclone . . . . .	84
Figure 5.13	Succession of Reverse Flow Vortex . . . . .	87
Figure 5.14	A Family of Computed Axial Velocity Spectra . . . . .	89
Figure 5.15	A Family of Computed Axial Velocity Spectra at $z=60$ mm . . . . .	89
Figure 5.16	A Family of Computed Tangential Velocity Spectra at $z=100$ mm . .	90
Figure 5.17	A Family of Computed Radial Velocity Spectra at $z=80$ mm . . . . .	90
Figure 5.18	The Effect of Droplet/Particle Size on Efficiency . . . . .	92
Figure 5.19	Particle Distribution in the Feed . . . . .	93
Figure 5.20	Particle Distribution in the Transflow . . . . .	93
Figure 5.21	Comparison of Experimental Efficiency Data With That of Colman .	94
Figure 5.22	Computed Underflow Pressure Drop Coefficients Compared with that of Colman at 0.6% C . . . . .	95
Figure 5.23	Computed Axial Velocity Profiles Compared with the Data of Dabir At $z = 240$ mm and $Re = 24,300$ . . . . .	96
Figure 5.24	Computed Tangential Velocity Profiles Compared with the Data of Dabir At $z = 60$ mm and $Re = 24,300$ . . . . .	97
Figure 5.25	Computed Radial Velocity Profiles Compared with the Data of Hsieh At $z = 100$ mm . . . . .	98
Figure C1	Concurrent Gravimetric Analysis of the Three-Phase Hydrocyclone Feed and Products . . . . .	120
Figure D1	A Rectangular Sample Cell for Laser Droplet/Particle Sizer . . . . .	122
Figure F1	Iso-kinetic Sampler . . . . .	127

## LIST OF ABBREVIATIONS AND SYMBOLS USED

$C$	Feed concentration by volume
$d_o$	Oil droplet size [m]
$d_s$	Solids particle size [m]
$D$	Hydrocyclone diameter [m]
$D_i$	Hydrocyclone inlet diameter [m]
$D_o$	Hydrocyclone overflow orifice diameter [m]
$D_s$	Hydrocyclone transverse orifice diameter [m]
$D_u$	Hydrocyclone underflow orifice diameter [m]
$D_c$	Hydrocyclone nominal diameter [m]
$E_{co}$	Oil centrifugal efficiency
$E_{cs}$	Solids centrifugal efficiency
$\frac{dF(x)}{dx}$	Fraction of the dispersed particles in the feed
$\frac{dF_o(x)}{dx}$	Fraction of the dispersed particles in the overflow
$\frac{dF_s(x)}{dx}$	Fraction of the dispersed particles in the transverse-flow
$\frac{dF_u(x)}{dx}$	Fraction of the dispersed particles in the underflow
$\frac{dF_r(x)}{dx}$	Fraction of the dispersed particles at mixing point during reversal flow
$F(x)$	Cumulative size distribution of dispersed phase in the feed
$F_o(x)$	Cumulative size distribution of dispersed phase in the overflow
$F_s(x)$	Cumulative size distribution of dispersed phase in the transverse
$F_u(x)$	Cumulative size distribution of dispersed phase in the underflow
$F_r(x)$	Cumulative size distribution of dispersed phase at mixing point in the separation

model

- $G_o(x)$  Grade efficiency for oil (recovery)
- $G_s(x)$  Grade efficiency for solids (recovery)
- $G_{co}(x)$  Centrifugal grade efficiency for oil
- $G_{cs}(x)$  Centrifugal grade efficiency for solids
- $k$  Volume fraction of the dispersed phase in the feed
- $k_o$  Volume fraction of the oil-dispersed phase in the overflow
- $k_s$  Volume fraction of the sand-dispersed phase in the transverse-flow
- $k_u$  Volume fraction of either oil or sand dispersed phase in the underflow
- $k_r$  Volume fraction of the dispersed at mixing point in the separation model
- $L$  Hydrocyclone length [m]
- $L_s$  Hydrocyclone swirl chamber length [m]
- $L_\alpha$  Hydrocyclone length of 1st taper section [m]
- $L_\beta$  Hydrocyclone length of 2nd taper section [m]
- $L_u$  Hydrocyclone length of the cylindrical (underflow) section [m]
- $L_v$  Length of vortex finder in the two-phase separation hydrocyclone [m]
- ppm parts per million = 1mg/kg
- $P_1, P_2$  Pressure tappings at points 1 and 2 in the iso-kinetic sampler unit [mmHg]
- $Q$  Volumetric flowrate of the feed [ $m^3/s$ ]
- $Q_o$  Volumetric flowrate of the overflow [ $m^3/s$ ]
- $Q_s$  Volumetric flowrate of the transverse-flow [ $m^3/s$ ]
- $Q_u$  Volumetric flowrate of the underflow [ $m^3/s$ ]
- $R_c$  Radius of the swirl chamber [m]
- $R_r$  Transition radius at forced vortex to free vortex [m]
- $r$  Dimensionless hydrocyclone radius =  $R/R_c$
- SG Specific gravity
- $t$  Dimensionless time =  $R_c/u_i$
- $\alpha$  Angle included by first cone [degree]
- $\beta$  Angle included by the second cone [degree]

$\Lambda$	Flow split ratio
$\rho_w$	Density of the continuous phase (water) [kg/m <sup>3</sup> ]
$\rho_o$	Density of the oil-dispersed phase [kg/m <sup>3</sup> ]
$\Delta\rho$	Differential density [kg/m <sup>3</sup> ]
$\rho_s$	Density of the solids-dispersed phase [kg/m <sup>3</sup> ]
$v_i$	Inlet velocity of the feed mixture = $(4Q)/(\pi D_i^2)$ [m/s]
$\Upsilon_R$	Radial velocity [m/s]
$\Upsilon_\theta$	Tangential velocity of the continuous phase [m/s]
$\Upsilon_z$	Axial velocity [m/s]
$v_1$	Mainstream fluid velocity prior to isokinetic sampling [m/s]
$v_2$	Probe fluid velocity [m/s]
$\Delta P_{F-T}$	Pressure drop between the hydrocyclone feed and the trans-flow [bar]
$\Delta P_{F-U}$	Pressure drop between the hydrocyclone feed and the underflow [bar]



## DEFINITION OF TERMS

<b>Annulus:</b>	The space between the outer cylindrical section and the interior chest of the hydrocyclone at the intersection of the taper and the cylindrical sections.
<b>Dispersed phase:</b>	Oil or sand dispersion in water.
<b>Droplet size:</b>	The diameter of an oil droplet.
<b>Hybridization:</b>	Geometrical union of two hydrocyclone designs, performing two different functions, to achieve a single hydrocyclone design for all the functions.
<b>Hybrid:</b>	The result of hybridization of the two two-phase hydrocyclone designs.
<b>Mixing point:</b>	Point at the underflow where reversal flow takes place and mixing of the fine particles from the inner and outer vortices.
<b>Particle size:</b>	The spherical diameter or equivalent diameter of a sand particle.
<b>Transverse aperture:</b>	An adjustable circumferential orifice at the intersection of the last cone and cylindrical section of the three-phase hydrocyclone.

## ACKNOWLEDGEMENTS

I take great pleasure to express my utmost gratitude to Prof. M.C. Rockwell, my supervisor, for her guidance and assistance throughout this study and in preparation of this manuscript. Not only has she been a teacher to me but a constant source of inspiration. To the members of my supervising committee, Dr. D. H. Zou, Dr. M. Rahman and Dr. H.S. Mitri, external examiner, McGill University, appreciation is expressed for their constructive comments and criticism.

My family deserves a special mention for their unfailing support, encouragement, and patience. To Shiroya, my wife, who helped with the typing, Bakoya, Kimwende and M'mbone, my daughters, I say thank you all. To my parents and mother in-law, Deina, Samuel and Susan respectively, I wish to thank them for their intercessional support.

Special mention must be given to Dr. A. Ong'iro of Chemical Engineering for his competence assistance in programming used in the current study. To the fellow graduate students of the Department of Mining and Metallurgical Engineering, P.K. Achireko, T.G. Lay, C. Ketata, L. Li and Huang for great companionship. Also included is V. Barsoum of the department for his assistance in the laboratory and typing.

The droplet/particle cumulative size distribution tests on the oil and sand were conducted by the Minerals Engineering Centre, TUNS, Halifax, Nova Scotia. I wish to thank the manager, Mr. C. Cole and his team. Thanks to Mr. Arthur Marshall who helped me to assemble the experimental set-up. The support of the departmental secretaries Karen and Heather is highly appreciated.

I wish to register my gratitude with both the governments of Kenya and Canada through CIDA programme for sponsoring part of this study. Finally, I wish to thank the Medjuck Scholarship in Energy Studies, Bruce and Dorothy Rosetti and Department of Mining and Metallurgical Engineering for financially supporting me to complete my doctoral studies.

## ABSTRACT

Recent developments in liquid-liquid and solid-liquid separation reveal that the conventional two-phase hydrocyclone is an indispensable tool in petroleum and allied industries. This is attributable to its simplicity of operation and numerous diverse applications. In spite of the many advantages it offers, the hydrocyclone suffers a major drawback in the separation of multiple-phase immiscible mixtures. Occurrence of these mixtures, as dispersions of oil and solids within liquids, can be epidemic and environmentally undesirable. In resolving this impediment, the author developed a three-phase liquid-solid-liquid separation hydrocyclone by hydrodynamically incorporating a transverse aperture into a two-phase design. Its unique aspect is that it can double function as a two-phase and a three-phase separator. The availability of this device provides potential for cost-effective concurrent treatment of oily sand-water systems in a single stage prior to reuse or disposal especially in marine environment.

Investigation into mathematical relationship between parametric and performance groups was pursued to develop a model of the three-phase hydrocyclone treating both dilute and concentrated slurry systems. An experimental program was designed to include fluid flow visualization and separation tests which were conducted on the fixed-dimension three-phase hydrocyclone. Using dye injection, the visualization tests revealed that the flows for dilute slurry system were coherent over a significant portion of the hydrocyclone axis and that negligible radial mixing occurred between the secondary and outer helical flows and vice versa for concentrated slurry system. During a stable vortex, a jet-like flow on the axis occurred from the spigot region to the overflow to a maximum amplitude of 2.65 mm. Separation tests with feed concentrations up to 2% by weight yielded a maximum efficiency of 89% for a 41- $\mu\text{m}$  oil droplet and 62% for a 46- $\mu\text{m}$  sand particle at flow split ratio range,  $\Lambda = 2.5 - 4.0$ . For the same range, an increase in feed concentration to 22% realized a maximum efficiency of 65% for a 49- $\mu\text{m}$  oil droplet and 78% for 49- $\mu\text{m}$  sand particle. Above 22% by weight of feed, sand particles bedded and plugged the transverse aperture and the spigot thereby disrupting the vortex stability and

subsequent slurry treatment. Increase in feed concentration and feed velocity enhanced sand efficiency and degenerated oil efficiency. The theoretical and experimental separation efficiency results were in good agreement. Statistical analysis showed that the droplet and particle sizes in the feed were described by lognormal and gamma distributions respectively. The Reynolds number based on the intake flow rate data ranged from 21,000 to 98,000 providing part of the input data for computation of velocity spectra.

In order to assess ultimately the performance of the three-phase hydrocyclone under different operating conditions, knowledge of the fluid velocity distribution inside the hydrocyclone was required. To determine the velocity spectra, a computational fluid dynamics approach was used. The developed Navier-Stokes equations in vorticity-stream function formulation form were identified as parabolic and elliptic. Employing Forward difference in Time and Central difference in Space (FTCS), the differential equations were converted into difference equations for numerical solution. The computed tangential velocity profiles behaved asymptotically as they approached the hydrocyclone wall yielding steep velocity gradients in that region and thus maximum effective viscosity. The computed and experimental velocity spectra results were in concordance. A unique aspect during validation of the results was that the computed and experimental tangential velocity profiles compared well better than the axial velocity profiles. This indicated that the influence of viscosity fluctuation on axial velocity distribution was much greater than that on tangential velocity distribution. Correlation between turbulence and Reynolds number was not established for vortical flows but the current study adopted the universal belief that turbulent conditions exist within the body of the hydrocyclone. In addition, the predicted and actual intake Reynolds numbers were of the order of  $10^5$  to  $10^6$  and hence the above closure applied to both turbulent and laminar flows.

## Chapter 1

### 1.0 INTRODUCTION

Several industries have employed two-phase hydrocyclones for more than fifty years. Industrial applications fall into several categories of two-phase separation with the liquid being the suspending medium: liquid clarification, slurry thickening, counter-current washing (solids washing), degassing of liquids, solids classification or sorting according to density or particle shape. Specially adapted hydrocyclones have successfully separated two immiscible liquids - oil from water, dewater light oils, and produce highly concentrated samples of a lighter dispersed phase.

A hydrocyclone is a mechanical device for separating solid, liquid, and/or gaseous phases in a dispersed suspension. Each hydrocyclone application has its particular requirements and calls for different design variables and operating conditions. Hydrocyclone operation is chiefly based on the differential density and high rotational velocities that are imparted as the suspension or slurry is injected tangentially into its upper part (see Fig. 1.1). The suspension takes on a swirling motion as it flows into the outer portion of the inverted cone. Some of the downward flow exits the hydrocyclone through the underflow while the rest reverses its vertical direction and swirls up and out of the vortex finder or overflow. Depending on the operating conditions, the swirling flow may create a region of low pressure in the center, forming a cylindrically shaped, rotating, free surface that runs the entire length of the hydrocyclone. When operating with air or one of its outlets is atmospheric, air core forms axially along the hydrocyclone and without air a lighter liquid-core forms.

Unfortunately, most industrial operations encounter numerous operations with multiple-phase systems of suspensions which necessitate the use of a more advanced separator. The author developed a three-phase separation hydrocyclone design by incorporating a two-phase hydrocyclone with a circumferential aperture, for solids removal, so that it can undertake concurrent three phase separation of liquid-solid-liquid. A three-phase hydrocyclone has demonstrated a promising separator as it is distinguished

by high effectiveness and process intensity.

In tangentially injecting immiscible mixtures into the hydrocyclone and subsequent spinning of the slurry, centrifugal forces are created. The conical section converts the inlet momentum into momenta in the component directions. This phenomenon can be described by the Navier-Stokes equations.

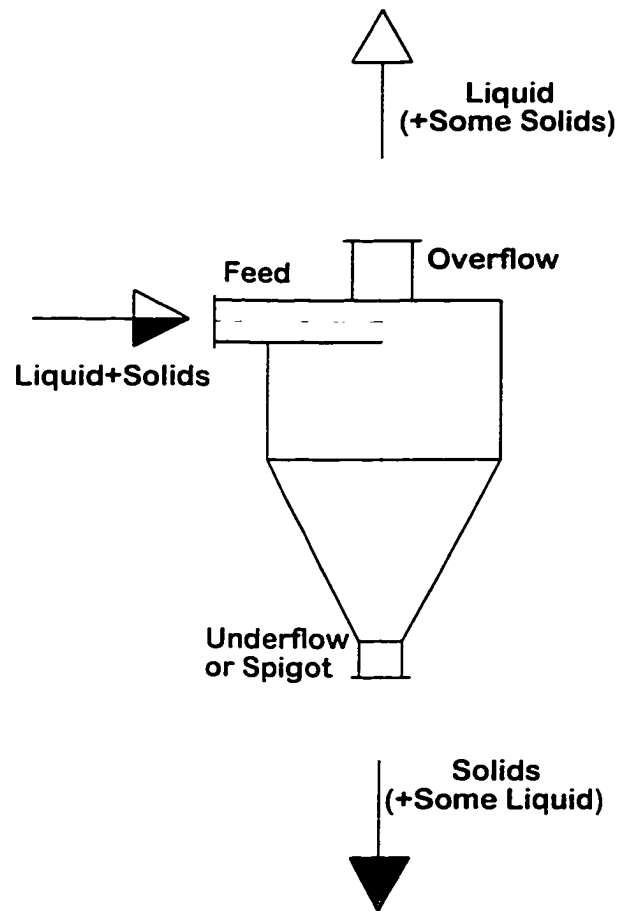


Fig. 1.1: A Two-Phase (Solid-Liquid) Separation.

Knowledge of its geometry and inlet Reynolds number can facilitate the computation of the hydrocyclone velocity components in axial, radial and tangential directions. It is therefore imperative to understand the fluid flow pattern in the three-phase hydrocyclone. Such a

model would allow design engineers to investigate the effects of changes in all dimensional variables. To the operating engineer it would provide a missing step in automating the control of closed circuit grinding systems and subsequent particle processing operations. Its advantages include simple construction and maintenance, cheaper in purchase and exploitation. The benefits translates into both capital and operating costs savings for separation of oil/solids/water mixtures in a single stage.

### 1.1 OBJECTIVES AND SCOPE OF STUDY

Abundant empiricism exists in the literature correlating design and operating conditions that influence the performance of a two-phase hydrocyclone. There is no predictive model which can provide an optimal basis for separation performance of a three-phase hydrocyclone treating high concentrations of dispersions of solids and oil in water. The performance of a three-phase hydrocyclone will be influenced by its geometrical apertures; four for three-phase and three for two-phase hydrocyclone. In addition, the separation of any three-phase immiscible mixture in the modelled hydrocyclone will be determined by its relevant physical properties, namely:

- (i) differential densities of the three components
- (ii) the feed concentrations of the dispersed phases
- (iii) the drop or particle size distributions of the dispersions
- (iv) the viscosity of the continuous medium
- (v) the viscosity and surface tension of the dispersed liquid which will determine the possible drop break-up in regions of high shear rate.

This in turn greatly affects reverse-flow vortex stability, split ratio and velocity profiles. The reverse flow vortex stability is further affected by an air core - where a hydrocyclone is operated with an air core and by a lighter-liquid core where the hydrocyclone is operated without an air core. The non-dimensional numbers such as Reynolds and Ekman do have

an impact on performance too.

The aim of the current study, therefore, is two-fold. The first objective is to mathematically and experimentally develop a description of the performance of three-phase hydrocyclone treating both dilute and concentrated slurry systems. A study of performance parameters such as vortex stability, pressure drop, dimensionless groups - split ratio, and Reynolds numbers which concentration greatly affect will be conducted. Using a hydrocyclone of fixed dimensions, a research program was designed to collect and correlate performance data as a function of measurable operating variables such as the pressure drop and feed properties. Performance criteria included the flowrates of the overflow, transflow and underflow products, their concentrations and the corresponding size distributions. In addition, fluid flow visualization tests were designed to collect data for monitoring and determining the vortex stability of the hydrocyclone.

The second objective is to mathematically develop a mathematical model for velocity spectra of fluid and dispersions based on the separation mechanics of the fluid. In tangentially injecting slurry into the hydrocyclone and subsequent spinning of the slurry, centrifugal forces are created. The conical section converts the inlet momentum into momenta in the component directions. This phenomenon can be described by the Navier-Stokes equations. Knowledge of its geometry and inlet Reynolds number can facilitate the computation of the hydrocyclone velocity components in axial, radial and tangential directions. Such a model would allow design engineers to investigate the effects of changes in all dimensional variables. To the operating engineer it would provide a missing step in automating the control of closed circuit grinding systems and subsequent particle processing operations.

The above phenomenological approach will provide a wealthier knowledge than the empirical one. The effect of geometry on classification can then be simulated elegantly in the former but impossible in the latter.



## 1.2 POSSIBLE INDUSTRIAL APPLICATIONS

The occurrence of dispersions of oil and solids impurities within liquids is widespread and environmentally undesirable. There is, often, the need to remove the dispersions of these impurities concurrently. Possible applications of the three-phase hydrocyclone in industry are enumerated in the following paragraphs.

Produced water in offshore petroleum development, normally exist as three-phase mixtures of oil and sand dispersions in water. To make it possible for reuse or disposal, this water is made clean by removal of the two phases of oil and sand. In many instances the oil is not recovered. By using a three-phase hydrocyclone this process can be effectively and practically easier.

Oil reduction platforms require efficient oil/sand/water and oil/brine separators and a hydrocyclone system to replace some of the very large separator systems in use at present would represent a considerable weight saving, thus reducing platform structural costs and may even assist in allowing the use of semi-submersibles rather than fixed plat-forms.

Treatment of industrial waste and effluent to reduce or remove concurrently concentrations of oil and solids before discharge into rivers is a similar application for the three-phase hydrocyclone. Though this form of hydrocyclone may not be used directly for dealing with major oil spills at sea, practical removal of oil and solids/oil-coated solids from the surface of the sea may include a large proportion of water and hence a simple robust compact device capable of high flow capacity. In this case a three-phase hydrocyclone, would be necessary for separating the resulting oil/solids/water mixture. A light dispersion three-phase hydrocyclone would be necessary.

Another application would be the removal of water/solids dispersions from a very dense process fluid. A company producing heavy chemicals can experience considerable problems due to the entrainment of small quantities of finely divided water drops and fine particles of solids of the order 15-20  $\mu\text{m}$  in being recirculated in a particular system, necessitating frequent shut down and cleaning of the plant. The installation of a three-

phase hydrocyclone in the system which will reduce the concentration of water and solids to below a critical level will save on the amount of fluid required in the system, increase the possible run time before shut down for necessary maintenance and improve the efficiency of the process. A heavy dispersion three-phase separation is necessary.

### 1.3 A Three-Phase Hydrocyclone

A three-phase separation hydrocyclone is used to separate a three-phase mixture into three separate streams. Unlike the two-phase hydrocyclone which has three principal apertures, the three-phase hydrocyclone has four principal apertures (see Fig.1.2). The design is derived by hybridization of the two-phase hydrocyclones, a liquid-liquid and solid-liquid details of which are found in the work by the author.<sup>4</sup> Fig. 1.2 shows a schematic of flow in a three-phase hydrocyclone design.

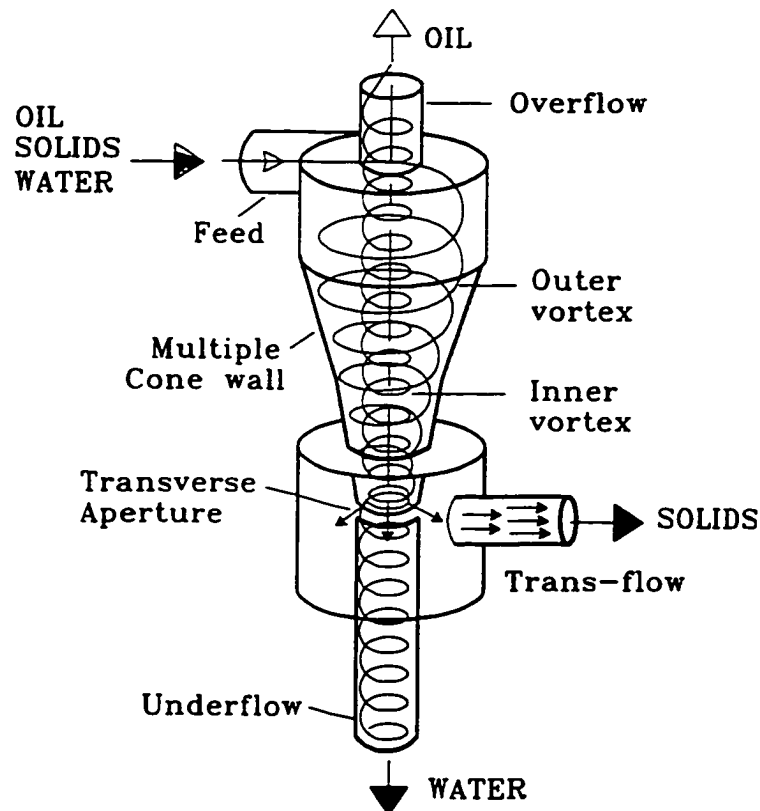


Fig. 1.2: Schematic of Spiral Flow in a Three-Phase Hydrocyclone.

The cylindrical part is closed at the top by a cover, through which the liquid overflow pipe protrudes some distance out of the hydrocyclone body. The trans-flow, which carries most of the solids, leaves through the opening in the side of the intersection of the taper and cylindrical sections. The underflow which comprises of the cylindrical section carries most of the continuous phase of the hydrocyclone. The liquid mixture enters the hydrocyclone through a tangential inlet which is either circular or rectangular in cross-section and located as near to the top cover as practical design limitations permit.

### 1.3.1 Development

Most industrial applications of hydrocyclones feature solid-liquid separation. Recently, liquid-liquid hydrocyclones have found an application in industries concerned with oily-water systems. In liquid-liquid hydrocyclones the solids which are carried over in water are not separated. Since the solids particles could be coated with oil they can not only present problems to the environment but also lower the quality of water. A second hydrocyclone or another type of separator must be used to separate the solids from water before the reuse or disposal of the water. This traditional dual-stage assembly for three-phase separation, adapted from Svarovsky<sup>3</sup>, is modified and presented in Fig. 1.3. This is a series connection of liquid-liquid and solid-liquid hydrocyclones.

The three-phase mixture of oil-solids-water is fed in the first liquid-liquid hydrocyclone and the oil separates from the overflow while the water and solids are separated from its underflow. The underflow (solids and water) is then fed to the feed of the second solid-liquid hydrocyclone through a booster pump. The booster pump is required to develop the necessary inlet velocities required to separate solids from the liquid. The liquid then separates from the overflow of the second solid-liquid hydrocyclone and the solids separate from its underflow.

The disadvantage of this assembly is its droplet/particle damage and potential danger of emulsification of the dispersed phases in the sudden steep velocity gradients in the flow as well as break-up by turbulent peak shear stresses and the pulsating flows

originating from the booster pump. Furthermore, the second stage may not guarantee a good solids efficiency so its underflow may be recycled into the feed of the first stage. This lead to the design of a single three-phase hydrocyclone which would do the work of the dual-stage hydrocyclones in a single stage.

The three-phase hydrocyclone design is derived from the evaluation of both the solid-liquid and liquid-liquid separation hydrocyclones. The design of a double-cone hydrocyclone is modified to incorporate an aperture for solids removal thus facilitating the three-phase separation of oil, solids and water. The three-phase hydrocyclone presents a potential technique for use in industry and, therefore, it is imperative that more knowledge be sought on the aspects of concurrent separation of the three phases.

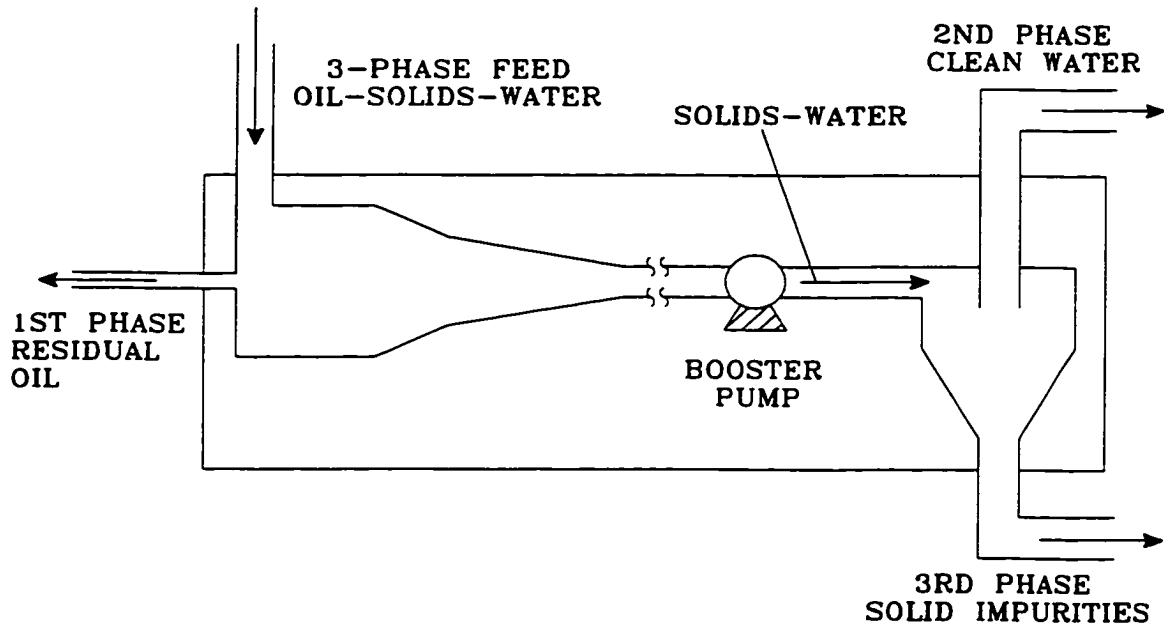


Fig. 1.3: Traditional Three-Phase Separation Utilizing Dual-Stage Hydrocyclones.

#### 1.4 Research Methodology

The main background for the current study is based on an analytical review of the theoretical and experimental models found in the literature of past and recent two-phase hydrocyclone technology and its applications.

A model-building approach with specific assumptions is used in the quantitative

analysis of three-phase hydrocyclone separation. A geometrical and hydrodynamic look at the three-phase hydrocyclone modelling and phenomenological separation, enables the development of the computational approach used to solve for velocity spectra.

Computer assisted drafting forms a base for geometrical management, design and testing of the physical model. By using various dispersions of crude oil and quartz sand in tap water, experimentation of the physical model is achieved.

### **1.5 Structure of Study**

The findings of the current study will provide knowledge and information to enable the design and operation of a hydrocyclone for three-phase separation and to evaluate its performance compared with the model developed. The model links non-dimensional numbers with the performance parameters. This is discussed in Chapter 2. Mathematical modelling for velocity spectra in the three-phase hydrocyclone is pursued. A computational fluid dynamics approach is used to determine the velocity spectra in the hydrocyclone. Employing Forward difference in Time and Central difference in Space (FTCS), the developed Navier-Stokes equations in vorticity-stream function formulation form are transformed and numerically solved. Details of the computational solution outline are found in Chapter 3.

A physical model is constructed and experimented in order to determine experimentally the aspects of performance for three-phase separation. Fluid flow visualization by dye injection is conducted. This is discussed in Chapter 4. Comparison of computed velocity spectra results is made with two experimental models. The results of the experiments are discussed in Chapter 5. Conclusive comments and recommendations for further study are given in Chapter 6.

### **1.6 Literature Review**

This review outlines mainly the progress made in the theoretical, experimental, design improvements and separation efficiencies of two-phase hydrocyclones which are

relevant to the current study. The main reason is that there is a lack of technical literature on high feed concentration and velocity spectra in a three-phase hydrocyclone. The review is categorized in two: theoretical and experimental models.

### 1.6.1 Theoretical Models

The theoretical models covered in this section aim either at simple model suitable for process simulation studies, at one particular aspect of hydrocyclone performance or to produce a detailed model of the physical interactions within the hydrocyclone by division of its interior into small sections and applying significant computational effort to balance the interactions between sections.

Many existing hydrocyclones are largely designed based on field experience rather than detailed theoretical analysis. This is not surprising because the flow field in a hydrocyclone is rather complex. Despite the complexity of the problem, simple analytical solutions that can predict the flow pattern are also very desirable from the point-of-view of simplicity and effectiveness. Rietema<sup>1</sup> and Bloor and Ingham<sup>5</sup> made early attempts at obtaining an analytical solution of the flow field in a hydrocyclone by either assuming laminar flow or inviscid flow with several other simplifying assumptions. Their work along with that of Bhattacharyya<sup>6</sup> and Upadrashta et al.<sup>7</sup> have generally aimed at one particular aspect of hydrocyclone performance. These were valuable contributions toward an understanding of the flow phenomena that govern the performance of hydrocyclones.

Lynch<sup>8</sup> and Plitt<sup>9</sup> provide examples aiming at a simple model suitable for process simulation studies. Bloor and Ingham<sup>10</sup> reported a closed-form solution for the axial swirl velocity that, despite many simplifying assumptions, compared well with the experimental results of Kelsall<sup>11</sup>.

Hwang et.al<sup>12</sup> explored and examined the underflow which was neglected by Bloor and Ingham<sup>10</sup>. They further conducted experiments on a laboratory scale, conically-shaped hydrocyclone and reported axial and tangential velocity measurements from a series of experiments that were solely devoted to the effect of underflow. As an extension of the

work of Bloor and Ingham<sup>10</sup>, they made theoretical developments with a provision for the fluid in the hydrocyclone underflow. However, in view of the simplifications employed, their usefulness in hydrocyclone design could be limited.

An optimization model for a multiple hydrocyclones separation in parallel was developed by the authors<sup>13</sup> to predict the optimum separation particle sizes, numbers of hydrocyclones and the hydrocyclones operational costs. Work on the modeling of a concurrent three-phase separation hydrocyclone was accomplished by Changirwa and Rockwell<sup>14</sup>.

Attempts by Brayshaw<sup>15</sup> and Rhodes et al.<sup>16</sup> have employed extensive computations that account for turbulence. Hsieh<sup>17</sup>, Hsieh and Rajamani<sup>18</sup> and Monredon et al.<sup>19</sup> have also used a turbulence model for calculating fluid velocities and particle trajectories in a hydrocyclone. They present comparisons between calculated and measured velocities which show good agreement. Their transport equations were formulated in terms of vorticity, stream function and angular spin (swirl) velocity using a modified Prandtl mixing length model for turbulent transport. The mixing length that they used was a function of position in the hydrocyclone.

Under practical operating conditions the flow inside a hydrocyclone may undergo several reversals before it emerges from the overflow exit as illustrated by Bradley and Pulling<sup>20</sup> and Dabir<sup>21</sup>. A simple mixing length model used to predict such a flow has a tendency to damp out these variations. The differential models of turbulence overcome this difficulty by accounting for convection and diffusion of turbulent parameters. The standard form of the *k*-model however proved inadequate for the flow. Dyakowski and Williams<sup>22</sup> attributed the above to the presence of anisotropy and the alteration of length scales caused by the presence of a high swirl velocity. They suggested that the anisotropy of turbulent viscosities is significant in hydrocyclones having diameters of the order of 44 mm or less. Typically, pulp and paper industry hydrocyclones are of the order of 75 mm.

The air core has a large effect on the flow rates to each product, and under some circumstances can even result in a zero flow to one product. Little is currently understood

about the behaviour of the air core. Hsieh and Rajamani<sup>18</sup> state, "Plausible formulations of the air core radius for hydrocyclones with wide variations in design and operating variables are almost nonexistent in the literature" and then choose the smallest air core that gave convergence in their computations. Upadrashta et al.<sup>7</sup> calculated an air core diameter but their relation omits the vortex diameter. Rhodes et al.<sup>16</sup> used multi-phase computational fluid dynamics with air as one component of the feed to obtain an air core.

Malhotra et al.<sup>23</sup> have carried out computations for turbulent flow under assumptions of axial symmetry. They developed a model that includes new formulation of the turbulence dissipation equation which was found to affect turbulence closure. The new model appears to predict correctly the behavior of a conventional water-fed hydrocyclone in the absence of an air core. So et al.<sup>24</sup> have carried out studies towards the modification of the modelled turbulence equations so that the models are applicable to low Reynolds number regions as well.

More recently, Bloor and Ingham<sup>25</sup> have studied the hydrocyclone theoretically assuming the flow to be rotational and inviscid. Their results show good agreement with those of Kelsall<sup>11</sup>. The region of viscous flow, where the azimuthal component of velocity changes from being a free vortex to solid body rotation, has also been investigated by Bloor and Ingham<sup>26</sup> who employed a viscous turbulent model based on Prandtl mixing length theory.

Recently, Kim and Chang<sup>27</sup> have carried out careful computations of a strongly swirling turbulent round jet with recirculation by an algebraic stress model that accounts for the differences between the three viscosities  $\nu_{t1}$ ,  $\nu_{t2}$ , and  $\nu_{t3}$ . They have illustrated that only a slight improvement in results is thereby obtained as compared to the standard model. The geometry developed by Malhotra et al.<sup>23</sup> was considerably more complicated than a round jet and it was felt that at that stage of development of a numerical model of a hydrocyclone, the additional sophistication was not necessary. Once confidence is acquired in the overall performance of an analytical procedure for a hydrocyclone it may be possible to incorporate the proposals of Kim and Chang<sup>27</sup>, and Dyakowski and



Williams<sup>22</sup>. It should be pointed out that even though their contribution may be small, the equations of algebraic stress modeling are algebraically involving and cumbersome. Aside from this, there is no fundamental difficulty in incorporating them in a numerical scheme because of their algebraic nature.

### 1.6.2 Experimental Models

Several authors<sup>17, 28-45</sup> have worked on the design of the hydrocyclone to enhance its efficiency for diverse applications while others like Kelsall<sup>46</sup> and Knowles<sup>47</sup> have measured the time averaged internal flow structure using an optical system. Bradley<sup>48</sup> has given comprehensive discussion of the hydrocyclone and its uses for separating more dense suspensions. At higher concentration the presence of the suspended solids affects the separation of the hydrocyclone and must be taken into account in operation Svarovsky and Marasinghe<sup>49</sup>. Sheng et al<sup>50</sup> and Bohner<sup>51</sup> have used conical hydrocyclones with oil/water mixtures of around equal proportions.

The operation of the hydrocyclone and its separation will be very different from the case of low concentrations of suspended particles that can be considered to have no interactive effect on each other or the overall flow structure. In this case the overflow and underflow will need to be of near equal proportions. In the case where the suspension is less dense than the continuous medium, for example a dispersion of oil drops in water, then, the drops will migrate towards the central axis of the hydrocyclone and be carried out through the vortex finder in the overflow stream and the underflow will become the depleted stream.

Most applications of hydrocyclones in the separation of light dispersions have been concerned with oily-water systems. The first known application<sup>52</sup> in this area was an attempt to separate water-alcohol mixtures in a 10-mm diameter hydrocyclone. Very low separation efficiencies in the order of 10 % were reported for alcohol feed fractions of about 50 % by weight.

Hitchon<sup>53</sup> used a similar hydrocyclone to separate kerosene-water mixtures and

found that it was possible to obtain one component in pure form. Either the water could be obtained pure at the underflow for high overflow split ratios, or kerosene could be obtained pure at the overflow for low overflow split ratios. However, very high feed fractions (50%) of the dispersed phase were used and a pure product in this sense probably containing some small impurities.

Further separation studies<sup>54</sup> were conducted for a white oil-water system in a 95-mm diameter hydrocyclone and results similar to those of Hitchon were obtained. They concluded that phase separation efficiency is critically dependent on dispersed phase drop size and that poor separation resulted from moderate mixing intensities at the feed inlet. Phase separation was found to be principally a function of operating conditions and not of hydrocyclone geometry. Again, high dispersed phase feed concentrations were used.

Regehr<sup>55</sup> pioneered the separation of less dense solid and liquid dispersions in water by employing variant complex geometrical designs of a hydrocyclone, based upon the circular cylinder and derived from the conical form of hydrocyclone with dispersions of polyethylene, polypropylene and oil, but the concentrations of the dispersion were high, in the range 1-30%. Thus, by using solid particles dispersed in water as a model for the liquid-liquid system, he would keep the dispersed phase size distribution fixed and investigate the influence of hydrocyclone geometry and operating variables. The designs studied appear to be the original attempts at using long hydrocyclones (length to diameter ratio  $\geq 10$ ) for this application. Both reverse-flow and through-flow designs were investigated. In his study, Regehr used the underflow purity (1 - ratio of the volume fraction of dispersed phase in the underflow to that of the feed stream) as a measure of separation efficiency. This measure reflects the ability of the separator to remove the dispersed phase from the underflow. An efficiency of 100% is reflected by the underflow containing no dispersed phase, while an efficiency of 0% represents the inlet stream being split into streams of equal composition. Regehr found that for all hydrocyclone designs tested, the underflow purity tended to reach an asymptotic value of less than 100% as either separation length or inlet velocity approached large values ( $L/D_c \geq 10$  or  $\psi \geq 8$

m/s). This result was independent of the particle size distribution or particle-fluid density differential and indicated the presence of an inefficiency common to all the designs studied. The underflow purity exhibited asymptotic behaviour as total separation length increased to which he interpreted as a decay of angular momentum at the downstream end of the hydrocyclones.

Kimber and Thew<sup>56</sup> investigated the separation of finely divided oil dispersions from water using cylindrical hydrocyclones. Using a 50-mm bore hydrocyclone they found that it was possible to concentrate up to 90% of the oil in an overflow of about 10% of the total throughput which was about 200 l/m with oil concentrations up to 1000 ppm. They conducted separation studies of oil-water mixtures in a hydrocyclone design used by Regehr<sup>55</sup>.

The above studies which were prompted by environmental concerns were continued by Colman<sup>57</sup> who conducted a series of experiments in an attempt to optimize the design of long hydrocyclones to separate very dilute mixtures of light dispersed particle. Using a combination of flow visualization, separation tests, particle size determinations, and velocity profile measurements, he arrived at an improved double-cone hydrocyclone design for light dispersion separations.

Meldrum<sup>58</sup> presented data for the double-cone hydrocyclone by Colman<sup>57</sup> which differed from the other researchers. The underflow purity exhibited a very sharp drop-off at both low and high values of inlet velocity with a constant value in between. He attributed the drop off at low inlet velocities to insufficient centrifugal forces available for separation. The decrease in underflow purity at high inlet velocities was attributed to insufficient pressure drop across the overflow orifice. The "plateau" value of underflow purity in these tests (from 90-95%) suggests the presence of a limiting factor such as the loss of dispersion directly to the underflow in a side-wall boundary layer and hence short circuit flow phenomenon.

Aspects of performance for both light and heavy dispersion hydrocyclones and their scale up criteria have been conducted by several researchers<sup>59-67</sup> while others<sup>68-75</sup> have

modelled and experimented the two-phase hydrocyclones for various industrial applications.

Hashmi et al.<sup>76</sup> using dispersions of Terra Nova crude in water achieved separation efficiencies as high as 98% in a long hydrocyclone for a mean droplet size of 10  $\mu\text{m}$ . They advocated for the removal of residual oil from the aqueous phase prior to removal of other impurities.

Bednarski and Listewnik<sup>77</sup> reported separations of a three-phase mixture of oil-solids-water in a twin inlet single cone hydrocyclone design with an included cone angle,  $\alpha = 7^\circ$ . By using oil and water mixtures with batches of solids they obtained separation efficiency of up to 80% with oil droplets  $> 40 \mu\text{m}$  while solids efficiency reached 47%. They attributed the low solids efficiency to inadequate centrifugal forces available for separation as the hydrocyclone was operated at low inlet velocities. This was done to prevent high shear field associated with oil droplet break-up.

Using a dilute feed (0.1% concentration by volume) of dispersions of Forties crude oil and quartz sand in water, the authors<sup>78</sup> tested the three-phase hydrocyclone achieving 90% oil efficiency and 58% sand efficiency for particle sizes 44  $\mu\text{m}$  and 48  $\mu\text{m}$  respectively at a transflow aperture of 6 mm. Apparently, their work did not explore the main flow field for velocity spectra. A compromise had been reached to maximize oil efficiencies at the expense of low solids efficiencies.

The solid-liquid hydrocyclones, the single-cone hydrocyclones, are relatively well known and their performance have been improved by computer modeling in recent years. Computer simulation work<sup>79</sup> on the three-phase hydrocyclone has provided insights into its main flow field.

## Chapter 2

### 2.0 Non-Dimensional Performance Parameters and Formulations

Unlike two-phase separation, three-phase separation has different non-dimensional governing performance parameters. Parameters affecting the separation in the three phase-hydrocyclone separation were discussed in detail<sup>4</sup>. Some of these parameters are utilized in this section to develop a mathematical relationships between the non-dimensional performance parameters. The three-phase hydrocyclone like any real separation equipment has limitations in its performance which can be characterized by separation efficiency. This chapter adopts some basic definitions and derived relationships between the efficiency and droplet/particle size distributions of various combinations of the feed, overflow or underflow or transverse-flow streams. The performance parameters of the three-phase hydrocyclone considered are: (1) the separation efficiency for the oil; (2) the separation efficiency for the solids; (3) the volume split and underflow ratio; (4) feed concentration; (5) pressure drop coefficients (Euler number - Eu); (6) Reynolds number; (7) Rossby number and (8) Ekman number.

### 2.1 Basic Equations

For optimum design the hydrocyclone separation<sup>2</sup> number,  $H_{50}$ , is given by;

$$H_{50} = \frac{d_{50}^2 \Delta \rho L \Delta P}{\mu \rho Q} \quad (2.1)$$

The feed flow rate,  $Q$ , of a hydrocyclone is given by;

$$Q = \frac{\pi D_i^2 v_i}{4} \quad (2.2)$$

Thus, for hydrocyclone applications, a swirl velocity is simply the intake volumetric flow rate divided by the cross sectional area of the intake:

$$v_{\theta} = \frac{Q_i}{A_i} \quad (2.3)$$

Expressing the axial velocity as a ratio of  $Q_o$  to the overflow:

$$v_z = \frac{Q_o}{A_o} \quad (2.4)$$

Expressing in terms of the velocity ratios, we obtain two dimensionless groups that determine the velocity field. The characteristic Ekman number for hydrocyclones is expressed as:

$$N_{ek} = \frac{\nu}{v_{\theta} D} \quad (2.5)$$

The characteristic length scale  $D$  is the diameter of the hydrocyclone and  $\nu$  is the kinematic viscosity of the fluid. The other is the characteristic Rossby number for hydrocyclones:

$$N_{ro} = \frac{v_z}{v_{\theta}} \quad (2.6)$$

The parameters  $v_{\theta}$  and  $v_z$  are simply the bulk mean velocities in the intake and overflow lines, respectively. The Ekman number which is equivalent to the reciprocal of Reynolds number is extremely small in most cases of interest where the primary effects of rotation are important. In this study,  $N_{ek} Re = D_i/D = 0.3$ . For example, with  $Re = 25,000$ ,  $N_{ek} = 1.2 \times 10^{-5}$ . The Rossby number, however, varies from zero to unity depending on the split ratio  $S = Q_o/Q$ . From Eqs. 2.3 and 2.5 Rossby number relates to  $S$  as:

$$N_{ro} = \frac{A}{A_o} \frac{Q_o}{Q} = \frac{A}{A_o} S \quad (2.7)$$

Eq.2.7 can be re-expressed as:

$$N_{ro} = \frac{A}{A_o} \left( \frac{Q_o}{Q_u} \right) \cdot \left( \frac{Q_u}{Q} \right) \quad (2.8)$$

In the current study  $A/A_o = 6.3$ . The feed Reynolds number is given by:

$$Re = \frac{D_i v}{\nu} \quad (2.9)$$

The pressure drop at  $Re_i > 5000$  is given by:<sup>2,3</sup>

$$\Delta P = \frac{aRe^b \rho v_i^2}{2} \quad (2.10)$$

where in the current study:  $a = 0.093$   $b = 0.3748$ . The Reynolds intake number is very important as it determines the velocity profiles, i.e., the momentum of the feed flow is distributed into the tangential, axial and radial directions.

## 2.2 Relations Between The Parameters

The modelling is limited to mixtures of three immiscible components/liquids for which the density of the mixture can be expressed as a linear combination of the component densities. The following assumptions are used in the model:

- 1) All flows are subjected to the centrifugal field.
- 2) The separation is isothermal or has negligible temperature rise.
- 3) The separation process occurs at steady state, with no agglomeration or comminution of dispersed phase particles occurring in the three-phase hydrocyclone.
- 4) The droplets or particles of the dispersed phases are assumed to have a distribution of sizes.

With the above assumptions, a single-stage concurrent three-phase separation hydrocyclone can be schematically drawn as in Fig. 2.1. The total flowrate of the feed must be equal to the sum of the total flowrates of the overflow, transverse-flow and underflow if there is no accumulation of material in the separator. The material balance equation for the total flowrates,  $Q$ ,  $Q_o$ ,  $Q_s$  and  $Q_u$  representing the feed, overflow, transverse-flow and underflow respectively (see Fig. 2.1) can be written as:

$$Q = Q_o + Q_s + Q_u \quad (2.11)$$

By dividing by  $Q$ , Eq. 2.11 can be expressed in terms of flow ratios:

$$\frac{Q_o}{Q} + \frac{Q_s}{Q} + \frac{Q_u}{Q} = 1 \quad (2.12)$$

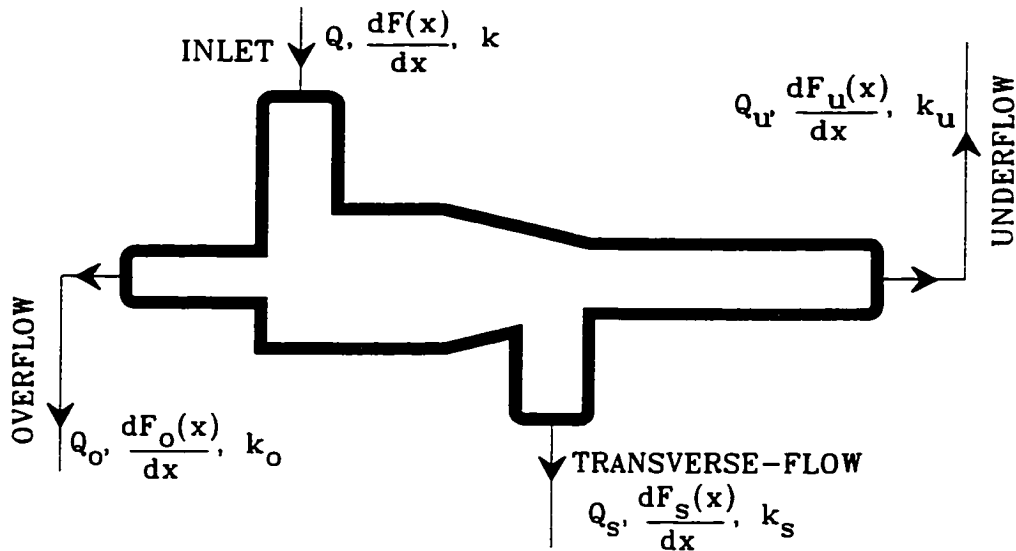


Fig. 2.1: Schematic for the Separation of a Three-Component Mixture in a Three-Phase Hydrocyclone.

Flowrate balance must also apply to any size fraction present in the feed if there is no change in particle sizes of the dispersed phases inside the hydrocyclone separator. Hence, a material balance equation for the dispersed phases can be written as:

$$kQ = k_o Q_o + k_s Q_s + k_u Q_u \quad (2.13)$$

Dividing Eq. 2.13 by  $kQ$  some very important ratios can be obtained:

$$\frac{k_o Q_o}{kQ} + \frac{k_s Q_s}{kQ} + \frac{k_u Q_u}{kQ} = 1 \quad (2.14)$$

By definition, the droplet/particle size distribution frequency gives the fraction of droplets/particles of size  $x$  in the sample. The total flowrate of droplets/particles of size  $x$  in the feed is therefore the total flowrate of the feed  $kQ$  multiplied by the fraction  $dF(x)/dx$  giving  $kQdF(x)/dx$ . Using the same analogy the total flowrates in the overflow, transverse-flow and underflow are  $k_o Q_o dF_o(x)/dx$ ,  $k_s Q_s dF_s(x)/dx$  and  $k_u Q_u dF_u(x)/dx$  respectively. Therefore, for dispersed particles in the differential size range  $dx$ , the



following component equation is valid:

$$kQ \frac{dF(x)}{dx} = k_o Q_o \frac{dF_o(x)}{dx} + k_s Q_s \frac{dF_s(x)}{dx} + k_u Q_u \frac{dF_u(x)}{dx} \quad (2.15)$$

The term  $k dF(x)/dx$  represents the volume fraction of the dispersed phase particles of size  $x$  in the feed stream and  $F(x)$ , cumulative size distribution. Likewise  $k_o dF_o(x)/dx$ ,  $k_s dF_s(x)/dx$  and  $k_u dF_u(x)/dx$  represent volume fractions of the dispersed phase particles of size  $x$  in the overflow, transverse-flow and underflow respectively. Cumulative size distribution  $F(x)$  is the density distribution and is given by:

$$f(x) = \left\{ \frac{dF(x)}{dx} \right\}_{0 \leq x \leq \infty} \quad (2.16)$$

and  $F(x)$  and  $f(x)$  are related statistically by;

$$F(x) = \int_0^{\infty} f(x) dx = 1 \quad (2.17)$$

### 2.3 Split Ratios In Three-Phase Hydrocyclone

The main parameter that an operator may wish to control, apart from the feed flowrate, is the split ratio  $\Lambda$ . This is done by using valves or restrictors in the two (overflow and underflow) outlet streams, so that the geometry must cope with a considerable range in  $\Lambda$  for many applications. Valves in the feed line, or other regions of very high shear are undesirable as they may further reduce the size distribution of the oil in the feed.

For a three-phase hydrocyclone, two types of split ratio exist. The ratio of the overflow to the underflow,  $\Lambda_o$  and the ratio of the transflow to the underflow,  $\Lambda_s$ . Mathematically they can be represented as:

$$\Lambda_o = \frac{Q_o}{Q_u} \quad (2.18)$$

$$\Lambda_s = \frac{Q_s}{Q_u} \quad (2.19)$$

Combining Eqs. 2.11, 2.18 and 2.19, we get:

$$Q_u = \frac{Q}{1 + \Lambda_o + \Lambda_s} \quad (2.20)$$

This is the fraction of the main flow that is diverted to the underflow. Likewise the fraction of the main flow that is diverted to the transflow is given by:

$$Q_s = \frac{Q\Lambda_s}{1 + \Lambda_o + \Lambda_s} \quad (2.21)$$

If there exists a condition whereby  $\Lambda_o = \Lambda_s = \Lambda$ ,

$$Q_u = \frac{Q}{1 + 2\Lambda} \quad (2.22)$$

$$Q_s = \frac{Q\Lambda}{1 + 2\Lambda} \quad (2.23)$$

For  $\Lambda = 1$ :

$$Q_u = Q_s = (1/3)Q \quad (2.24)$$

By matrix algebra Eqs. 2.11, 2.13 and 2.15 can be expressed as a product of 3 X 3 and 3 X 1 matrices to get a 3 X 1 matrix:

$$\begin{pmatrix} 1 & 1 & 1 \\ k_o & k_s & k_u \\ k_o \frac{dF_o(x)}{dx} & k_s \frac{dF_s(x)}{dx} & k_u \frac{dF_u(x)}{dx} \end{pmatrix} \cdot \begin{pmatrix} Q_o \\ Q_s \\ Q_u \end{pmatrix} = \begin{pmatrix} Q \\ kQ \\ kQ \frac{dF(x)}{dx} \end{pmatrix} \quad (2.25)$$

By Cramer's<sup>80</sup> rule the values of  $Q_o$ ,  $Q_s$ , and  $Q_u$  can be computed as following ratios of the determinants:

$$Q_o = \frac{\begin{vmatrix} Q & 1 & 1 \\ kQ & k_s & k_u \\ kQ \frac{dF(x)}{dx} & k_s \frac{dF_s(x)}{dx} & k_u \frac{dF_u(x)}{dx} \end{vmatrix}}{\begin{vmatrix} 1 & 1 & 1 \\ k_o & k_s & k_u \\ k_o \frac{dF_o(x)}{dx} & k_s \frac{dF_s(x)}{dx} & k_u \frac{dF_u(x)}{dx} \end{vmatrix}} = \frac{\begin{vmatrix} Q & 1 & 1 \\ kQ & k_s & k_u \\ kQ \frac{dF(x)}{dx} & k_s \frac{dF_s(x)}{dx} & k_u \frac{dF_u(x)}{dx} \end{vmatrix}}{A} \quad (2.26)$$

where the  $\begin{vmatrix} \end{vmatrix}$  brackets on the matrices denote their determinants and A is given by

$$A = \begin{vmatrix} 1 & 1 & 1 \\ k_o & k_s & k_u \\ k_o \frac{dF_o(x)}{dx} & k_s \frac{dF_s(x)}{dx} & k_u \frac{dF_u(x)}{dx} \end{vmatrix}$$

Therefore, Eq. 2.26 can be re-expressed as:

$$Q_o = \frac{Q}{A} \begin{vmatrix} 1 & 1 & 1 \\ k & k_s & k_u \\ k \frac{dF(x)}{dx} & k_s \frac{dF_s(x)}{dx} & k_u \frac{dF_u(x)}{dx} \end{vmatrix} \quad (2.27)$$

Likewise for  $Q_s$  and  $Q_u$ :

$$Q_s = \frac{Q}{A} \begin{vmatrix} 1 & 1 & 1 \\ k_o & k & k_u \\ k_o \frac{dF_o(x)}{dx} & k \frac{dF(x)}{dx} & k_u \frac{dF_u(x)}{dx} \end{vmatrix} \quad (2.28)$$

and the underflow discharge is:

$$Q_u = \frac{Q}{A} \begin{vmatrix} 1 & 1 & 1 \\ k_o & k_s & k \\ k_o \frac{dF_o(x)}{dx} & k_s \frac{dF_s(x)}{dx} & k \frac{dF(x)}{dx} \end{vmatrix} \quad (2.29)$$

Eqs. 2.27 - 2.29 are only valid if the following are true:

$$\begin{vmatrix} 1 & 1 & 1 \\ k_o & k_s & k_u \\ k_o \frac{dF_o(x)}{dx} & k_s \frac{dF_s(x)}{dx} & k_u \frac{dF_u(x)}{dx} \end{vmatrix} \neq 0$$

which implies that

$$k_o \neq \zeta k_s \neq \varphi k_u \quad \zeta, \varphi \text{ are real numbers}$$

$$k_o \frac{dF_o(x)}{dx} \neq \gamma k_s \frac{dF_s(x)}{dx} \neq \zeta k_u \frac{dF_u(x)}{dx} \quad \gamma, \zeta \text{ are real numbers}$$

Thus, the split ratio,  $\Lambda_o$ :

$$\Lambda_o = \frac{Q_o}{Q_u} = \frac{\begin{vmatrix} 1 & 1 & 1 \\ k & k_s & k_u \\ k \frac{dF(x)}{dx} & k_s \frac{dF_s(x)}{dx} & k_u \frac{dF_u(x)}{dx} \end{vmatrix}}{\begin{vmatrix} 1 & 1 & 1 \\ k_o & k_s & k \\ k_o \frac{dF_o(x)}{dx} & k_s \frac{dF_s(x)}{dx} & k \frac{dF(x)}{dx} \end{vmatrix}} \quad (2.30)$$

The above equation shows clearly that  $\Lambda$  depends upon the fractions of the dispersions in the intake and reporting to the overflow, underflow and transflow apertures.

## 2.4 Prediction of Separation Efficiency

The total efficiency of the dispersed phase can be defined as the ratio of the flowrate of the droplet/particles separated to the flowrate of the mixture fed into the three-phase hydrocyclone. For oil dispersion the efficiency,  $E_o$ , can be expressed as:

$$E_o = \frac{k_o Q_o}{kQ} \quad (2.31)$$

Substituting Eq. 2.2 into Eq. 2.6 we get:

$$E_o = \frac{k_o}{kA} \begin{vmatrix} 1 & 1 & 1 \\ k & k_s & k_u \\ k \frac{dF(x)}{dx} & k_s \frac{dF_s(x)}{dx} & k_u \frac{dF_u(x)}{dx} \end{vmatrix} \quad (2.32)$$

Thus, the efficiency of oil in the three-phase hydrocyclone can be expressed as a ratio of the two determinants. For the solids dispersion the efficiency,  $E_s$ , can be expressed as;

$$E_s = \frac{k_s Q_s}{kQ} \quad (2.33)$$

and in terms of matrix determinants - size distribution frequencies:

$$E_s = \frac{k_s}{kA} \begin{vmatrix} 1 & 1 & 1 \\ k_o & k & k_u \\ k_o \frac{dF_o(x)}{dx} & k \frac{dF(x)}{dx} & k_u \frac{dF_u(x)}{dx} \end{vmatrix} \quad (2.34)$$

or, if material balance in Eq. 2.14 applies Eq. 2.31 can be written as;

$$E_o = 1 - \frac{k_s Q_s}{kQ} - \frac{k_u Q_u}{kQ} \quad (2.35)$$

where concentrations in the respective streams are:

$$\frac{k_o Q_o}{kQ}, \quad \frac{k_s Q_s}{kQ}, \quad \frac{k_u Q_u}{kQ} \quad (2.36)$$

By substitution of Eqs. 2.14, 2.31, and 2.33, Eq. 2.15 can be written as:

$$\frac{dF(x)}{dx} = E_o \frac{dF_o(x)}{dx} + E_s \frac{dF_s(x)}{dx} + (1-E_o-E_s) \frac{dF_u(x)}{dx} \quad (2.37)$$

Eq. 2.37 is important because it relates the particle size distributions of the feed, the overflow, transverse-flow and the underflow. By integrating Eq. 2.37 for particle fractions between  $x_1$  and  $x_2$ , i.e.,

$$\int_{x_1}^{x_2} \frac{dF(x)}{dx} dx = E_o \int_{x_1}^{x_2} \frac{dF_o(x)}{dx} dx + E_s \int_{x_1}^{x_2} \frac{dF_s(x)}{dx} dx + (1-E_o-E_s) \int_{x_1}^{x_2} \frac{dF_u(x)}{dx} dx \quad (2.38)$$

which can be simplified as;

$$F(x_2) - F(x_1) = E_o[F_o(x_2) - F_o(x_1)] + E_s[F_s(x_2) - F_s(x_1)] + (1-E_o-E_s)[F_u(x_2) - F_u(x_1)] \quad (2.39)$$

For cumulative percentages corresponding to any size  $x$ :

$$F(x) = E_o F_o(x) + E_s F_s(x) + (1-E_o-E_s) F_u(x) \quad (2.40)$$

The material balance in Eq. 2.40 allows the determination of any one missing size distribution provided the other distributions and the total efficiencies are known. It should be noted that the cumulative percentages in Eqs. 2.39 and 2.40 can be either oversize or undersize as long as the same type is used for all the distributions in the given equation.

## 2.5. Feed Concentration and Flow Parameters

At low concentrations by volume, the individual particles are on average so far apart that they do not affect each other in their movement through the fluid. Particle separation can be achieved by putting a force on the particles which will move towards a surface where they will separate. The magnitude of the force can usually be easily expressed but the opposing particle motion, the drag force, is more difficult to establish.

The conventional way to express the drag force  $F_D$  is according to Newton:

$$F_D = C_D \cdot A \frac{\rho u_s^2}{2} \quad (2.41)$$

where  $u_s$  is the relative velocity, also known as particle slip velocity, between the fluid and the particle,  $A$  is the projected area of the particle in the motion direction and  $C_D$  is the drag coefficient.

In the current hydrocyclone the three phases namely oil, solids and water separate in the radial direction with the coarse solids being pushed to the wall - boundary layer from which the sedimenting solids are smuggled through the circumferential gap at the transverse-flow and out of the hydrocyclone. At the same time the fine oil particles or droplets migrate to the hydrocyclone axis and out to the overflow.

The relative velocities between the oil and solids, and water (carrier liquid) can be evaluated by consideration of the forces acting on a particle/droplet in equilibrium. By balancing the centrifugal force against the radial drag force ;

$$(\rho_s - \rho_m) \frac{u_\theta^2}{r} V_s = \frac{1}{2} \rho_w u_{sr}^2 \frac{\pi d^2}{4} C_D \quad (2.42)$$

Eq. 2.42 can be solved for radial drag slip velocity:

$$u_{sr} = u_\theta \sqrt{\frac{4d}{3C_D} \left( \frac{\rho_s - \rho_m}{\rho_w} \right) \frac{1}{r}} \quad (2.43)$$

where

$V_s$  = Volume of solid spherical particle =  $\pi d^3/6$

$\rho_m$  = density of the mixture

$\rho_w$  = density of the carrier liquid

$\rho_s$  = density of the solid particle

$C_D$  = drag coefficient

For coarse particles moving fast, the drag force is mostly due to the inertia of the fluid and  $C_D$  is then constant. Fine particles move more slowly and the drag force becomes

affected by viscous forces - the drag coefficient is then dependent on the particle Reynolds number  $Re_p$ , which characterises the flows round the particle. Hsieh<sup>17</sup> lists the values of  $C_D$  under three flow regimes: creeping flow regime,  $Re_p < 0.3$ ; intermediate flow regime,  $0.3 < Re_p < 500$ ; and Turbulent regime,  $500 < Re_p < 200,000$ .

$$C_D = \begin{cases} \frac{24}{Re_p} & \text{for } Re_p < 0.3 \\ \frac{18.5}{Re_p^{0.6}} & \text{for } 0.3 < Re_p < 500 \\ 0.44 & \text{for } 500 < Re_p < 200,000 \end{cases} \quad (2.44)$$

While the value  $Re_p$  is determined as:

$$Re_p = \frac{\rho_w u_{sr} d_s}{\mu} \quad (2.45)$$

Likewise, in the axial direction, the same particle experiences the downward gravitational force opposed by the upward buoyant force and the vertical drag force:

$$(\rho_s - \rho_m)g \frac{\pi d^3}{6} = \frac{1}{2} \rho_w u_{sz}^2 \frac{\pi d^2}{4} C_D \quad (2.46)$$

Eq. 2.46 can be solved for the axial drag slip velocity:

$$u_{sz} = \sqrt{\frac{4d}{3C_D} \left( \frac{\rho_s - \rho_m}{\rho_w} \right) g} \quad (2.47)$$

Eqs. 2.43 and 2.47 are important in that they combine with the component liquid velocity profiles to obtain particle velocity profiles and is covered in Chapter 3. Comparison of Eqs. 2.43 and 2.47 shows that unlike the axial slip velocity, the radial slip velocity is dependent on the tangential velocity and radial position.

With an increasing solids concentration in the suspension, the distances between the particles are reduced and particles begin to interfere with each other. If the particles are



not distributed uniformly throughout the suspension, the overall effect may be a net increase in the settling velocity because the return flow due to volume displacement will predominate in the particle-sparse regions. This is known as cluster formation and the effect is only significant in nearly mono-dispersed suspensions - those containing particles of the same size. In most practical, poly-dispersed suspensions clusters do not survive for long enough to affect the settling behaviour and the settling rate declines with increasing concentration due to the return flow being more uniformly distributed. This is known as hindered settling behaviour and yields an expression of the form

$$\frac{v_h}{v_t} = \xi^2 \cdot g(\xi) \quad (2.48)$$

where  $v_h$  is the hindered settling velocity of a particle,  $v_t$  is the unhindered terminal settling velocity,  $\xi$  is the volume fraction of the fluid (voidage) and  $g(\xi)$  is a voidage function which may take several forms. The ratio of  $v_h$  to  $v_t$  is known as hindrance. The most popular and widely used form of the voidage function is the Richardson and Zaki<sup>82</sup> equation:

$$g(\xi) = \xi^{2.65} \quad (2.49)$$

Davies et. al<sup>83</sup> suggested an expression in the form:

$$\frac{v_h}{v_t} = e^{(-\kappa c)} \quad (2.50)$$

where  $\kappa$  is a constant for a particular system and  $c$  is the concentration of solids by volume.

Another important expression for steady state hindered settling was developed by Barnea and Mizrahi<sup>84</sup>. This can be derived from the general equation of motion for particles settling in a finite system of constant volume. In the Stokes' regime, the hindered settling velocity is:

$$\frac{v_h}{v_t} = \frac{(1-c)^2}{(1+c^{1/3}) \cdot e^{\frac{5c}{3(1-c)}}} \quad (2.51)$$

### 2.5.1 Pressure Drop

The pressure drop of hydrocyclones comprises losses due to friction and acceleration and the static radial pressure gradient. The pressure losses across a hydrocyclone are a direct measure of the operating costs of the device. The performance of the hydrocyclone depends on the purity of the three streams and the pressure drop. The dimensionless groups chosen to represent the losses are the pressure drop coefficients (Euler number - Eu) and the feed Reynolds number defined as:

$$C_{pu} = \frac{P_F - P_U}{\rho v^2 / 2} \quad (2.52)$$

$$C_{po} = \frac{P_F - P_O}{\rho v^2 / 2} \quad (2.53)$$

$$C_{pt} = \frac{P_F - P_T}{\rho v^2 / 2} \quad (2.54)$$

Substituting Eq. 2.8 into Eqs. 2.52 - 2.54 we get the expressions:

$$C_{pu} = \left( \frac{2D_i^2 \Delta P_u}{\rho v^2} \right) \frac{1}{Re^2} \quad (2.55)$$

$$C_{po} = \left( \frac{2D_i^2 \Delta P_o}{\rho v^2} \right) \frac{1}{Re^2} \quad (2.56)$$

$$C_{pt} = \left( \frac{2D_i^2 \Delta P_t}{\rho v^2} \right) \frac{1}{Re^2} \quad (2.57)$$

where  $P_O$  is the wall pressure measured near the overflow orifice. When the term in the brackets, in Eqs. 2.55-2.57, is constant, the pressure loss coefficients vary inversely as the square of the Reynolds number.

### **2.5.2 Computing Efficiencies and Parameters**

A FORTRAN computer code (see Appendix B) was written to analytically compute the predicted values of oil and solid efficiencies, volume split and flow ratio, non-dimensional parameters and pressure drop coefficients. The input parameters are feed discharge and particle size distribution as obtained from the lognormal distribution.

So far the detailed flow structure in the three-phase hydrocyclone is not covered. Fluid flow modelling for velocity spectra will provide an insight into separation mechanics of the hydrocyclone. This is another phenomenological approach and is discussed in the next chapter.

## Chapter 3

### 3.0 MODELLING FLUID FLOW FIELD

This section involves building a mathematical architecture for viscous fluid flow and employing a computational fluid dynamics approach to predict the liquid-phase velocity profiles, the turbulent viscosities, the slip velocities of particles or droplets with respect to the liquid phase, and finally the particle separation performance. This task is multifarious in that the governing fluid-flow equations are non-linear, simultaneous partial differential equations, and adding to this complexity is the presence of water, oil and solids phases within the three-phase hydrocyclone. Fig. 3.1 shows the modelled hydrocyclone. The feed with dispersed phases of solid and oil enter tangentially into the cylindrical section causing a swirl flow field to develop within the unit. The separated light dispersed phase, after going through reversal flow vortex, report to the overflow. The separated dense phase goes to the boundary layer thereafter reporting to the transflow.

### 3.1 Governing Equations

Given the geometry of the hydrocyclone in Fig. 3.1 and its operating conditions, the problem is how to determine its velocity spectrum and performance. In this chapter, the equation of continuity and the momentum equations for viscous incompressible fluids will be presented without detailed derivations. For such details the reader is referred to Batchelor<sup>85</sup> and Rahman<sup>86</sup>. It will be assumed that throughout the motion of any element of fluid, its mass is conserved. This implies the volume of the fluid element must remain constant. This condition yields the equation of continuity. The momentum equations, which must be satisfied by the flow quantities at each point of the fluid, are deduced by applying the second law of motion to the fluid, which occupies an elementary volume. Figure 3.2 depicts a three-phase hydrocyclone and the cylindrical coordinate  $(R, \Theta, Z)$  with the origin at the apex of the cone.

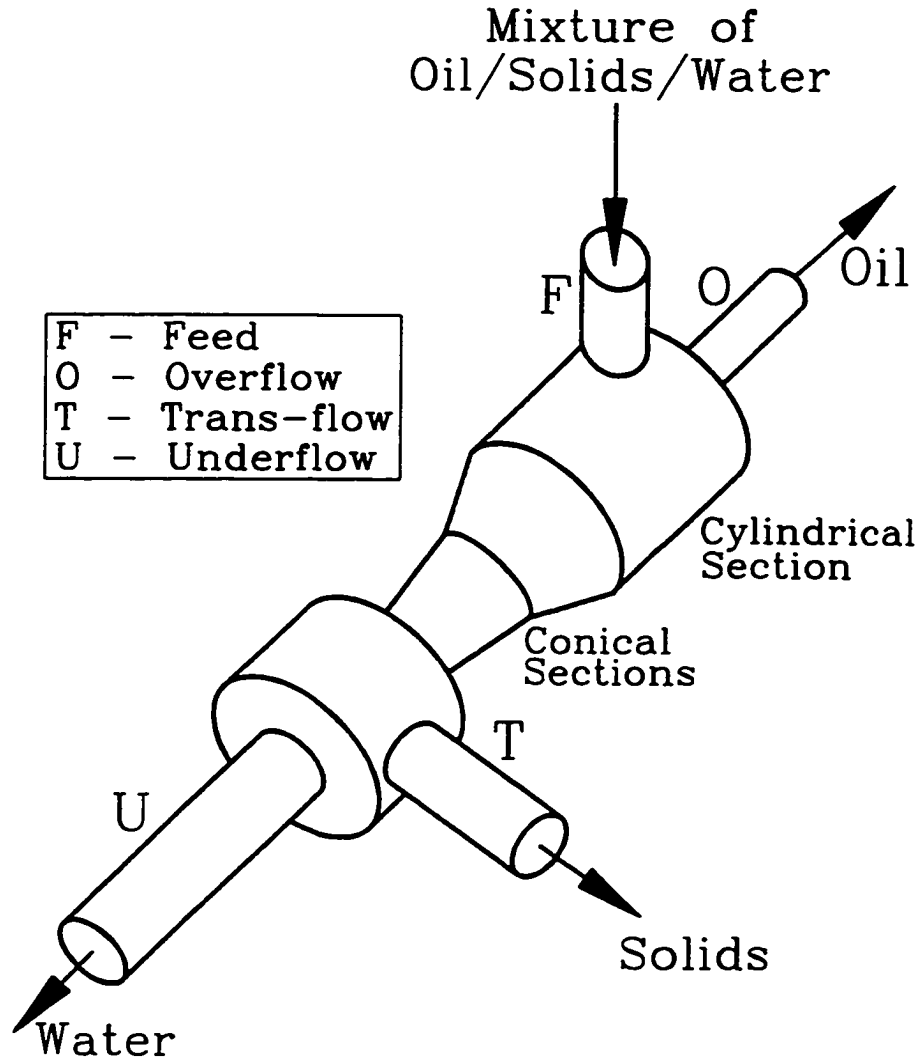


Fig. 3.1: Schematic Three-Phase Hydrocyclone Separation

The assumptions made during the modelling are: the fluid is incompressible; it has viscosity; and its flow is axi-symmetric. The corresponding velocity components are  $(\Upsilon_R, \Upsilon_\theta, \Upsilon_z)$ . The equation of conservation of mass is:

$$\frac{\partial \rho}{\partial T} + \nabla \cdot (\rho \Upsilon) = 0 \quad (3.1)$$

In consistence with the curvilinear coordinate system used here, the cylindrical coordinate form of Eq. 3.1 is

$$\frac{1}{R} \frac{\partial(\rho R \Upsilon_R)}{\partial R} + \frac{1}{R} \frac{\partial(\rho \Upsilon_\Theta)}{\partial \Theta} + \frac{\partial(\rho \Upsilon_Z)}{\partial Z} = 0 \quad (3.2)$$

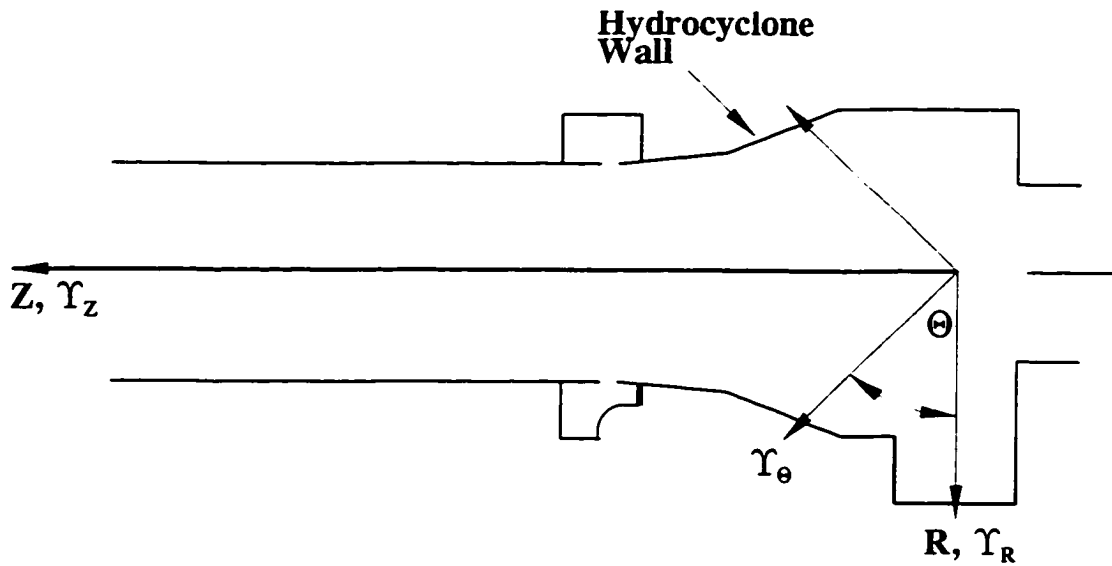


Fig. 3.2: A Three-Phase Hydrocyclone Displaying The Co-ordinate System.

The equations of motion with no body forces are:

In R-Direction

$$\frac{\partial \Upsilon_R}{\partial T} + \Upsilon_R \frac{\partial \Upsilon_R}{\partial R} + \frac{\Upsilon_\Theta}{R} \frac{\partial \Upsilon_R}{\partial \Theta} + \Upsilon_Z \frac{\partial \Upsilon_R}{\partial Z} - \frac{\Upsilon_\Theta^2}{R} = -\frac{1}{\rho} \frac{\partial P}{\partial R} + \nu \left( \nabla^2 \Upsilon_R - \frac{\Upsilon_R}{R^2} - \frac{2}{R^2} \frac{\partial \Upsilon_\Theta}{\partial \Theta} \right) \quad (3.3)$$

In \Theta-Direction

$$\frac{\partial \Upsilon_\Theta}{\partial T} + \Upsilon_R \frac{\partial \Upsilon_\Theta}{\partial R} + \frac{\Upsilon_\Theta}{R} \frac{\partial \Upsilon_\Theta}{\partial \Theta} + \Upsilon_Z \frac{\partial \Upsilon_\Theta}{\partial Z} + \frac{\Upsilon_R \Upsilon_\Theta}{R} = -\frac{1}{\rho} \frac{\partial P}{R \partial \Theta} + \nu \left( \nabla^2 \Upsilon_\Theta + \frac{2}{R^2} \frac{\partial \Upsilon_R}{\partial \Theta} - \frac{\Upsilon_\Theta}{R^2} \right) \quad (3.4)$$

In Z-Direction

$$\frac{\partial \Upsilon_z}{\partial T} + \Upsilon_R \frac{\partial \Upsilon_z}{\partial R} + \frac{\Upsilon_\theta}{R} \frac{\partial \Upsilon_z}{\partial \theta} + \Upsilon_z \frac{\partial \Upsilon_z}{\partial Z} = -\frac{1}{\rho} \frac{\partial P}{\partial Z} + \nu \nabla^2 \Upsilon_z \quad (3.5)$$

where the grad operator:

$$\nabla^2 = \frac{\partial^2}{\partial R^2} + \frac{1}{R} \frac{\partial}{\partial R} + \frac{1}{R^2} \frac{\partial^2}{\partial \theta^2} + \frac{\partial^2}{\partial Z^2} \quad (3.6)$$

The capitalized regular and Greek letters represent dimensional quantities. These equations are written in the primitive variables of velocity components,  $\Upsilon_R$ ,  $\Upsilon_\theta$ , and  $\Upsilon_z$ , and pressure,  $P$ , and the fluid properties of mass density,  $\rho$ , and kinematic viscosity,  $\nu$ . It is possible to obtain numerical solutions from Eqs. 3.2-3.5. However, most successful numerical solutions have employed the vorticity-stream method approach which will be discussed in the next section.

**3.1.1 Vorticity-Stream Function Method**

Vorticity and stream functions can be expressed in terms of velocity components. The flow field vorticity components can be introduced as follows:

In R-Direction

$$\Phi_R = -\frac{\partial \Upsilon_R}{\partial Z} \quad (3.7)$$

In  $\theta$ -Direction

$$\Phi_\theta = \frac{\partial \Upsilon_R}{\partial Z} - \frac{\partial \Upsilon_z}{\partial R} \quad (3.8)$$

In Z-Direction

$$\Phi_z = \frac{\partial(\Upsilon_R R)}{\partial R} \quad (3.9)$$

Vorticity can be regarded as the specific circulation (circulation per unit area) of the flow in the surface.

A stream function ( $\Psi$ ) can be defined to satisfy continuity in terms of the two velocity components  $\Upsilon_R$  and  $\Upsilon_Z$  for any horizontal section through the modelled hydrocyclone according to:

In R-Direction

$$\Upsilon_R = -\frac{1}{R} \frac{\partial \Psi}{\partial Z} \quad (3.10)$$

In Z-Direction

$$\Upsilon_Z = \frac{1}{R} \frac{\partial \Psi}{\partial R} \quad (3.11)$$

and angular-spin velocity

$$\Omega = \Upsilon_{\theta} R \quad (3.12)$$

By substituting Eqs. 3.10 and 3.11 into Eq. 3.8 and dropping the subscript from  $\Phi_{\theta}$ , the following vorticity-stream flow equation can be obtained:

$$\frac{\partial^2 \Psi}{\partial R^2} + \frac{\partial^2 \Psi}{\partial Z^2} - \frac{1}{R} \frac{\partial \Psi}{\partial R} + R \Phi = 0 \quad (3.13)$$

The physical significance of stream function is that lines of  $\Psi = \text{constant}$  are streamlines.

In steady flow these are the curves actually traced out by the particles of the fluid. To pursue the vorticity-stream function method, the pressure is eliminated from Eqs. 3.3 and 3.5 by cross-differentiating Eq. 3.3 with respect to Z and Eq. 3.5 with respect to R, rearranging the resultant equation with Eq. 3.2:

$$\frac{\partial \Phi}{\partial T} = \frac{1}{R^3} \frac{\partial \Omega^2}{\partial Z} + \frac{\Upsilon_R \Phi}{R} - \Upsilon_R \frac{\partial \Phi}{\partial R} - \Upsilon_Z \frac{\partial \Phi}{\partial Z} + \vartheta \left( \frac{\partial^2 \Phi}{\partial R^2} + \frac{1}{R} \frac{\partial \Phi}{\partial R} - \frac{\Phi}{R^2} + \frac{\partial^2 \Phi}{\partial \Theta^2} \right) \quad (3.14)$$



$$\frac{\partial \Omega}{\partial T} = - \left( \Upsilon_R \frac{\partial \Omega}{\partial R} + \Upsilon_Z \frac{\partial \Omega}{\partial Z} + \vartheta \left\{ \frac{\partial^2 \Omega}{\partial R^2} - \frac{1}{R} \frac{\partial \Omega}{\partial R} + \frac{\partial^2 \Omega}{\partial Z^2} \right\} \right) \quad (3.15)$$

### 3.1.2 Normalizing The Primitive Equations

The normalizing system employed in this section and elsewhere in the current study is based on the advective time scale  $R/v_i$ . The various variables in the preceding equations are converted into dimensionless form:

$$t = \frac{T}{(R_c/v_i)} \quad r = \frac{R}{R_c} \quad z = \frac{Z}{R_c} \quad v_{r,\theta,z} = \frac{\Upsilon_{R,\theta,Z}}{v_i} \quad (3.16)$$

$$\omega = \frac{\Omega}{R_c v_i} \quad \phi = \Phi \frac{R_c}{v_i} \quad Re = \frac{R_c v_i}{\vartheta} \quad \psi = \frac{\Psi}{R_c^2 v} \quad (3.17)$$

where  $Re$  is the Reynolds number. Substituting Eqs. 3.16 and 3.17 into Eqs 3.10 through 3.15 produces a normalized system of equations in conservative form:

$$\frac{\partial \phi}{\partial t} = \frac{1}{r^3} \frac{\partial \omega^2}{\partial z} - \frac{\partial(v_r \phi)}{\partial r} - \frac{\partial(v_z \phi)}{\partial z} + \frac{1}{Re} \left\{ \frac{\partial^2 \phi}{\partial r^2} + \frac{1}{r} \frac{\partial \phi}{\partial r} - \frac{\phi}{r^2} + \frac{\partial^2 \phi}{\partial z^2} \right\} \quad (3.18)$$

$$\frac{\partial^2 \psi}{\partial r^2} + \frac{\partial^2 \psi}{\partial z^2} - \frac{1}{r} \frac{\partial \psi}{\partial r} + r \phi = 0 \quad (3.19)$$

$$\frac{\partial \omega}{\partial t} = - \left( \frac{\partial(v_r \omega)}{\partial r} + \frac{v_r \omega}{r} + \frac{\partial(v_z \omega)}{\partial z} - \frac{1}{Re} \left\{ \frac{\partial^2 \omega}{\partial r^2} - \frac{1}{r} \frac{\partial \omega}{\partial r} + \frac{\partial^2 \omega}{\partial z^2} \right\} \right) \quad (3.20)$$

$$v_r = -\frac{1}{r} \frac{\partial \psi}{\partial z} \quad v_\theta = \frac{\omega}{r} \quad v_z = \frac{1}{r} \frac{\partial \psi}{\partial r} \quad (3.21)$$

Equations 3.18-3.21 are the final form of the simultaneous partial differential equations that will be solved numerically in order to obtain the velocity of the liquid phase inside the hydrocyclone. Although a correlation between turbulence and Reynolds number has not been established for vortical flows, it is generally believed that turbulent conditions exist within the body of the hydrocyclone, since the inlet Reynolds numbers are as high as  $10^5$  to  $10^6$ . However, the above closure applies to both turbulent and laminar motions. Assuming that effective viscosity is computable consisting of a laminar  $\mu_l$ , and a turbulent  $\mu_t$  component, it is necessary now to choose a suitable model for  $\mu_t$  to effect the turbulent closure.

### 3.1.3 Turbulent Diffusion - Hsieh's Approach

The overview of turbulent diffusion by Hsieh<sup>17</sup> gives a simpler definition of effective turbulent shear stress which is caused by the cross-correlation of fluctuating variables as the product of the mean velocity gradient and turbulent viscosity. Unlike  $\mu_l$ , the molecular viscosity,  $\mu_t$  is not a property of the fluid. Its value will vary from point to point in the flow, being largely determined by the structure of the turbulence at the point in question. The introduction of  $\mu_t$  provides a framework for constructing a turbulence model, but it does not itself constitute to a model, for there remains the task of expressing the turbulent viscosity in terms of known or calculable quantities. Prandtl mixing-length hypothesis employs an algebraic equation for  $\mu_t$ .<sup>17</sup> According to this hypothesis, the turbulent viscosity is equal to the local product of the density, the magnitude of the mean rate of strain, and the square of a characteristic length scale of the turbulent motion which is referred to as the mixing length,  $\iota_m$ . For nearly two-dimensional boundary flows, particularly those developing over rigid boundaries, the mixing-length hypothesis combines a good mixture of accuracy and simplicity, so good indeed that only the best of the more comprehensive simulations of turbulence can surpass it. It is therefore advisable to apply the simple algebraic mixing-length model to calculate the local effective viscosity of the slurry. The usual form of unidirectional mixing-length model is:

$$\mu_t = \rho l_m^2 \left| \frac{\partial u}{\partial y} \right| \quad (3.22)$$

The above model can be also expressed in cylindrical coordinates for swirling flows:

$$\mu_t = \rho l_m^2 \left| \frac{\partial \gamma_\theta}{\partial R} - \frac{\gamma_\theta}{R} \right| \quad (3.23)$$

In a typical hydrocyclone operation, however, the axial velocity gradient in the radial direction is of the same order of magnitude compared to the tangential-velocity gradient in the same direction. Therefore, a modified Prandtl mixing-length model, which includes the axial-velocity gradient in the algebraic expression, is proposed here to estimate the turbulent viscosity:

$$\mu_t = \rho l_m^2 \left( \left| \frac{\partial \gamma_\theta}{\partial R} - \frac{\gamma_\theta}{R} \right| + \left| \frac{\partial \gamma_z}{\partial R} \right| \right) \quad (3.24)$$

In the absence of the mixing length correlation, Pericleous et al.<sup>87</sup> used a fraction of the hydrocyclone radius as the mixing length with success. Strictly speaking, however, the turbulent mixing length varies both axially and radially inside the hydrocyclone, e.g., the mixing length is a function of position. Turbulent swirling flow through wide-angle conical diffusers<sup>88</sup> was studied enabling the solution to full Navier-Stokes equations with finite-difference method. The work, claimed as a simple turbulence model, provided realistic predictions when comparisons were made with available experimental mean axial-velocity data for flow through a 16.5° conical diffuser (area ratio = 4.4) fitted with a tailpipe. Meanwhile, Morsi and Clayton<sup>88</sup> determined the principal characteristics of turbulent swirling flow along the axisymmetric annulus formed between two coaxial tubes of different diameters but the same length. Their analysis commenced from a general statement of the Navier-Stokes in cylindrical coordinates written in a form to account for turbulent-velocity components. Both mixing-length and  $\kappa$ - $\epsilon$  models were then examined, and good agreement between theory and experiment in respect of velocity profiles was

obtained. Therefore, in the current model the expressions for the mixing length in axial and tangential directions are:

$$l_{mz} = k_1 \left( \frac{R}{R_c} \right)^{\frac{1}{4}} \left( \frac{r}{R_c} \right)^{\frac{1}{2}} \quad (3.25)$$

$$l_{m\theta} = k_2 \left( \frac{R}{R_c} \right)^{\frac{1}{4}} \left( \frac{r}{R_c} \right)^{\frac{1}{2}} \quad (3.26)$$

where  $k_1$  and  $k_2$  are constants, and  $R$  is the radius of the hydrocyclone at the horizontal level in question. It should also be noted, at this juncture, that the  $\kappa$ - $\epsilon$  model, in which two differential equations are used to describe the turbulence energy per unit mass,  $\kappa$ , and the dissipation rate of turbulence energy per unit mass,  $\epsilon$ , can not be used to calculate the local effective viscosity of the fluid in this particular application since anisotropy is imposed by swirling.<sup>17</sup>

### 3.2 Computational Solution Outline

Here the numerical problem is a set of coupled parabolic and elliptic partial differential equations. Eqs. 3.18 and 3.20 are parabolic, and they pose a "marching" or initial-value problem, wherein the solution is stepped out from some initial condition. These equations are solved using the Hopscotch method are detailed by Roache<sup>88</sup>. Eq. 3.19 is elliptic, i.e., it poses a "jury" to boundary-value problem, which is solved by the successive over-relaxation (SOR) method comprehensively discussed by Roache.

Equations (3.18) - (3.21) are converted from differential equations into difference equations following FTCS techniques (forward difference in time and central difference in space). However, due to stability consideration, donor cell differencing<sup>88</sup> is used for advection terms. Then, the hydrocyclone is overlaid with a finite-difference mesh. At the mesh intersections (node points or mesh points), the finite-difference solution is defined.

The solution starts with the establishment of initial values of  $\psi$ ,  $\phi$ ,  $\omega$ ,  $v_r$  and  $v_z$  everywhere at  $t=0$ . Then the computational cycle begins as the vorticity transport equation (Eq. 3.18) is used to calculate an approximation to  $\partial\phi/\partial t$  at all interior points. The values of  $\phi$  are calculated at the next time increment by marching the vorticity transport equation forward in time. The next step in the computational cycle is to solve the Poisson equation (Eq. 3.19) for new values of stream function  $\psi$ , using the recently calculated values of  $\phi$  in the source term of Eq. (3.18). The solution of  $\psi$  does not depend upon the boundary values of  $\phi$ , which are not yet known. This solution for new  $\psi$  is itself iterative, which means that the  $\psi$  iteration is nested within the overall computational cycle. Then the boundary values of  $\phi$  are calculated, which are typically dependent upon the recently computed values of  $\psi$  and  $\phi$  at interior points adjacent to boundary points. At this point, new velocity components  $v_r$  and  $v_z$  can be evaluated from the finite-difference analog of Eq. (3.21). Meanwhile, the approximation to  $\partial\omega/\partial t$  at all interior points with Eq. (3.20). The values of  $\omega$  at the increment time are calculated by marching the angular-spin velocity Eq. (3.20) forward in time. The last step in the computational cycle is to calculate the values of  $\omega$  on boundaries by the universal velocity-distribution law which has been comprehensively discussed by Roache. Then the computational cycle is repeated until the desired time is reached, or until the convergence criterion for steady state is satisfied. Schematically, the computational flow chart is illustrated in Fig. 3.3. The details of the numerical methods used will be discussed in the following sections.

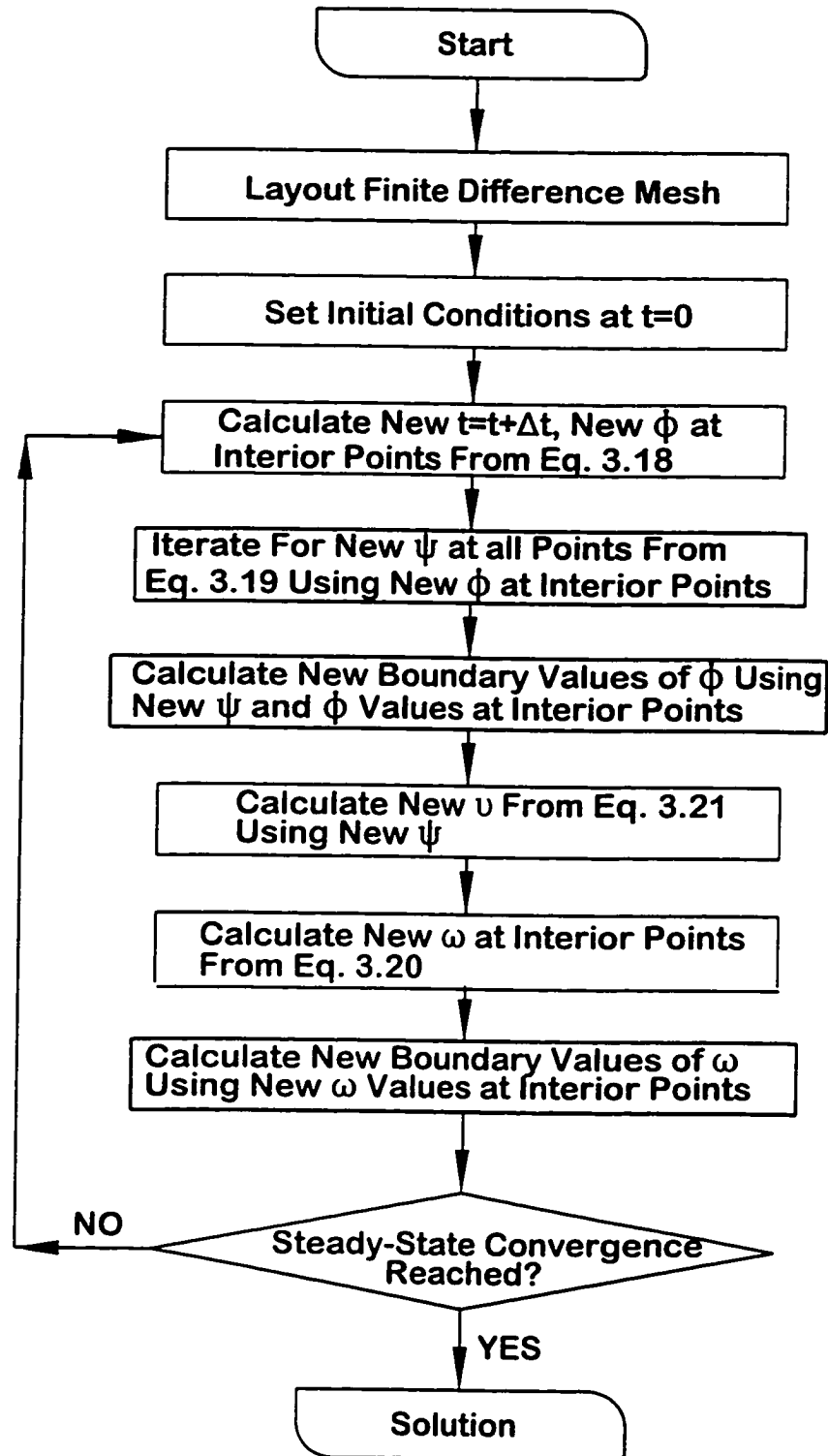


Fig.3.3: A Flowchart For Computation

### 3.2.1 Finite-Difference Formulation

By employing the Taylor-series expansions, the finite-difference forms for partial derivatives can be derived. When forward difference in time and central difference in space (FTCS) are used, one obtains second-order accuracy in space, and only first-order in time.<sup>88</sup> For a rectangular mesh system as shown in Fig. 3.4, let  $f$  represent  $\phi$ ,  $\psi$ ,  $\omega$ ,  $u_x$  or  $u_z$ ; then the various derivatives appearing in Eqs. 3.18 - 3.21 can be expressed as:

$$\left. \frac{\partial f}{\partial t} \right|_{i,j}^n = \frac{f_{i,j}^{n+1} - f_{i,j}^n}{\Delta t} \quad (3.27)$$

$$\left. \frac{\partial f}{\partial r} \right|_{i,j}^n = \frac{f_{i,j+1}^n - f_{i,j-1}^n}{2\Delta r} \quad (3.28)$$

$$\left. \frac{\partial f}{\partial z} \right|_{i,j}^n = \frac{f_{i-1,j}^n - f_{i+1,j}^n}{2\Delta z} \quad (3.29)$$

$$\left. \frac{\partial^2 f}{\partial r^2} \right|_{i,j}^n = \frac{f_{i,j-1}^n - 2f_{i,j}^n + f_{i,j+1}^n}{\Delta r^2} \quad (3.30)$$

$$\left. \frac{\partial^2 f}{\partial z^2} \right|_{i,j}^n = \frac{f_{i-1,j}^n - 2f_{i,j}^n + f_{i+1,j}^n}{\Delta z^2} \quad (3.31)$$

For the “donor cell” method, which is used for the advection terms, an average interface velocity on each side of the mesh point is first defined; the sign of these velocities, determined by upwind differencing, tells which cell values of  $f$  to use. For example,

$$\frac{\partial u f}{\partial r} = \frac{u_F f_F - u_B f_B}{\Delta r} \quad (3.32)$$

where

$$u_F = \frac{u_{i,j+1} + u_{i,j}}{2} \quad (3.33)$$

$$u_B = \frac{u_{i,j} + u_{i,j-1}}{2} \quad (3.34)$$

and

$$\begin{aligned} f_F &= f_{ij} && \text{for } [u_F, 0] \\ f_F &= f_{ij-1} && \text{for } u_F < 0 \\ f_B &= f_{ij-1} && \text{for } [u_B, 0] \\ f_B &= f_{ij} && \text{for } u_B < 0 \end{aligned} \quad (3.35)$$

It is easy to verify that the “donor cell” method is both conservative and transportive from the control-volume point of view, since interface velocities are determined by the flow direction. Compared with the upwind-differencing method, this one involves additional computations for velocities: an additional numerical differentiation of  $\psi$  to obtain  $v_r$  and additional averaging calculation of  $u_F$  and  $u_B$ . However, it is more accurate than the upwind-differencing, since it maintains something of the second-order accuracy of  $\partial v_r / \partial r$  possessed by central-difference schemes.

### 3.2.2 Solution Grid Selection

As the numerical solution of Eqs. 3.13 - 3.16 involves the approximation of the derivatives using finite-difference formula, the solution domain must be defined. A rectangular mesh system was therefore adopted here to provide a network of points. At each point the numerical values of  $\phi$ ,  $\psi$ ,  $\omega$ ,  $v_r$ , or  $v_z$  were sought to satisfy these equations. The directional indices of the solution grid are defined as shown in Fig. 3.4.

The grid size in the radial direction is determined, chiefly, by the radial dimensions of the hydrocyclone being modelled. A constant but small,  $\Delta r$ , would be favoured due to the high velocity gradient in the radial direction. Small axial grid size,  $\Delta z$ , should also be used in the overflow region of the hydrocyclone to account for short-circuiting. In the conical part, however,  $\Delta z$  would be chosen in such a way that node points fall exactly on the conical wall, and this  $\Delta z$  is generally larger than the one used in the overflow region.



Consequently, some variable width mesh system has to be designed in cylindrical section below the overflow to smooth out the change in  $\Delta z$ . As far as stability is concerned, the change in mesh spacing in this region must be gradual so as not to deteriorate the formal order of truncation error.

It is worthy of mention that the selection of grid size is a compromise between good resolution and computational time. The study extended the calculation domain into the overflow and spigot by at least five additional mesh cells. This was intended to conserve the angular momentum of the flow.

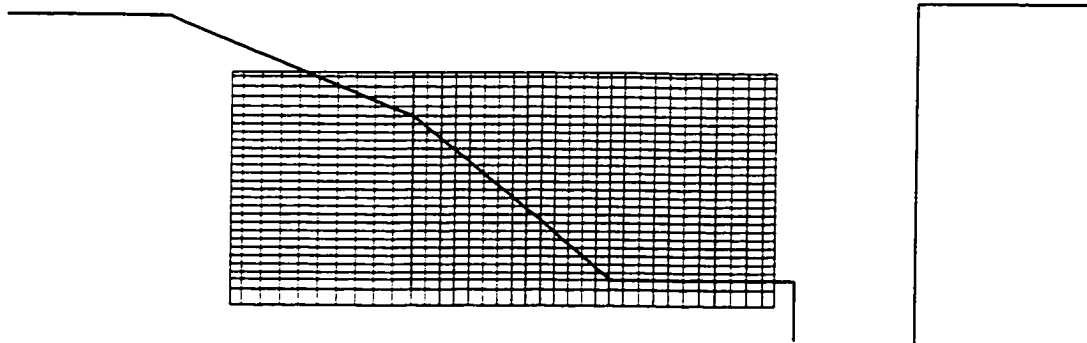
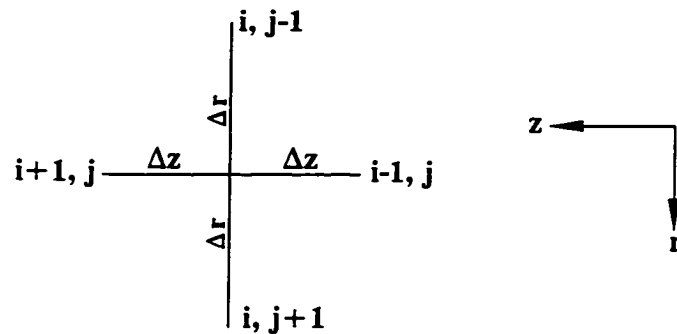


Fig. 3.4: Three-Phase Hydrocyclone Spidering.

### 3.2.3 Hopscotch Method

Roache discusses the use of the Hopscotch method for the iterative solution of the Poisson equation and its stability for quite general equations in multiple dimensions. The name 'Hopscotch' comes about from the pattern of the sweeps, shown in Fig. 3.5. At each time step,  $\phi$  is calculated in two sweeps of the mesh. In the first and substance odd-numbered time step  $\phi$ , the nodes marked with the symbol "■" in Fig. 3.5, defined by  $(i+j)$  odd, are calculated based on the current values of neighbouring points.

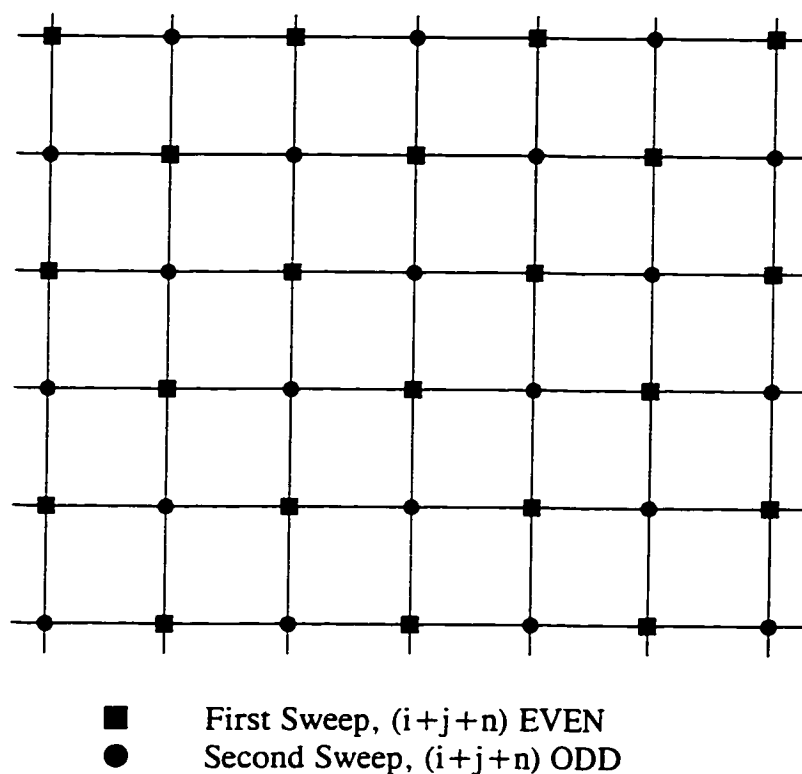


Fig. 3.5: Hopscotch Method.

For Eq. (3.18), it gives:

For  $(i+j)=\text{odd}$

$$\begin{aligned} \phi_{i,j}^{n+1} = \phi_{i,j}^n + \Delta t \left\{ \frac{1}{r_j^3} \left( \frac{\omega_{i+1,j}^{n^2} - \omega_{i-1,j}^{n^2}}{2\Delta z} \right) - \left( \frac{v_r \phi_F^n - v_r \phi_B^n}{\Delta r} \right) - \left( \frac{v_z \phi_F^n - v_z \phi_B^n}{\Delta z} \right) \right\} + \\ \frac{\Delta t}{Re} \left\{ \frac{\phi_{i,j-1}^n - 2\phi_{i,j}^n + \phi_{i,j+1}^n}{\Delta r^2} + \frac{1}{r_j} \left( \frac{\phi_{i,j-1}^n - \phi_{i,j+1}^n}{2\Delta r} \right) - \frac{\phi_{i,j}^n}{r_j^2} + \frac{\phi_{i-1,j}^n - 2\phi_{i,j}^n + \phi_{i+1,j}^n}{\Delta z^2} \right\} \end{aligned} \quad (3.36)$$

For the second sweep at the same time level, the same computation is used at nodes marked with the symbol “•” defined by  $(i+j)$  even, but now using the recently computed values at neighbouring points calculated in the first sweep:

For  $(i+j) = \text{even}$

$$\begin{aligned} \phi_{i,j}^{n+1} = \phi_{i,j}^n + \Delta t \left\{ \frac{1}{r_j^3} \left( \frac{\omega_{i+1,j}^{n^2} - \omega_{i-1,j}^{n^2}}{2\Delta z} \right) - \left( \frac{v_r \phi_F^{n+1} - v_r \phi_B^{n+1}}{\Delta r} \right) - \left( \frac{v_z \phi_F^{n+1} - v_z \phi_B^{n+1}}{\Delta z} \right) \right\} + \\ \frac{\Delta t}{Re} \left\{ \frac{\phi_{i,j-1}^{n+1} - 2\phi_{i,j}^{n+1} + \phi_{i,j+1}^{n+1}}{\Delta r^2} + \frac{1}{r_j} \left( \frac{\phi_{i,j-1}^{n+1} - \phi_{i,j+1}^{n+1}}{2\Delta r} \right) - \frac{\phi_{i,j}^{n+1}}{r_j^2} + \frac{\phi_{i-1,j}^{n+1} - 2\phi_{i,j}^{n+1} + \phi_{i+1,j}^{n+1}}{\Delta z^2} \right\} \end{aligned} \quad (3.37)$$

This second sweep is fully implicit in the sense that  $(n+1)$  values are required at  $(i,j)$ ,  $(i \pm 1, j)$ , and  $(i, j \pm 1)$  but this “implicitness” does not involve simultaneous algebraic solution, since the values at neighbouring points are already known from the first sweep.

In the second and subsequent even-numbered time steps, the role of points marked with the symbols of “■” and “●” are interchanged. This is succinctly expressed by noting that Eq. 3.36 is applied if  $(i+j+n)$  is even, and Eq. 3.37 if  $(i+j+n)$  is odd, where  $i$  and  $j$  are node subscripts and  $n$  is a time index.

The Hopscotch method is also applicable to Eq. 3.20, the angular momentum equation. In which case, the first sweep gives:

For  $(i+j+n) = \text{even}$

$$\omega_{i,j}^{n+1} = \omega_{i,j}^n + \Delta t \left\{ - \left( \frac{v_r \omega_F^n - v_r \omega_B^n}{\Delta r} \right) - \left( \frac{v_r \omega_{i,j}^n}{r_j} \right) - \left( \frac{v_z \omega_F^n - v_z \omega_B^n}{\Delta z} \right) \right\} + \frac{\Delta t}{Re} \left\{ \frac{\omega_{i,j+1}^n - 2\omega_{i,j}^n + \omega_{i,j-1}^n}{\Delta r^2} - \frac{1}{r_j} \left( \frac{\omega_{i,j-1}^n - \omega_{i,j+1}^n}{2\Delta r} \right) + \frac{\omega_{i-1,j}^n - 2\omega_{i,j}^n + \omega_{i+1,j}^n}{\Delta z^2} \right\} \quad (3.38)$$

and the second sweep gives

For  $(i+j+n) = \text{odd}$

$$\omega_{i,j}^{n+1} = \omega_{i,j}^n + \Delta t \left\{ - \left( \frac{v_r \omega_F^{n+1} - v_r \omega_B^{n+1}}{\Delta r} \right) - \left( \frac{v_r \omega_{i,j}^{n+1}}{r_j} \right) - \left( \frac{v_z \omega_F^{n+1} - v_z \omega_B^{n+1}}{\Delta z} \right) \right\} + \frac{\Delta t}{Re} \left\{ \frac{\omega_{i,j+1}^{n+1} - 2\omega_{i,j}^{n+1} + \omega_{i,j-1}^{n+1}}{\Delta r^2} - \frac{1}{r_j} \left( \frac{\omega_{i,j-1}^{n+1} - \omega_{i,j+1}^{n+1}}{2\Delta r} \right) + \frac{\omega_{i-1,j}^{n+1} - 2\omega_{i,j}^{n+1} + \omega_{i+1,j}^{n+1}}{\Delta z^2} \right\} \quad (3.39)$$

Compared to the popular Alternating Direction Implicit (ADI) method, the Hopscotch method takes less time per computational step to solve the parabolic differential equations, due to the absence of tridiagonal inversions. It is also considerably easier to program than ADI method, especially for complex geometries. However, for calculations of the vorticity transport equation, it shares with ADI method the difficulty of implicit boundary values.

### 3.2.4 Successive Over-Relaxation (SOR) Method

Comprehensive analysis by Roache<sup>88</sup> shows that the solution of (steady) elliptic equations by iteration is analogous to solving for the asymptotic steady-state value of time dependent problem. Consider a time-dependent diffusion equation for  $\psi$  with a source term,  $-r\phi$ , and with a diffusion coefficient of unity:

$$\frac{\partial \psi}{\partial t} = \nabla^2 \psi + r\phi \quad (3.40)$$

The physical significance of the transient solution is not important, but as steady state is approached, the solution approaches the desired solution for the Poisson equation, Eq. 3.19.

Applying FTCS differencing to Eq. 3.40, one obtains

$$\psi_{i,j}^{n+1} = \psi_{i,j}^n + \Delta t \left\{ \frac{\psi_{i,j+1}^n - 2\psi_{i,j}^n + \psi_{i,j-1}^n}{\Delta r^2} - \frac{1}{r_j} \left( \frac{\psi_{i,j+1}^n - \psi_{i,j-1}^n}{2\Delta r} \right) + \frac{\psi_{i+1,j}^n - 2\psi_{i,j}^n + \psi_{i-1,j}^n}{\Delta z^2} + r_j \phi_{i,j}^{n+1} \right\} \quad (3.41)$$

Defining  $\lambda = \Delta r/\Delta z$ , taking the largest possible  $\Delta t = \Delta r^2/2(1 + \lambda^2)$ , and rearranging, Eq. 3.41 gives

$$\psi_{i,j}^{n+1} = \frac{1}{2(1+\lambda^2)} \left\{ \psi_{i,j+1}^n + \psi_{i,j-1}^n + \lambda^2(\psi_{i-1,j}^n + \psi_{i+1,j}^n) - \frac{\Delta r}{2r_j}(\psi_{i,j+1}^n - \psi_{i,j-1}^n) + \Delta r^2 r_j \phi_{i,j}^{n+1} \right\} \quad (3.42)$$

This is Richardson's method which is also known as the Jacobi method as discussed by Roache.<sup>88</sup> Eq. 3.42 is a two-level equation, requiring storage of  $\psi_{i,j}^{n+1}$  and  $\psi_{i,j}^n$ . If one sweeps in the direction of increasing  $i$  and  $j$  and uses new values wherever available in Eq. 3.42, one obtains

$$\psi_{i,j}^{n+1} = \frac{\left\{ \psi_{i,j+1}^n + \psi_{i,j-1}^{n+1} + \lambda^2(\psi_{i-1,j}^n + \psi_{i+1,j}^{n+1}) - \frac{\Delta r}{2r_j}(\psi_{i,j+1}^n - \psi_{i,j-1}^{n+1}) + \Delta r^2 r_j \phi_{i,j}^{n+1} \right\}}{2(1+\lambda^2)} \quad (3.43)$$

Which is the Gauss-Seidel, a method covered by Roache.<sup>88</sup>

Roache discussed the method of applying over-relaxation to the Gauss-Seidel method in a methodical manner suitable for computer programming and called it the, "Successive over-relaxation" method. Adding and subtracting  $\psi_{i,j}^n$  to the right-hand side

of Eq. 3.43 and regrouping terms gives:

$$\psi_{i,j}^{n+1} = \psi_{i,j}^n + \frac{\left\{ \psi_{i,j-1}^n + \psi_{i,j-1}^{n+1} + \lambda^2(\psi_{i-1,j}^n + \psi_{i-1,j}^{n+1}) - \frac{\Delta r}{2r_j}(\psi_{i,j-1}^n - \psi_{i,j-1}^{n+1}) + \Delta r^2 r_j \phi_{i,j}^{n+1} - 2(1+\lambda^2)\psi_{i,j}^n \right\}}{2(1+\lambda^2)} \quad (3.44)$$

In the SOR method, the bracketed term in Equation (3.44) is multiplied by a relaxation factor  $\mathfrak{D}$ , where  $\mathfrak{D} \neq 1$ ; thus one obtains

$$\psi_{i,j}^{n+1} = \psi_{i,j}^n + \frac{\mathfrak{D} \left\{ \psi_{i,j-1}^n + \psi_{i,j-1}^{n+1} + \lambda^2(\psi_{i-1,j}^n + \psi_{i-1,j}^{n+1}) - \frac{\Delta r}{2r_j}(\psi_{i,j-1}^n - \psi_{i,j-1}^{n+1}) + \Delta r^2 r_j \phi_{i,j}^{n+1} - 2(1+\lambda^2)\psi_{i,j}^n \right\}}{2(1+\lambda^2)} \quad (3.45)$$

For convergence, it is required that  $1 < \mathfrak{D} < 2$ . Frankel and Young both determined an "optimum" value  $\mathfrak{D}_o$ , basing their optimality criterion on the asymptotic reduction of the most resistant error. The optimum value  $\mathfrak{D}_o$  depends upon the mesh, the shape of the domain, and the type of boundary conditions. For a Dirichlet problem in a rectangular domain of size  $(I-1)\Delta z$  by  $(j-1)\Delta r$  with constant  $\Delta z$  and  $\Delta r$ , it may be shown that

$$\mathfrak{D}_o = 2 \left( \frac{1 - \sqrt{1 - \xi}}{\xi} \right) \quad (3.46)$$

Where

$$\xi = \left\{ \frac{\lambda^2 \cos\left(\frac{\pi}{I-1}\right) + \cos\left(\frac{\pi}{J-1}\right)}{1 + \lambda^2} \right\}^2 \quad (3.47)$$

### 3.3 Boundary Conditions

It is easy to conjure up some kind of plausible boundary conditions for  $\eta$ ,  $\psi$ ,  $\omega$ ,  $u_r$ ,  $u_z$ , but attempts to determine realistic and accurate conditions that result in stable solution can be extremely difficult. For instance, a partial differential equation such as Eq. 3.19 really contains very little information on  $\psi$ . All the fantastic flow patterns of common

gases and liquids are solutions of the same PDE. The flows are distinguished only by boundary and initial conditions and by the flow parameters such as the Reynolds number. It is therefore not surprising that the specification of computational boundary conditions, besides affecting numerical stability greatly affects the accuracy of the finite-difference equation solution. Nevertheless, boundary conditions must be specified at all points on the boundaries enclosing the field of the flow in order to obtain numerical solution of Eqs. 3.18 - 3.21.

It may be noted that a theoretical prediction of the flow field obtained independently of all empiricism cannot yet be achieved. Clearly, for the analytical predictions to accurately resemble the measured flow field. The boundary conditions must reflect experimental condition as close as possible. The boundaries, where steady-state conditions should be specified, are the solid walls (inner, outer and roof), the inlets and outlets (overflow, transflow and spigot) and the lighter-liquid interface. The boundary conditions adopted at these locations are now examined in detail.

### 3.3.1 Solid Walls

The conditions of no-slip and impermeability are assumed at the solid walls. As a result, the axial and radial velocity components are zero at the walls. Also from Eq. 3.21, it is concluded that the stream function must be constant at the walls. The value of vorticity at the wall, however, is somewhat difficult to obtain but is extremely an important quantity. The vorticity transport equation for  $\partial\phi/\partial t$  determines how  $\phi$  is advected and diffused, but the total  $\phi$  is conserved at interior points. However, at no-slip boundaries,  $\phi$  is produced. Actually, it is the diffusion and subsequent advection of vorticity, which is produced at walls, that drives the problem.

Consider a horizontal wall as shown in Fig. 3.4. The vorticity is obtained from the no-slip conditions. If  $\psi_{i+1,j}$  expanded by a Taylor series around the wall values,  $\psi_{i,j}$ , we get,

$$\psi_{i-1,j} = \psi_{i,j} + \frac{\partial \psi}{\partial z} \Big|_{i,j} \Delta z + \frac{1}{2} \frac{\partial^2 \psi}{\partial z^2} \Big|_{i,j} \Delta z^2 + O(\Delta z^3) \quad (3.48)$$

At no-slip condition:

$$\frac{\partial \psi}{\partial z} \Big|_{i,j} = 0, \quad -\frac{1}{r_j} \frac{\partial \psi}{\partial z} \Big|_{i,j} = v_r \Big|_{i,j} = 0 \quad (3.49)$$

and

$$-\frac{1}{r_j} \frac{\partial^2 \psi}{\partial z^2} \Big|_{i,j} = \frac{\partial v_r}{\partial z} \Big|_{i,j} \quad (3.50)$$

Along the wall,  $\partial v_z / \partial r = 0$ ,  $\therefore v_z = 0$ . And because

$$\phi = \frac{\partial v_r}{\partial z} - \frac{\partial v_z}{\partial r} \quad (3.51)$$

Thus

$$\phi_{i,j} = \frac{\partial v_r}{\partial z} \Big|_{i,j} = -\frac{1}{r_j} \frac{\partial^2 \psi}{\partial z^2} \Big|_{i,j} \quad (3.52)$$

Substituting Eq. 3.52 into Eq. 3.48 and solving for  $\phi_{i,j}$  gives:

$$r_j \phi_{i,j}^n = \frac{-2(\psi_{i+1,j} - \psi_{i,j})}{\Delta z^2} + O(\Delta z) \quad (3.53)$$

Likewise for a vertical wall shown in Fig. 3.4, the same Taylor-series expansion gives



$$\psi_{i,j-1} = \psi_{i,j} + \frac{\partial \psi}{\partial r} \Big|_{i,j} \Delta r + \frac{1}{2} \frac{\partial^2 \psi}{\partial r^2} \Big|_{i,j} \Delta r^2 + O(\Delta r^3) \quad (3.54)$$

At no-slip condition:

$$\frac{\partial \psi}{\partial r} \Big|_{i,j} = 0, \quad \frac{1}{r_j} \frac{\partial \psi}{\partial r} \Big|_{i,j} = v_z \Big|_{i,j} = 0 \quad (3.55)$$

and

$$\frac{\partial v_z}{\partial r} \Big|_{i,j} = \frac{1}{r_j} \frac{\partial^2 \psi}{\partial r^2} \Big|_{i,j} - \frac{1}{r_j^2} \frac{\partial \psi}{\partial r} \Big|_{i,j} = \frac{1}{r_j} \frac{\partial^2 \psi}{\partial r^2} \Big|_{i,j} \quad (3.56)$$

Along the wall,  $\partial v_r / \partial z = 0$ ,  $\therefore v_r = 0$ . And because

$$\phi_{i,j} = \frac{\partial v_r}{\partial z} \Big|_{i,j} - \frac{\partial v_z}{\partial r} \Big|_{i,j} \quad (3.57)$$

Thus

$$\phi_{i,j} = -\frac{\partial v_z}{\partial r} \Big|_{i,j} = -\frac{1}{r_j} \frac{\partial^2 \psi}{\partial r^2} \Big|_{i,j} \quad (3.58)$$

Substituting Eq. 3.58 into Eq. 3.54 and solving for  $\phi$  gives

$$r_j \phi_{i,j}^n = \frac{-2(\psi_{i,j-1} - \psi_{i,j})}{\Delta r^2} + O(\Delta r) \quad (3.59)$$

so, regardless of the wall orientation or boundary value of  $\psi$ , the following holds:

$$r \phi_w = \frac{-2(\psi_{w+1} - \psi_w)}{\Delta n^2} + O(\Delta n) \quad (3.60)$$

Where  $\Delta n$  is the distance, from  $(w+1)$  to  $(w)$ , normal to the wall.

The boundary values of angular-spin velocity at the walls are approximately by the universal velocity-distribution law<sup>88</sup> for smooth pipe. For a very large Reynolds number, the universal velocity-distribution law has the form

$$\frac{v}{v_w} = 2.5 \ln \left( \frac{d_w v_w \rho}{\mu} \right) + 5.5 \quad (3.61)$$

Where  $v_w$  = friction velocity and  $d_w$  = distance from the wall.

Being for turbulent flow, Eq. 3.61 is valid only in region where the laminar shearing stress can be neglected in comparison with the turbulent stress. In the immediate neighbourhood of the wall, where the turbulent shearing stress decreases to zero and laminar stresses predominate, deviations from this law must be expected. Hsieh<sup>17</sup> noted that experimental measurements of tangential velocity by LDV play an important role in fine-tuning the approximation of boundary values of the angular-spin velocity.

### 3.3.2 Feed Flow

Given that the feed tube is perpendicular to the axis of symmetry of the hydrocyclone, there is no axial component at the inlet. As a result, given the inlet pipe diameter and mass flow rate, the velocity vector can be resolved in the tangential and radial directions. In the current work, because of the assumption of axisymmetry, the radial component is responsible for convecting mass into the hydrocyclone. As has been pointed out previously, the feed enters the calculation domain through an inlet ring; this component is averaged along the periphery of the hydrocyclone while the tangential component remains the same.

There are two ways to specify the discretized inflow radial velocity. The discrete values of  $\psi$  may be matched to the input continuum solution. However, when one now numerically differentiates  $\psi_{i,j}$  to get  $v_{r,i,j}$  the discretized  $v_{r,i,j}$  are not the input continuum solution of  $v_r$ . The alternative method is to discretize the radial velocities at the inlet and then evaluate  $\psi_{i,j}$  in manner compatible with the velocity differencing as in:

$$v_{r,i,j}^n = \frac{-(\psi_{i-1,j} - \psi_{i,j})}{2r_j \Delta z} \quad (3.62)$$

This method would give

$$\psi_{1,j} = 0 \quad (3.63)$$

$$\psi_{2,j} = -r_j \Delta z v_{r,2,j} \quad (3.64)$$

The second method gives the correct radial velocity but results in a discretization error for

$$\psi_{i,j} = -2r_j \Delta z v_{r,i-2,j} + \psi_{i-2,j} \quad (3.65)$$

$\psi_{i,j}$ . Of course, both methods converge for  $\Delta z \rightarrow 0$ . Since the dynamics are affected by  $v_r$  rather than  $\psi$ , the second method of matching the desired  $v_r$  is preferred. Also it has been pointed out that close agreement between numerical and experimental inflow boundary conditions is often necessary for overall solution agreement<sup>88</sup> so the tangential- and radial-velocity components of the inlet ring are thus calculated from the experimentally measured velocity profile of the inlet pipe. Incidentally, these inflow boundary values can be closely approximated by one-seventh-power velocity-distribution law for turbulent flow in pipes at Reynolds number around  $10^5$ .

Having fixed the flow boundary values of  $v_{r,i,j}$ , and  $\psi$ , the following is automatically fixed:

$$\left. \frac{\partial v_r}{\partial z} \right|_{i,j} = -\frac{1}{r_j} \left. \frac{\partial^2 \psi}{\partial z^2} \right|_{i,j} \quad (3.66)$$

This is the first of the two terms in Eq. 3.57. The second term could also have been fixed from the boundary layer solution, but instead, less restrictive evaluations were attempted.

The most successful method found was to approximate

$$\left. \frac{\partial}{\partial r} \left( \frac{\partial v_z}{\partial r} \right) \right|_{i,j} = 0 \quad (3.67)$$

$$\begin{aligned}
\left. \frac{\partial v_z}{\partial r} \right|_{i,j} &= \left. \frac{\partial v_z}{\partial r} \right|_{i,j-1} = \left. \frac{\partial}{\partial r} \left( \frac{1}{r} \frac{\partial \psi}{\partial r} \right) \right|_{i,j-1} \\
&= -\frac{1}{r^2} \left. \frac{\partial \psi}{\partial r} \right|_{i,j-1} + \frac{1}{r} \left. \frac{\partial^2 \psi}{\partial z^2} \right|_{i,j-1}
\end{aligned} \tag{3.68}$$

The following equation is finally obtained,

$$\left. \frac{\partial v_z}{\partial r} \right|_{i,j} = \frac{(\Delta r - 2r_{j-1})\psi_{i,j} + 4r_{j-1}\psi_{i,j-1} - (\Delta r + 2r_{j-1})\psi_{i,j-2}}{2r_{j-1}^2 \Delta r^2} \tag{3.69}$$

### 3.3.3 Outflow

The evaluation of  $\phi$ ,  $\psi$ , and  $\omega$  at the outflow boundary is one of the most interesting computational boundary problems. Somehow the details of the farther downstream flow must be neglected and an attempt made to obtain realistic answers upstream. Numerical experience has shown that catastrophic instabilities may be propagated upstream from the outflow boundary and can destroy the solution. Therefore the objective of the calculation is to allow the most free-flow adjustment at outflow boundaries, which still gives a solution.

An outflow boundary condition which approximates  $\partial v_r / \partial z = 0$  for  $\psi$  is adopted; Since

$$v_r = -\frac{1}{r} \frac{\partial \psi}{\partial z} \Rightarrow \frac{\partial^2 \psi}{\partial z^2} = 0 \tag{3.70}$$

which can be approximated by linear extrapolation out to  $i=I$ . For constant  $\Delta z$ , this gives

$$\psi_{I,j} = 2\psi_{I-1,j} - \psi_{I-2,j} \tag{3.71}$$

The extrapolation of  $\psi_{I,j}$  should be performed after each SOR iteration for the Poisson equation.

Linear extrapolation is also applicable to variables  $\phi$  and  $\omega$  on the outflow boundaries to achieve stability, if the implicit Hopscotch method is used to solve the velocity transport and angular momentum equations. In this case, when one approximates  $\phi$  and  $\omega$  out to  $i = I$ , one obtains

$$\phi_{I,j} = 2\phi_{I-1,j} - \phi_{I-2,j} \quad (3.72)$$

$$\omega_{I,j} = 2\omega_{I-1,j} - \omega_{I-2,j} \quad (3.73)$$

However, it should be noted the applicability of linear extrapolation depends very much upon numerical method used.

### 3.3.4 Lighter-Liquid Interface - Absent-Air-Core

The water/oil interface, which divides the body of fluid within the hydrocyclone and the column of oil forming the oil core itself, is impervious to water and may hence be represented by stream surface. Since the no-slip boundary condition is also applicable to this stream surface, it behaves like a solid wall in some aspect. Consequently, Eqs. 3.60 and 3.61 can be used to compute boundary values of  $\phi$  and  $\omega$  at the water/oil interface. On the other hand, although this stream surface is still a streamline with constant  $\psi$ , the value of that  $\psi$  is not specified but is free to develop.

Prior to computing the boundary values of  $\psi$  at the water/oil interface, the radius of the oil core must be determined. Convincing formulation for oil core radii of different hydrocyclones classifying under a wide range of operating conditions are virtually non-existent in the literature. Nevertheless, Tarjan<sup>88</sup> cited research where the air-core radius,  $R_a$ , varied from 0.06-0.33 $R_c$  depending on hydrocyclone design and operating conditions. Lilge<sup>85</sup> claimed that  $R_a = 0.083 R_c$ , but did not give experimental data to back up the claim. From Kelsall<sup>11</sup> it would certainly seem that  $R_a$  cannot be a function of  $R_c$  alone.

In the current study of a 80-mm hydrocyclone under various operating conditions, the oil-core radius seems to be not only a function of  $R_c$  but also a function of viscosity and volumetric flow rate. In addition, the oil-core shape was found to be wider in the overflow region than in the spigot region. However, mathematical formulation for oil-core radius will not be proposed here due inefficient data available. Instead, the experimental measured oil-core radius in the spigot region was used, and the oil-core was assumed to be constant throughout the hydrocyclone. It should be noted that both the radius and the shape of oil-core can be determined by iteration, at the expense of much longer computational time.

Since the radial grid size is relatively small compared to the oil-core radius in this modelling work, one can safely assume liquid/air interface coincides with an axial grid line at  $j = j_a$ . With an additional "fictitious" node point at  $j = j_a - 1$  in the spigot region,  $\psi_{j_a - 1}$  is set equal to  $\psi_{j_a + 1}$  for each computation of the Poisson equation. The later equation is solved for all points up to  $j = j_a = 1$ . This implies nothing but  $v_z = 0$  at  $j = j_a$ . Then  $\psi_{j_a}$  is computed with the same Poisson equation, and average value of  $\psi_{j_a}$  determined in the spigot region is assigned to all the node points at the liquid/air interface.

### 3.3.5 Sharp Corners

Here no problem is posed for the boundary conditions at the sharp corner on the intersection of the overflow and the roof. Simply in this region  $\phi = 0$ ,  $\psi = 0$  and  $\omega = \omega_{in}$ , because  $\phi$ ,  $\psi$ , and  $\omega$  defined at these points do not even enter into the calculation when the equations are used at interior points. However, the computational condition at the sharp convex corner, on the overflow tip, require special considerations regarding boundary values and numerical accuracy.

The stream function at the sharp convex corner, like the rest of the solid wall, equal zero. However, there are several alternatives for the evaluation of  $\phi$  since the no-slip wall condition for  $\phi$  at the sharp convex corner can be applied in a number of ways. In this modelling work, this continues values of  $\phi$  are used, as shown in Fig. 3.4, each one

evaluated with Eq. 3.60. Such discontinuous treatment of boundary conditions was discussed by Roache<sup>88</sup>. Discontinuous formulation is also used for  $\omega$ , in which case Eq. 3.61 is applied to compute each of the boundary values.

## Chapter 4

### 4.0 EXPERIMENTAL WORK

Experiments were carried out to determine the performance of the three-phase hydrocyclone as discussed in Chapter 1. The scope of the experimental program included determination of oil and solids efficiencies at low and high feed concentrations, the influence of feed concentrations on performance parameters, reverse vortex stability, droplet/particle size distributions and influence of Reynolds, flow and split ratio numbers on vortex stability.

#### 4.1 Experimental Set-up

A schematic of the flow loop used in the current study is shown in Fig. 4.1. The major parts of the loop are: 1) a three-phase hydrocyclone unit and piping, 2) storage tank, 3) oil tank, 4) water pump, 5) oil pump, 6) iso-kinetic sampler unit, 7) oily-water system, 8) optical system. The overflow, underflow and transflow streams from the hydrocyclone discharge freely into a 600-litre PVC cylindrical tank. This was used for temporary storage of the mixture prior to pumping. Attached to the tank was an ac-motor driven impeller for mixing of the mixture. It was maintained at 20-23°C. Two 5-litre plastic containers were used for the storage of oil.

The hydrocyclone unit was built from the designed acrylic parts, flanges and connectors to its full length incorporating the solids outlet. A centrifugal pump capable of handling up to 200 l/min of oil-solid-water mixtures was used. The pump was supplied from a 600-litre tank. In addition to the feed supply valve, a bypass was included in the line to assist in the control of pressure and volumetric flow rate of the inlet line. The inlet pressure line was 15-mm ID PVC reinforced tube and the return lines were 20-mm ID, 15-mm ID and 12.5-mm ID for underflow, trans-flow and overflow respectively. Before entering the hydrocyclone, the inlet was passed through a (0.6-5.8m<sup>3</sup>/hr) flowmeter.



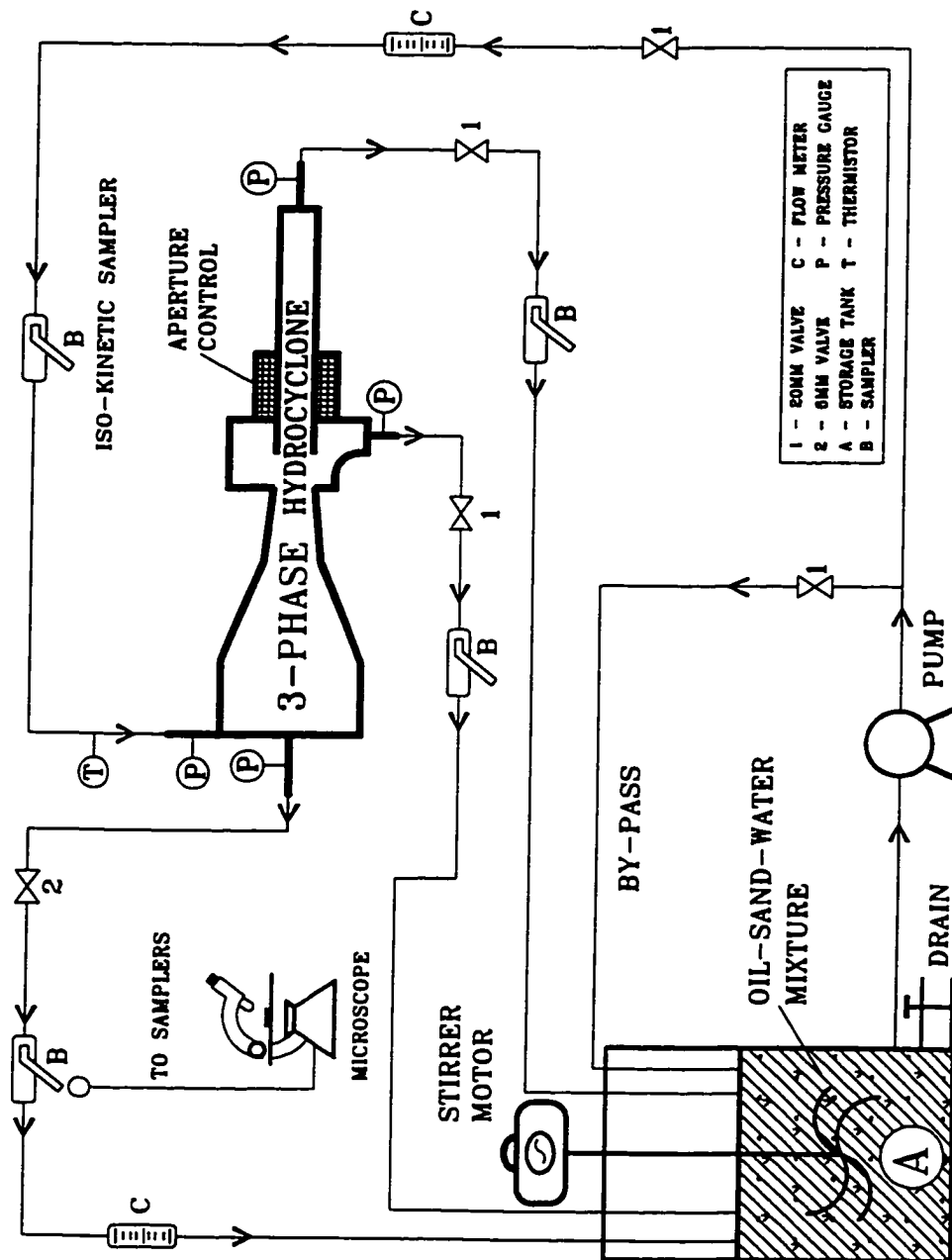


Fig. 4.1: An Experimental Set-up for Testing the Three-phase Hydrocyclone in the Current Study.

The overflow stream was passed through a 6-mm ID valve prior to returning to the feed tank. The underflow stream was routed through a 20-mm valve and, during the tests, through an iso-kinetic sampler identical to the inlet sampler. Before returning to the feed tank, the underflow stream was passed through a second flowmeter. Pressure differentials between the inlet and the three outlet ports were measured by a pressure gauge (0-160psi) stationed in each stream.

All flow rates were measured by turbine flowmeters. Five turbine flowmeters were used in the flow circuit since measurement of flowrates was conducted at five points - oil injection flow into the main stream, flowrate of inlet, oil overflow, flowrate of solids trans-flow and water at the underflow. Water temperature upstream was measured by a thermistor probe. In order to analyze oil and solids droplet/particle size distributions and concentrations in the outlet streams - the feed, trans-flow and underflow streams samples were scooped during testing without flow disturbance. Because large volumetric flow rates of the feed and underflow streams about 100 litre/min hampered the total diversion of each stream for sampling, some technique was necessary to take representative samples from these streams. This was accomplished by using an iso-kinetic sampler stationed in each stream. The iso-kinetic sampler unit consists of one 5-mm ID probe tapped to one manometer (see Appendix F).

The oily-water system consisted of dispersions of Forties crude oil and quartz sand in water. Various mixtures of oil/sand/water were prepared for testing. One of the problems in working with oil-solids suspensions is in maintaining a homogeneously mixed suspension in the test circuit. In this study an ac motor - 1750 RPM, 0.5 HP- rotated a two-bladed centripetal impeller to stir the suspension. To boost the stirring up, the overflow, trans-flow and underflow lines were routed to discharge, below the liquid-air interface, into the feed tank. This composite of measures was designed to give a homogeneous suspension with no air entrainment into the feed tank. Experiments were conducted on the hydrocyclone at various inlet flow conditions and oil/solid/water mixtures. The operating variables considered for control were: Influent flow rates of the

mixtures, inlet concentrations of oil and solids, inlet-outlet pressure drops and viscosity of transporting medium, i.e., water. Each experimental run proceeded as follows to:

1. Adjust the flow conditions for optimum operation; adjust inlet and the transverse aperture size;
2. Calibrate the sampling and metering devices;
3. Commence sampling and data collection;
4. Inject dye and visualize the flow inside hydrocyclone at regular intervals to study vortex stability.

For each experiment conducted, the separation efficiencies of oil and solids were computed from concentrations (in ppm) of their respective inlet and outlet flow streams. The particle size distributions for oil and sand were carried out on a Malvern Laser Droplet and Particle Sizer S2600. This consists of the droplet/particle sizer coupled to a PC and recorder. The oil and sand concentrations were determined by gravimetric method (see appendix D). Feed and outlet stream droplet/particle sizes were required in order to monitor the on-line performance of three-phase hydrocyclone. The droplets and particles were observed under an optical microscope.

#### **4.2 The Three-Phase Hydrocyclone Design**

The three-phase hydrocyclone design used in the current study was constructed from acrylic parts and connectors. It is 1.6 m long and has a diameter of 80 mm as shown in Figs. 4.2- 4.3. Its photograph is shown in Fig. 4.4. The clear acrylic construction allows for the optical visualization of the interior flow phenomena. The inlet tube consisted of a short section of acrylic protruding from the body, forming an "outer wall tangential entry" type. This type of feed inlet has an outer wall of the inlet entry tube tangential to the wall of the hydrocyclone. Two cones with angles  $20^\circ$ , and  $10^\circ$  have been architecturally structured downstream co-axial with the hydrocyclone axis.

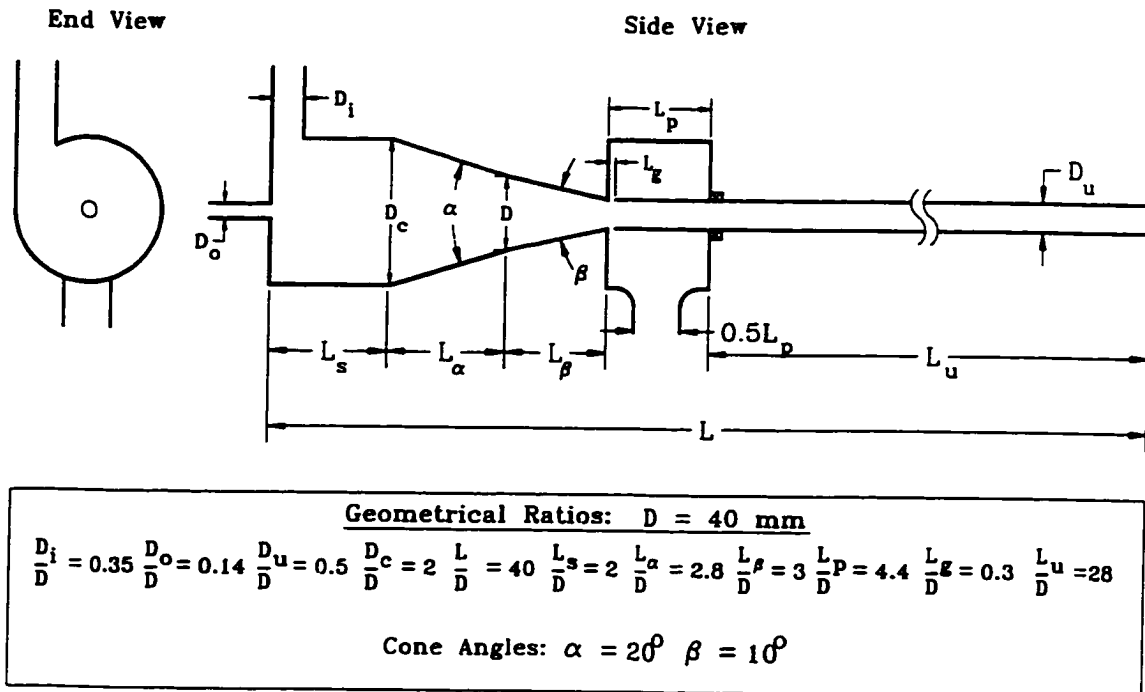


Fig. 4.2: A Three-Phase Separation Hydrocyclone Design Used in the Current Study.

At the intersection of the last cone and cylindrical section, there is a circumferential aperture which opens into an annulus formed by the outer surface of cylindrical section and the inner cylindrical chest designed to smuggle the solids. Fig. 4.2 shows a transflow aperture of 12 mm but in most of the experiments it was fixed at 6 mm as previous experiments<sup>4</sup> had found this aperture optimal. This was done by using the adjustable knob on the threaded cylindrical section and line swivel joint at the end of the cylindrical section. The swivel joint facilitated the support and angular rotation of the section without disruption of the flow field. The hydrocyclone is installed horizontally as shown in Fig. 4.1. The feed is a protrusion of the acrylic body, forming an outer wall tangential entry. The 5.6-mm overflow orifice was a central roof protrusion of the acrylic body and its other end was flushed with the interior roof of the hydrocyclone.

DESIGN - CONICAL LENGTH/DIAMETER RATIOS

$$\frac{D_o}{D} = 0.14 \quad \frac{D_c}{D} = 2 \quad \frac{D_u}{D} = 0.5 \quad \alpha = 20^\circ \quad \beta = 10^\circ$$

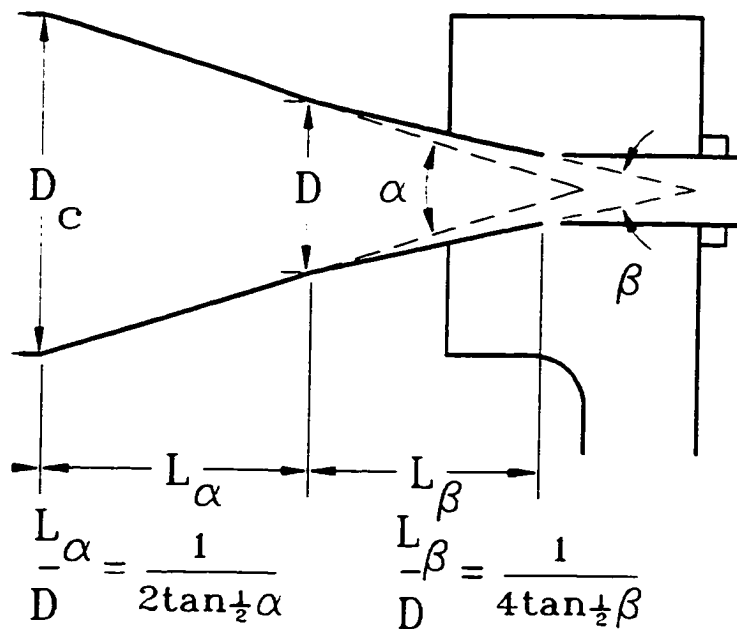


Fig. 4.3: Three-phase Hydrocyclone Conical Length/Nominal Diameter Ratios

For the purpose of design, Fig. 4.3 portrays the ratios conical lengths to the nominal diameter. The ratios are important in determining the capacity of the hydrocyclone. They are:

$$\frac{L_{\alpha}}{D} = \frac{1}{2 \tan \frac{1}{2} \alpha}$$

and the other is

$$\frac{L_{\beta}}{D} = \frac{1}{4 \tan \frac{1}{2} \beta}$$

then the ratio of the conical lengths - upstream to the downstream:

$$\frac{L_{\alpha}}{L_{\beta}} = \frac{2 \tan \frac{1}{2} \beta}{\tan \frac{1}{2} \alpha}$$

The taper section for the hydrocyclone was constructed using three main parts; the swirl chamber accommodates the feed and overflow orifices, the multiple-coned and annulus section accommodate the transverse-flow, and the threaded underflow section accommodates the knob for adjustment of the separation gap. Between the swirl chamber section was grooved for an 16-mm O-ring 75mm diameter. This was used to seal the swirl chamber and the multiple-coned section. In addition, the sections had dowelled flanges with four evenly spaced 6-mm ID holes. With the underflow knob and threaded part, and the annulus, the three-phase hydrocyclone could be transformed into a conventional hydrocyclone by closing the separation gap (setting to zero), i.e., two phase separation. All the interior surfaces were machined and polished until they were hydraulically smooth.

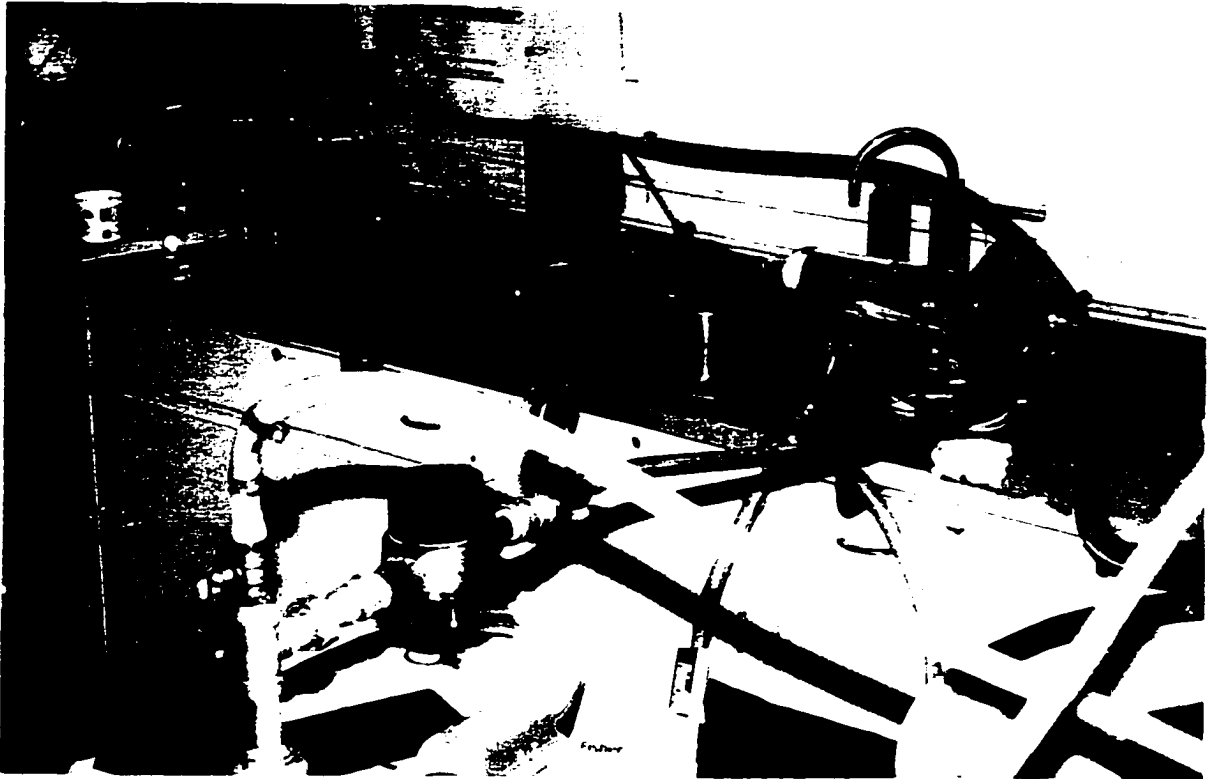


Fig. 4.4: Photograph of the Physical Three-Phase Hydrocyclone.

### 4.3 Fluid Flow Visualization

The flow patterns in the three-phase hydrocyclone were examined by dye injection (see Fig. 4.5) for various split ratios. Food colour dyes specifically blue and green were used to visualize the flow and the various observed phenomena were photographed. This part of the experiment was very important in studying the vortex structure equilibrium.

Under optimum operating conditions, the reverse vortex inside the hydrocyclone was visualized using the hypodermic dye injector - a hypodermic needle. 2 mls of green dye was injected upstream and the 2 mls of blue dye downstream and photographs were taken. The operating parameters used for fluid flow visualization are shown in Table 4.1. Instability of the vortex necessitated the measurement of its amplitude. This was accomplished by graduating the hydrocyclone axial length as shown in Fig. 4.6.

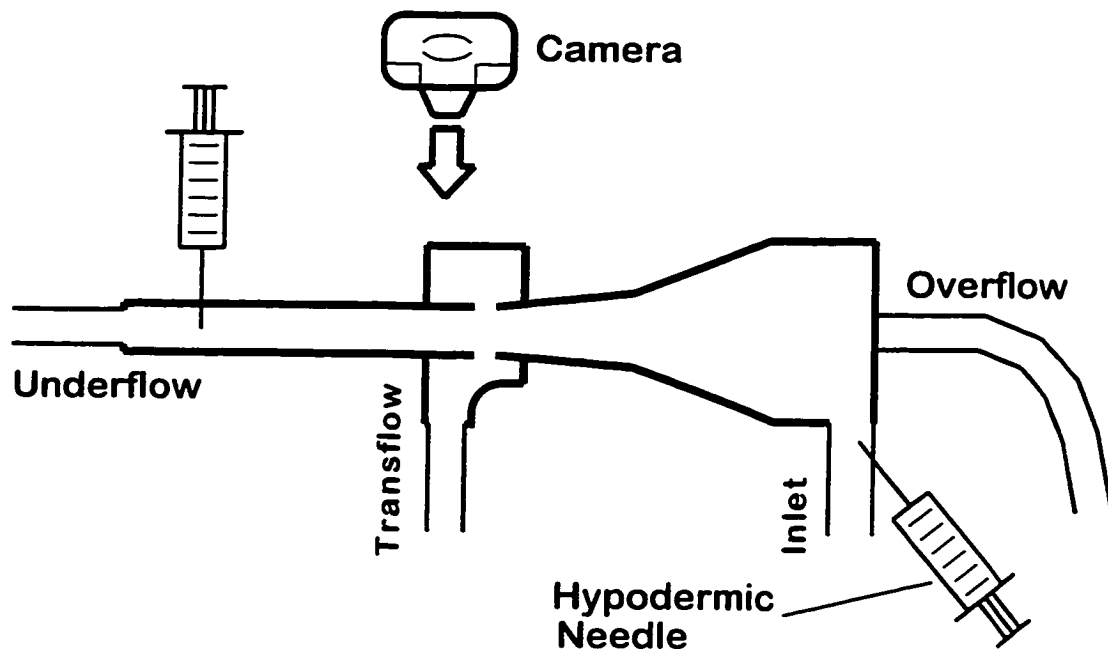


Fig. 4.5: Hypodermic Dye Injector.

Table 4.1: Flow Visualization at Feed Pressure of 5.4 psig.

$Q_o/Q_u$	$Q_o$ , cc/s	$Q_u$ , cc/s	$Q_o/Q_t$	$Q_t$ , cc/s	Re
4.0	300	75	2.5	120	68,000
2.0	150	75	2.0	75	40,905
0.25	95	380	0.5	190	60,293
$\infty$	550	0	$\infty$	0	49,866



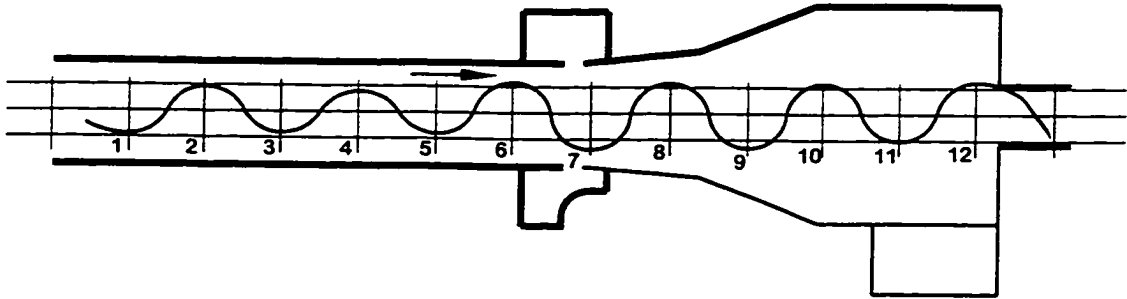


Fig. 4.6: Determination of Vortex Amplitude.

#### 4.4 Test Materials

Table 4.2: Physical Properties of Test Materials.

Material	Viscosity at 20°C poise	Specific Gravity at 20°C (S.G)	Interfacial Tension (mN/m)
Crude Oil	25	0.83	20
Quartz Sand	-	2.65	-
Water	$10^{-3}$	1	-

Table 4.3 Sieve Analysis of Quartz Sand (SG=2.65)

Size, $\mu\text{m}$	Percent
> 140	10
80 - 140	36
45 - 80	42
9 - 45	10

#### 4.5 Experimental Procedure

Inlet concentrations of each dispersion of crude oil and quartz sand were obtained by mixing 200 ml of crude oil and 160g of sand with 250 litres of tap water. Samples for the feed, trans-flow and underflow streams ranged from 500 ml at volumetric flow rates (40 litre/min) to 750 ml at volumetric flow rates (100 litre/min). These volumes represent sampling times of approximately 10 to 20 seconds. The size density distribution was assumed to be unaffected by the removal of this small samples from the mixture. Overflow samples were not collected because these contained a large amount of crude oil, which would necessitate replenishment of the dispersion. A closure of the steady state material balance was not pursued directly, but the reproducibility of the separation measurements was indicative of steady state conditions. Pressure readings and flow rates were recorded for various conditions.

The determination of the separation efficiency involved the use of the iso-kinetic sampling technique and subsequent gravimetric analysis. The mass fractions of dispersed phase in the feed, trans-flow and underflow streams were determined gravimetrically using a filtration technique. To separate the crude oil and sand from the sample fluid, Whatman #42 filters (passing 2.5  $\mu\text{m}$  particles and below) were used in a multiple funnel-aspirator arrangement as shown in Fig. 4.7. Three units of the arrangement were used, each holding 10 sub-samples for each stream. The filter papers were dried and weighed prior to filtering. After filtering, the papers, crude oil and sand were air-dried and then weighed to determine crude and sand content. After weighing, the filter papers, crude oil and sand were returned to funnel-beaker array and transferred to a fume chamber from where chloroform was poured over to dissolve the oil to pass through the filter. After drying, the filter papers and the sand were weighed. A detailed filtration-drying-weighing sequence is given in Appendix C.

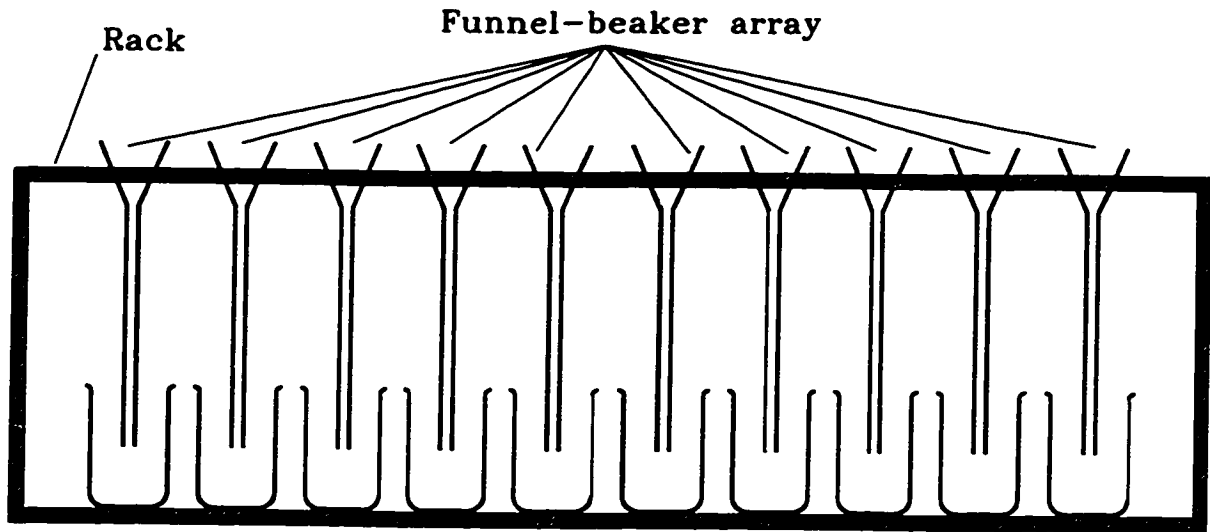


Fig. 4.7: A Ten Funnel-beaker Arrangement for Sample Gravimetric Analysis.

Prior to all separation tests, calibration of measurement devices was done. The iso-kinetic sampling units were calibrated by closing the valves at overflow and trans-flow and running the suspension through the feed and underflow sampling units. In this configuration both streams should remain at feed conditions. Seven samples from each probe were taken using 30 second intervals between feed and underflow stream sampling. Analysis of the seven samples for the underflow indicated mean concentrations of 852 and 876ppm for crude oil and quartz sand respectively. These results compared favourably with the computed feed mean concentrations of 840 and 886ppm for crude oil and quartz sand based on the same analysis and the initial amount of crude oil and sand charged to the system, giving confidence to the sampling and gravimetric procedures. The calibration tests for the iso-kinetic sampling units indicate that the feed concentration remains approximately constant over the duration of the experiment. In subsequent tests only two feed samples were taken, one at the beginning of each test and another at the end of a test run.

Droplet/particle analysis was performed by a Malvern droplet/particle coupled to a PC. The quartz sand analysis was carried out using the regular LASER cell but analysis

for oil droplets required a special cell. Therefore, a 50 by 25 by 75mm top-open rectangular glass cell was constructed from 75 by 50mm metallurgical glass slides. The capacity of the cell was about 100mls. Two parallel sides 25mm apart were kept to avoid distortion of the laser beam. Detailed description is found in Appendix D. The cell was filled with the sample to be tested and placed in between the LASER torch and the receiver. A sketch arrangement is given in Fig 4.8.

The rectangular cell was calibrated using a sample with a known size distribution (quartz sand used) in the regular cell and also in the designed cell. They all had same distribution. Feed samples were divided into 10 samples for measurements. 20mls of the overflow was also measured. The subdivided quartz sand and crude oil samples were placed in the rectangular cell. A small magnetic stirrer bar, in the cell, was used to stir the sample to expel air and to maintain droplets and particles suspended. With the particles settled at the bottom of the cell, the droplets in suspension scanned by the Laser radiation. The residual sand, from gravimetric analysis, was used in the particle size measurements since it contained no oil. Distilled water was added to the dry sand in the cell and the measurement repeated as above.

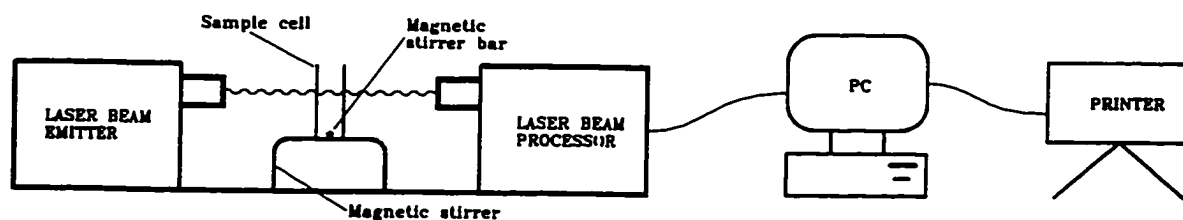


Fig. 4.8: Schematic of a Laser Droplet and Particle Sizer.

## Chapter 5

### 5.0 RESULTS AND DISCUSSION

As discussed in Chapter 1, separation tests were conducted to determine the influence of concentrations of dispersed phases on performance parameters of the three-phase separation hydrocyclone. The separation results in this section were obtained using dispersions of Forties crude and quartz sand in tap water. The droplet/particle size density distributions were determined using a Malvern Droplet and Particle Sizer S2600. On-line performance of three-phase hydrocyclone was monitored by an optical microscope.

By hypodermically injecting organic dyes, flow visualization was conducted to determine areas of high particle/droplet concentration within the flow domain and short-circuit behaviour. Modelling for velocities was done and the computed results compared with experimental data in the literature.

As discussed the hydrocyclone in the current study can double function as a two-phase and three-phase separator when the transflow is closed and opened respectively. Theoretical and experimental modelling was conducted with the hydrocyclone in both modes. Detailed experimental and computational data are attached as Appendix A.

#### 5.1 Separation Tests

The separation results in this section were obtained using dispersions of Forties crude (SG = 0.83), dynamic viscosity of 23 mPas and quartz sand (SG = 2.65) in tap water at an ambient temperature of 20°C.

##### 5.1.1 Efficiency Data

In two-phase mode, separation was observed using dispersed crude oil in water. The bulk of the crude oil separated from the overflow while the water separated in the underflow. In three-phase mode, the dispersions of oil and sand in water were used. It was

observed that the oil and sand separated from the overflow and transflow respectively. The oil and sand efficiencies were computed using Eqs. 2.31 and 2.33.

Fig. 5.1 shows the effect of split ratio on hydrocyclone efficiency for a dilute feed stream. Highest efficiency of 88% was obtained at  $\Lambda = 0.2$ . Efficiency peaks were observed to occur in the feed discharge range of 3.6 - 4.2 m<sup>3</sup>/hr. The efficiency peaks can be attributed to the fact that at high flowrate the centrifugal forces are too strong for oil to separate. Another observation was that efficiencies increased with increase in feed flowrate and vice-versa. Values of  $Q$  between 2.0 and 4.2 m<sup>3</sup>/hr caused a stable vortex and separation of the various three-phase mixtures fed into it.  $Q$  is crucial to separation since it determines the strength of the vortex and hence the trajectory of individual particles.

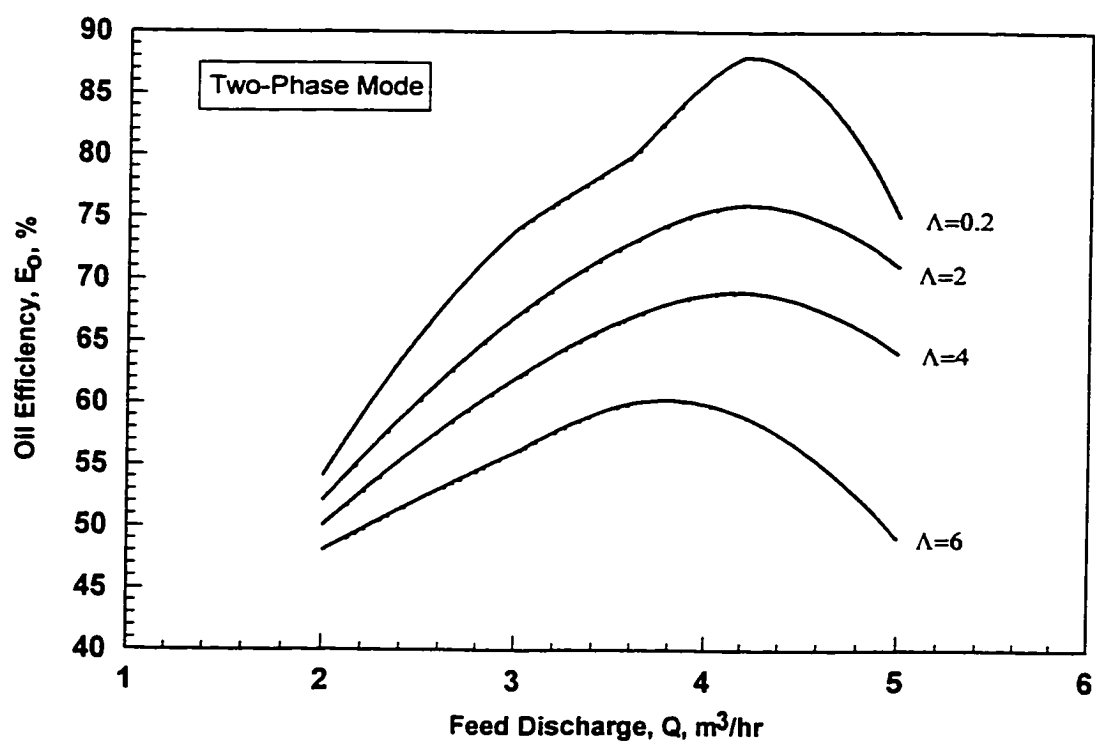


Fig. 5.1: The Effect of Inlet Flow Rate on Oil Efficiency  $C = 0.1\%$  Feed.

Fig. 5.2 shows the observation made in a three-phase hydrocyclone. As a dilute (0.1%) feed discharge was increased the efficiencies of both oil and sand increased but started dropping at a value of  $Q=4 \text{ m}^3/\text{hr}$ . At this value and above the sand efficiency gradually dropped while the oil efficiency dropped sharply. The observation can be attributed to the rupture of oil droplets at high values of  $Q$  causing or degenerating its efficiency.

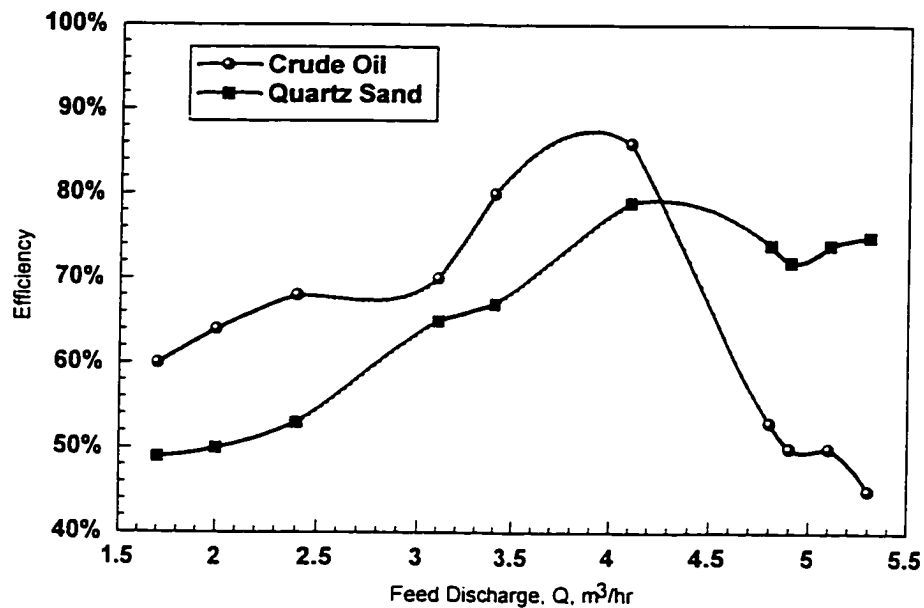


Fig. 5.2: The Effect of Feed Discharge on Three-phase Efficiency at  $\Lambda = 0.2$ ,  $C=0.1\%$  Feed.

As the feed concentration is increased, the efficiencies in both two-phase and three-phase modes degenerate as shown in Figs. 5.3-5.5. This may be attributed to bombardment and interaction of particles/droplets.

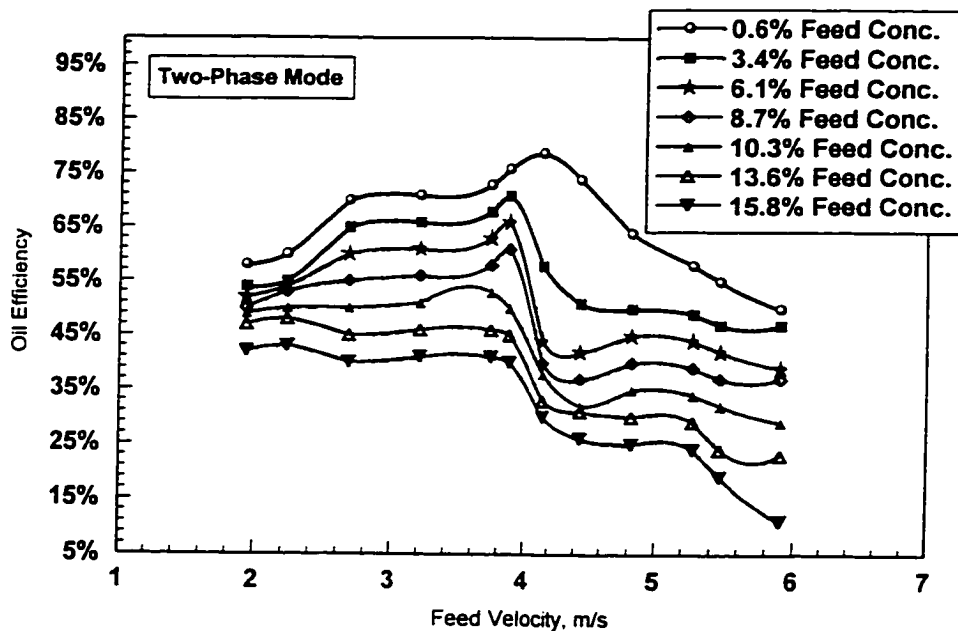


Fig. 5.3: Influence of Feed Concentration on Oil Efficiency,  $\Lambda=0.2$ .

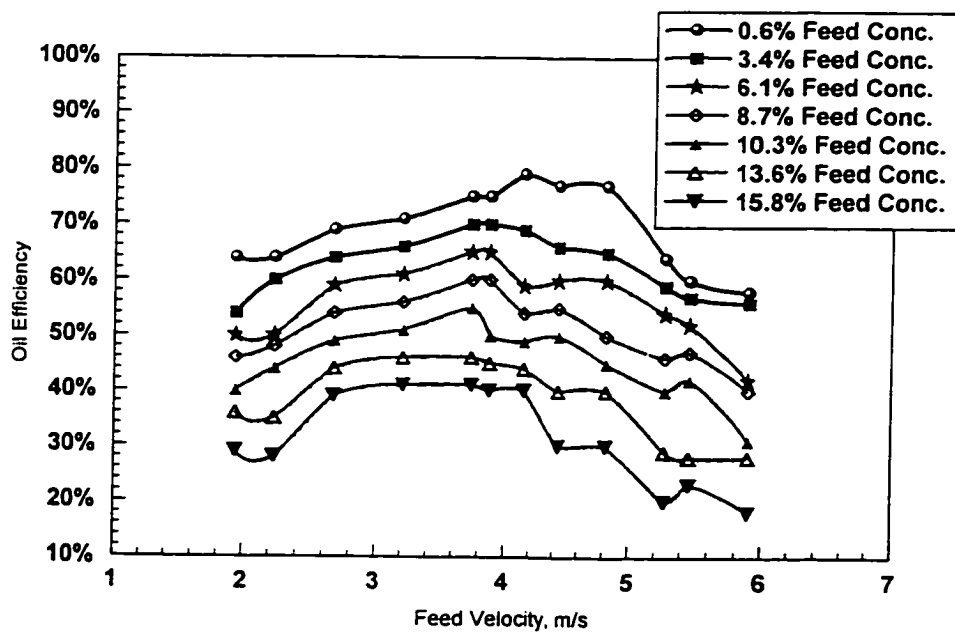


Fig. 5.4: Influence of Feed Concentration on Three-phase Oil Efficiency.



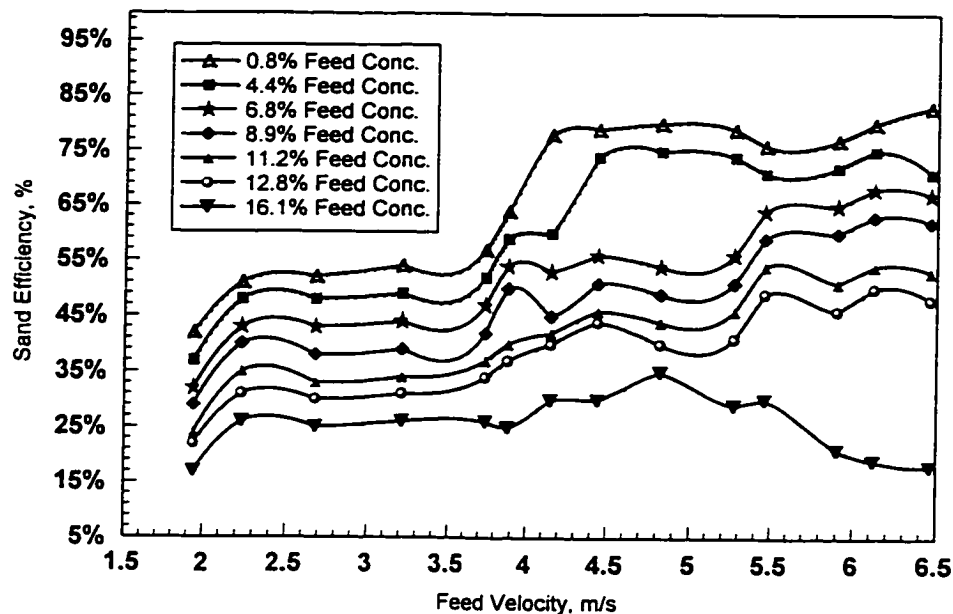


Fig. 5.5: Influence of Feed Concentration on Three-phase Sand Efficiency.

### 5.1.2 Pressure Drop Data

The pressure losses across a hydrocyclone are a direct measure of the operating costs of the device. The pressure drop-flow rate data reported in this section were observed at the minimum values of  $S_0$  corresponding to the stability curves in Figure 5.12.

The influence of feed solids concentration on the pressure drop across the hydrocyclone is shown in Figs. 5.6-5.8 for inlet velocities of 2, 4 and 6 m/s, respectively. At the lowest velocity, the pressure drop increases only marginally with both the feed concentration and the flow ratio. At higher flow rates, the pressure drop increases substantially with both, the feed concentration and the flow ratio. This may be attributed to the reversal of axial velocity of a large part of the feed flow further down in the conical section of the hydrocyclone. At inlet velocity of 6 m/s, the pressure drop at large flow ratios increases additionally because separated particles are re-entrained by the upward flow. This re-entrainment occurs once the capacity of the transflow aperture fails to cope with the

amount of solids, separated as a result of centrifugal action which increases in proportion to the feed rate, has been exhausted. The pressure drop will increase even further once rotating bed of solid particles has formed on periphery of the transflow aperture since the free vortex becomes shorter and the friction losses increase.

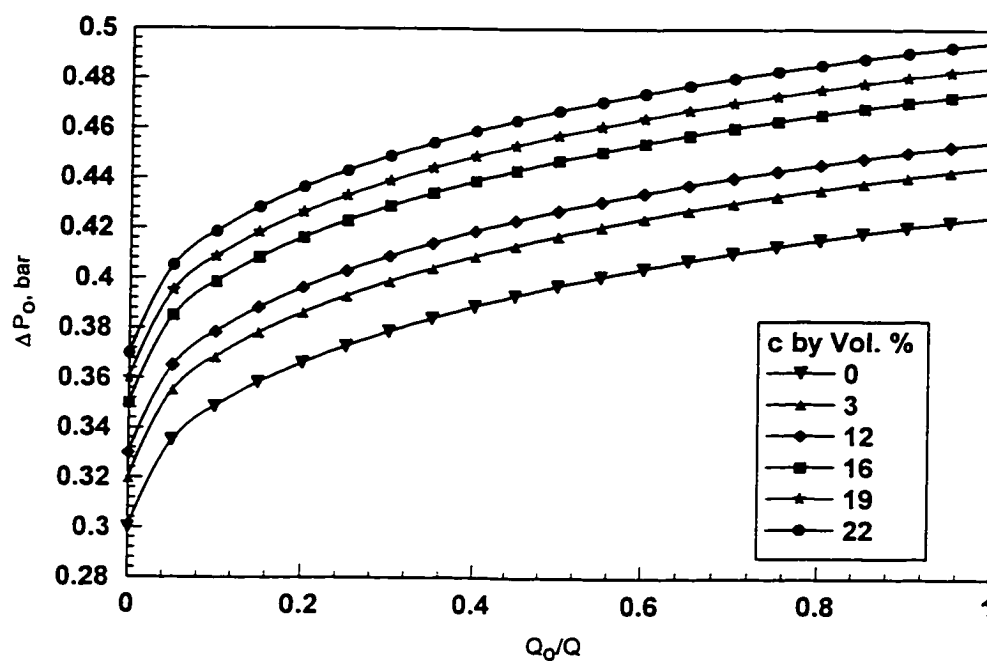


Fig. 5.6: Pressure Drop At an Inlet Velocity of 2 m/s.

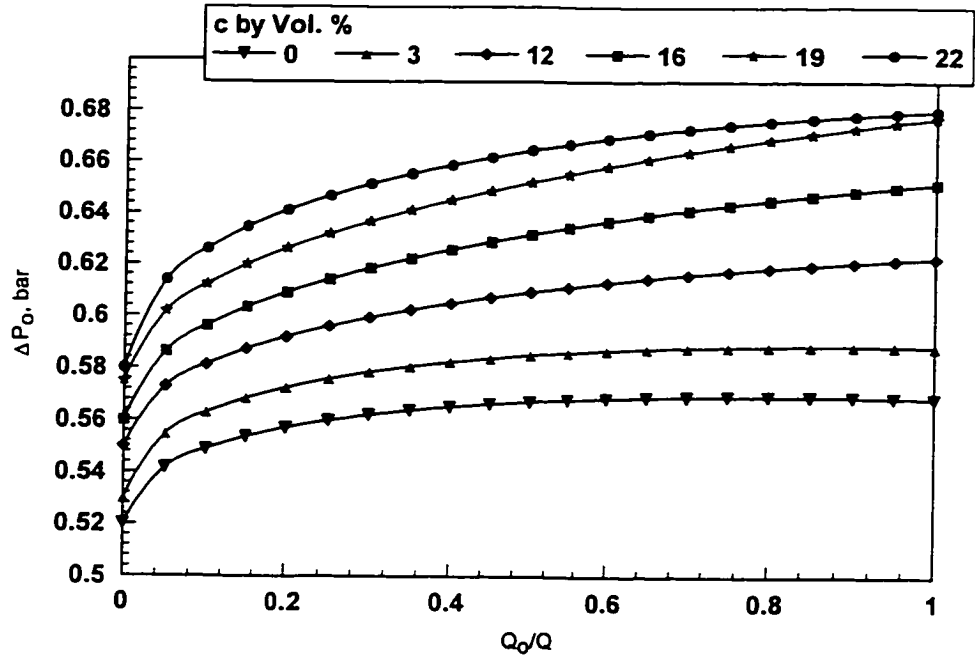


Fig. 5.7: Pressure Drop at an inlet velocity of 4 m/s.

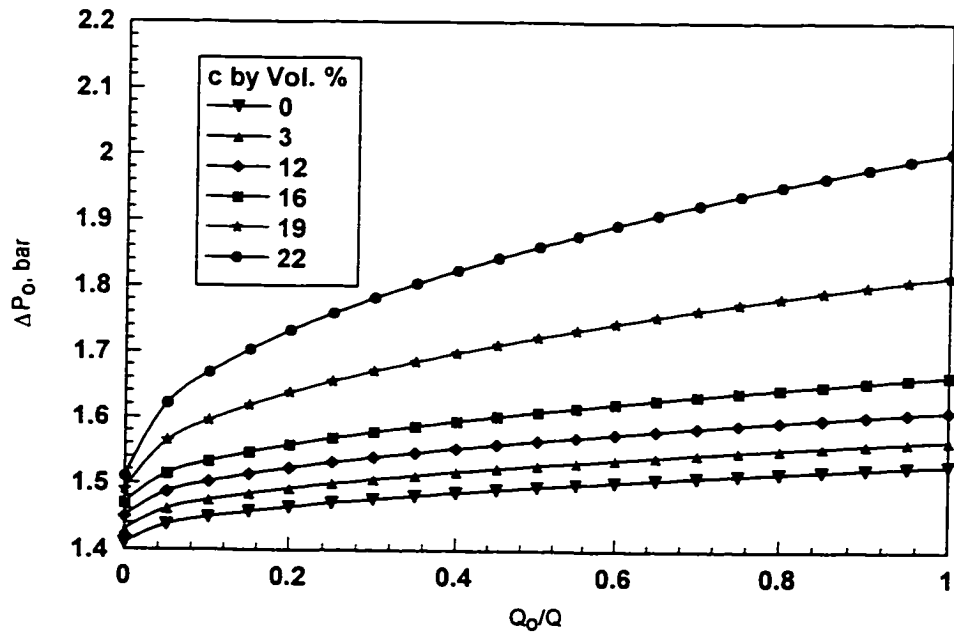


Fig. 5.8: Pressure Drop at Inlet Velocity of 6 m/s.

The dimensionless groups chosen to represent this data are the pressure drop coefficients and the feed Reynolds number defined in Eqs. 2.41 - 2.46. In Eqs. 2.41 - 2.46, if the term in the brackets is constant the pressure drop coefficients vary inversely as the square of the Reynolds number.

For instance in the current study, a dilute slurry has the following parameters:

$$\text{Density} = 1,000 \text{ kg/m}^3$$

$$\text{Dynamic viscosity} = 1 \text{ (cp) mPas} = 10^{-3} \text{ Ns/m}^2.$$

$$\text{Kinematic viscosity} = 1/1000 \text{ (cp) mPas} = 10^{-6} \text{ Ns/m}^2.$$

$$\Delta P_o = 2.0 \times 10^5 \text{ N/m}^2, \quad \Delta P_u = 1.5 \times 10^5 \text{ N/m}^2$$

$$\text{Hydrocyclone geometry, } D_i = 14 \text{ mm} = 14 \times 10^{-3} \text{ m}$$

$$C_{po} = \left( \frac{2 \times (14 \times 10^{-3})^2 \times 2 \times 10^5}{1000 \times (10^{-6})^2} \right) \frac{1}{Re^2} = \frac{7.84 \times 10^{10}}{Re^2}$$

Re values in the current study range from 21000 to 98000 at overflow pressure drop of 2 bars. With these data pressure drop coefficients can be predicted. The intensity of the fluid swirl at a given axial position is a function of the radial pressure gradient. The significance of measurement of the wall pressures at the inlet and outlets of the hydrocyclone is that it gives a gross measurement of the conversion of pressure energy of the fluid into rational energy that is useful for centrifugal separation.

Figure 5.9 shows the plot of the pressure drop coefficient versus feed Reynolds number for the three-phase hydrocyclone in both modes. The pressure drop coefficient while operating in two-phase mode is nearly double that in three-phase mode. This higher pressure loss indicates a difference in the internal flow structures of the hydrocyclone in both modes. This is consistent with the observation of the incoherence of the particle core near large taper section apex in the two-phase mode of the hydrocyclone. The coherence of the particle core throughout the entire length of the current hydrocyclone in three-phase mode, coupled with a lower pressure loss coefficient, suggests that the function of the fine taper is to conserve angular momentum without creating secondary flows, resulting in a

lower pressure losses. All the observed pressure loss coefficients are practically dependent of the feed Reynolds number, indicating that the viscous losses are significant as compared to centrifugal head losses.

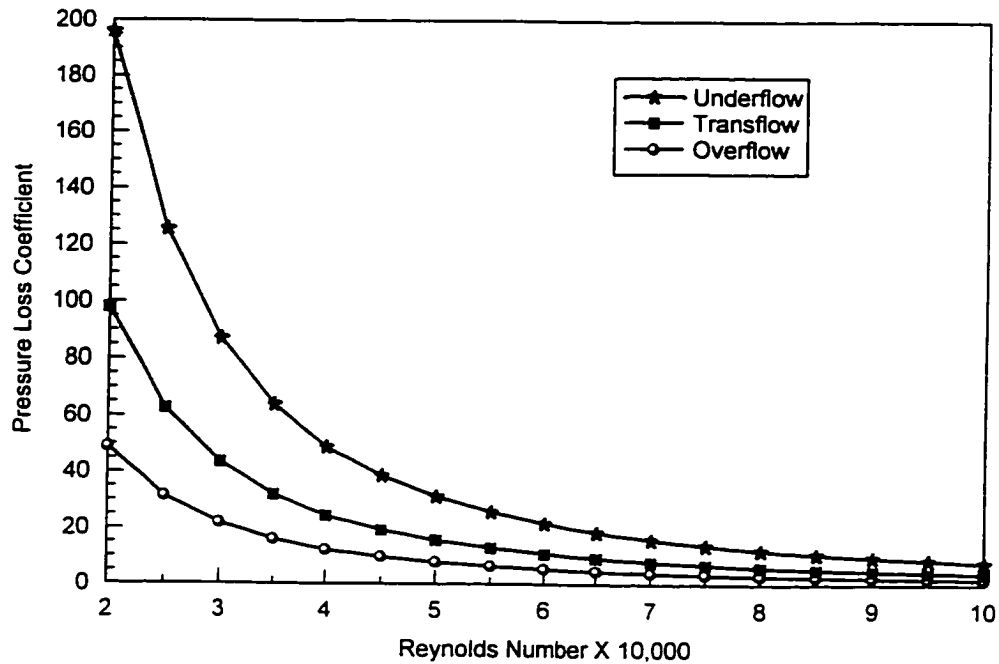


Fig. 5.9: A Family of Computed Pressure Drop Coefficients in a dilute feed.

Fig. 5.10 shows the influence of feed concentration on pressure drop coefficients. The pressure coefficients vary inversely with the square of Reynolds number. The curves are found to be asymptotic to Re-axis. Just as in Figs. 5.6-5.8, this behaviour can be explained in terms of rotating bed of solid particles forming on periphery of the transflow as free vortex becomes shorter and increase of frictional losses. The significance of curves is that they can help to determine the operating pressure drop and thus the corresponding design.

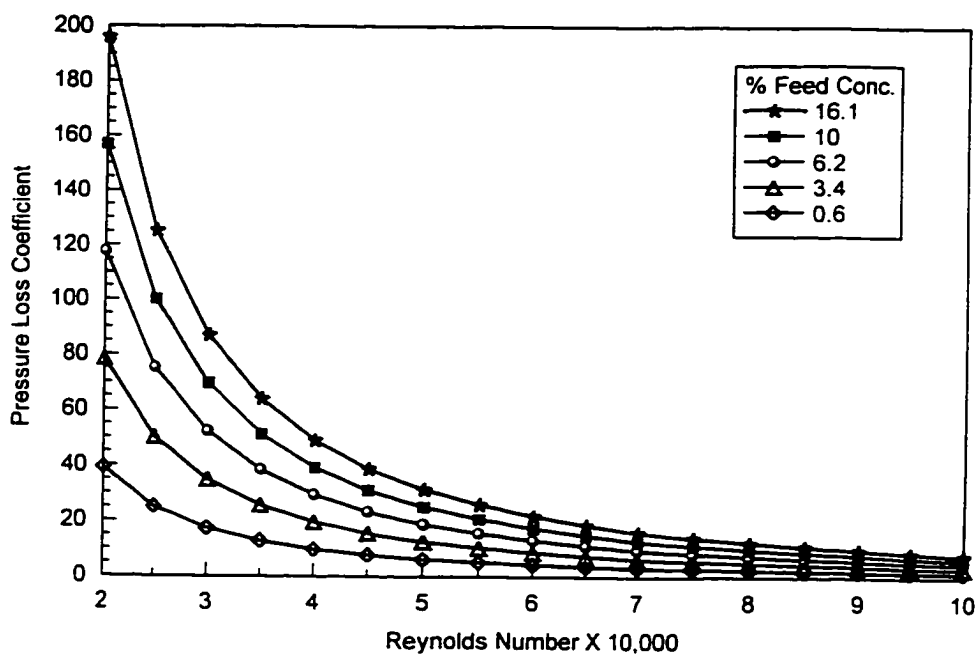


Fig. 5.10: Effect of Feed Concentration on Pressure Drop Coefficients.

## 5.2 Fluid Flow Visualization

After satisfactory alignment, the flow rates were readjusted and the hydrocyclone was operated without an air core for the entire set of experiments described herein. Instead, it was operated with an oil core several centimetres long in the axial direction and along the true axis of the hydrocyclone. This initially served as an alignment reference.

### 5.2.1 Reverse Flow Vortex Stability

The stability of the reverse flow vortex for the three-phase hydrocyclone studied was found to be a dynamic phenomenon. Instabilities in the reverse flow vortex manifested themselves over periods of time from 10 seconds to 20 minutes, depending on the operating conditions. Uniquely, the particle core existed for the entire length of the hydrocyclone. The diameter of the particle core increased with increase in feed concentration but never exceeding the overflow diameter for stable conditions (see Fig.5.11) i.e., the vortex amplitude,  $\eta$ , is such that:

$$|2\eta| \leq D_o$$

Vortex amplitude measurements were made along the axial length of the hydrocyclone. The absolute values are plotted as shown in Fig. 5.11. Notice that in Fig. 5.11 the curve corresponding to inlet velocity of 1.8 m/s has exceeded the overflow diameter. This is due to instabilities of the reverse flow vortex.

Flow conditions corresponding to good separation efficiencies could be determined by observing the behaviour of the reverse flow vortex<sup>21,57</sup>. These observations were confirmed in the current study. The reverse flow vortex behaviour can be easily visualized because light dispersed phase particles migrate toward the core and are captured in the jet-like flow. Fig. 5.12 summarizes the observed operating regimes for the three-phase hydrocyclone. The three operating regimes include: 1) an unstable inlet flow; 2) a stable reverse flow; and, 3) a transient reverse flow.

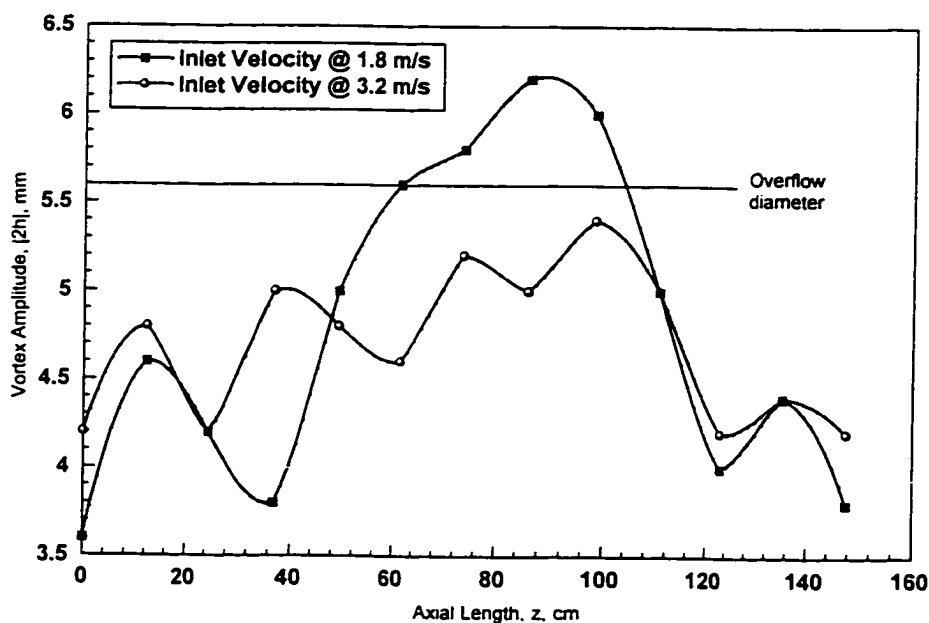


Fig. 5.11: Effect of Inlet Velocity on Absolute Vortex Amplitude.

The threshold inlet velocity, 1.7 m/s, represents an operating condition for the loop at which the pump would not deliver a steady volumetric flow to the hydrocyclone test section. The two stability boundaries in Fig. 5.12 were obtained by visual observation of the particle core. The underflow and transflow valves were left fully open, giving fixed underflow and transflow resistances, respectively, for all experiments reported in the current study. At each selected value of the feed velocity, the overflow valve was opened incrementally from the fully closed position. If instabilities in the reverse flow vortex resulted in a transition from reverse flow vortex to a through flow vortex, the overflow valve was opened further. This procedure was continued until no instabilities occurred. The criterion used for stability was on longitudinal pulsations or any thickening of the particle core within twenty minutes of setting the overflow valve position.

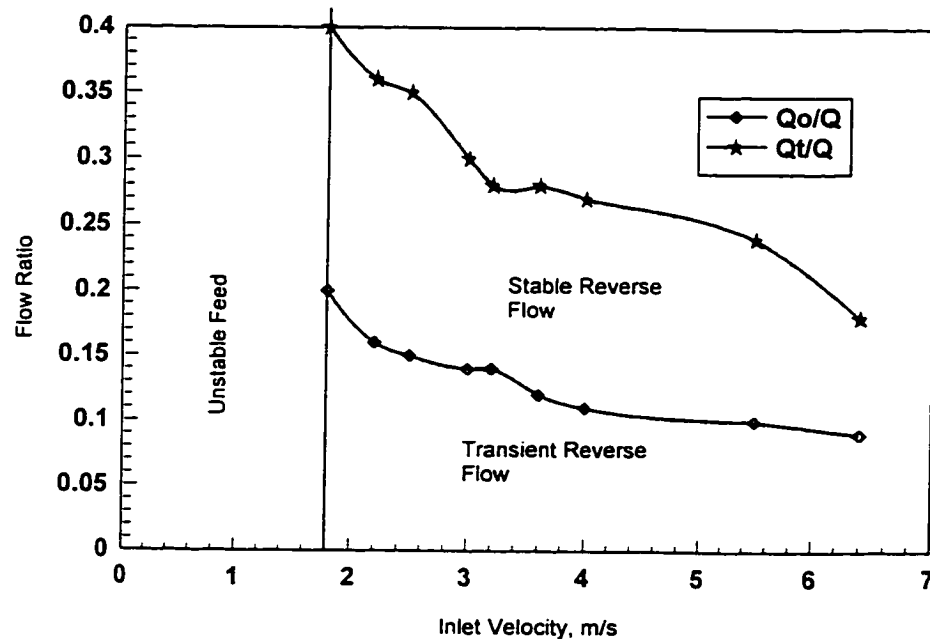


Fig. 5.12: Operating Zones for Three-Phase Hydrocyclone.

This time limit was chosen for practical considerations. After determining the minimum overflow and transflow ratios for a given feed velocity, the stability of the reverse flow vortex was further checked by momentarily clamping down on the overflow hose, creating



a pressure pulse in the overflow line. If the core remained in a stable reverse flow, the coordinates of the operating point were noted. The points comprising the stability curves locate specific values of  $v_i$ ,  $\Lambda_o$ ,  $\Delta P_i$ , and  $\Delta P_u$  which are marginally stable.

The transient reverse flow regime indicates the combinations of  $\Lambda_o$ ,  $\Lambda_i$  and  $v_i$  that resulted in an eventual transition from a reverse flow vortex to a through flow (concurrent with the main flow) vortex. For three-phase hydrocyclone design, the transient reverse flow regime consists of all points below the marginal stability curve. The stability operating regions consist of region above the stability curves. The upper bound for each region was determined by the "natural" overflow ratio, occurring when the overflow, transflow and underflow valves were in fully opened position. As Fig. 5.12 shows, the maximum values of the overflow ratio obtained were 0.15 and 0.09. Also, the stable operating region in the two-phase mode is narrower than that in the three-phase, but occurs at lower values of  $\Lambda_o$  over the range of feed velocities studied.

Firstly, what appeared to be a stable reverse flow vortex occurred. The particle core resembled a thin strand of cord along the hydrocyclone axis, somewhat helical in shape as shown in Fig. 5.13A. In both modes of operation studied, the motion of groups of solid particles indicated the axial flow of the vortex to be toward the overflow orifice over most of the vortex length. In the region near the underflow orifice, the direction of the inner vortex axial flow could not be determined. Some incoherence of the particle core could be seen between the cylindrical underflow section and the large taper section. This incoherence may be due to a secondary (eddy-type) flow caused by the continuance of the  $10^\circ$  taper angle to the underflow diameter over a short distance.

The second stage of the transition begins with longitudinal pulsations of the particle core originating from near the underflow orifice and continuing toward the overflow orifice (see Fig. 5.13B). This event was accompanied by a general thickening of the particle core, also observed by Colman<sup>57</sup>. The reverse flow particle core was not observed to break up as it proceeded toward the overflow orifice and remix with the feed flow as noted by Colman<sup>57</sup>. Instead, the particle core was observed to thicken until its diameter

exceeded that of the overflow orifice, accompanied by a sudden increase in the overflow stream pressure and chocking of the overflow stream. This thickening was followed by the third stage of the transition; a sudden transformation of the inner vortex from a reverse flow to a through flow vortex (see Fig.5.13C). At this point the overflow ratio  $\Lambda_o$  was essentially zero. Some observations of the reverse flow to through mode were accompanied by the entrainment of a small amount of air into the inner vortex, but this was not true in general. Also, in some experiments, the third stage of transition was characterized by three to four consecutive transitions from reverse flow to through flow and back to reverse flow. In these cases, the final result was always a stable through flow inner vortex. The stability associated with Fig. 5.13 is that it can enable the operator optimize the separation

The transition from reverse flow vortex to through flow vortex occurred on different time scales, depending on the initial coordinates  $(v_i, \Lambda_o)$  of hydrocyclone operation. In general, the further below the stability curve, the shorter the period of time that elapsed before the transition.

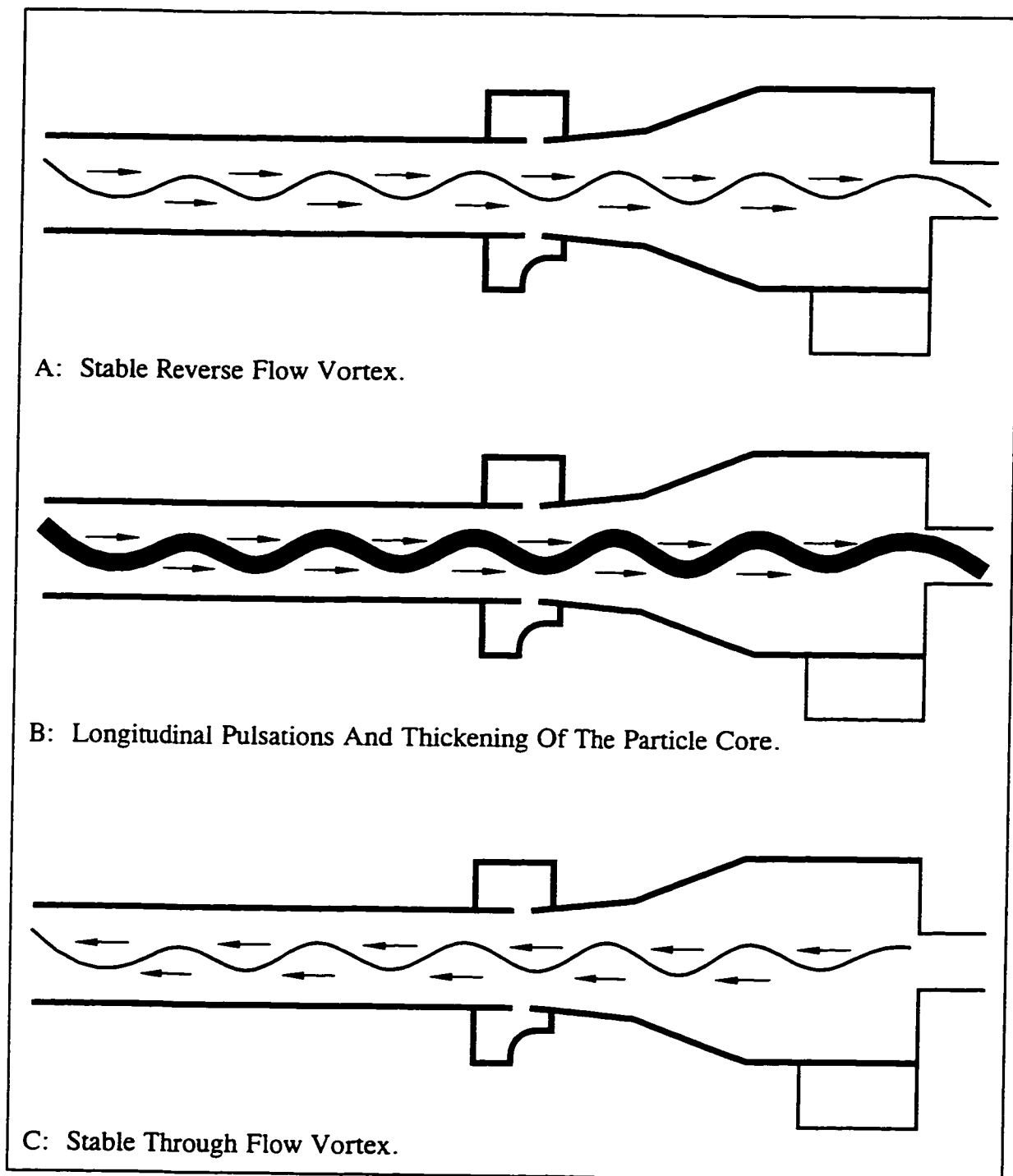


Fig. 5.13: Succession of the Reverse Flow Vortex.

### 5.3 Computed Velocity Spectra

The Reynolds number of the inlet flow determines the velocity spectra, i.e., the momentum of the fed flow is distributed into the tangential, axial and radial directions. Velocity spectra will be presented as axial, tangential and radial spectra.

#### 5.3.1 Axial Velocity Spectra

Fig. 5.14 shows the axial velocity profiles at the level  $z = 20 - 320$  mm in the hydrocyclone with flow split ratios varying from 0 to infinity. As the flow split ratio is increased, the depth of the dent in the centre of the axial velocity profile is reduced and the positive (upward) portion of the velocity profile is increased. Fig. 5.15 indicates the influence of  $Re$  on velocity spectra. At  $z = 60$  mm and higher values of  $Re$  the oil ruptures forming an emulsion which has a profound effect on velocity.

#### 5.3.2 Tangential Velocity Spectra

Figs. 5.16 shows the influence of Reynolds numbers on computed tangential velocity spectra at  $z = 100$  mm. As  $Re$  increases the spectrum peak increases. The tangential velocity component is zero at the centre, increases sharply with the radius, to a maximum value, and then gradually decreases as it approaches the hydrocyclone wall where it becomes zero. This central viscous region of the vortex is characterized by a linear variation of the tangential velocity. The variation of the flow split ratio can have a profound effect on the shape of the velocity components.

#### 5.3.3 Radial Velocity Spectra

Fig. 5.17 shows the radial velocity profiles at the level  $z = 80$  mm in the hydrocyclone with flow split ratios varying from 0 to infinity.

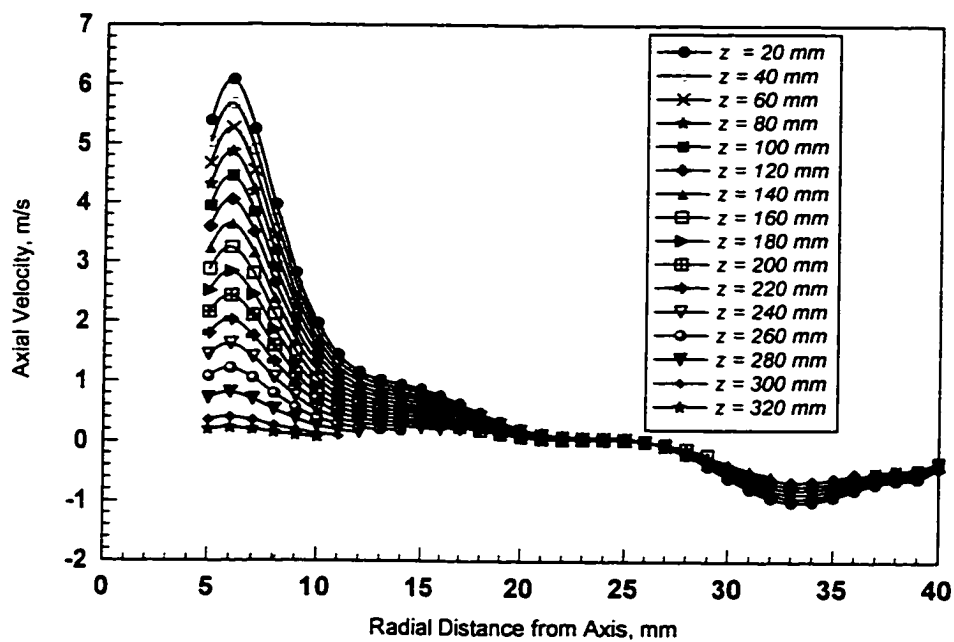


Fig. 5.14: A Family of Computed Axial Velocity Spectra.

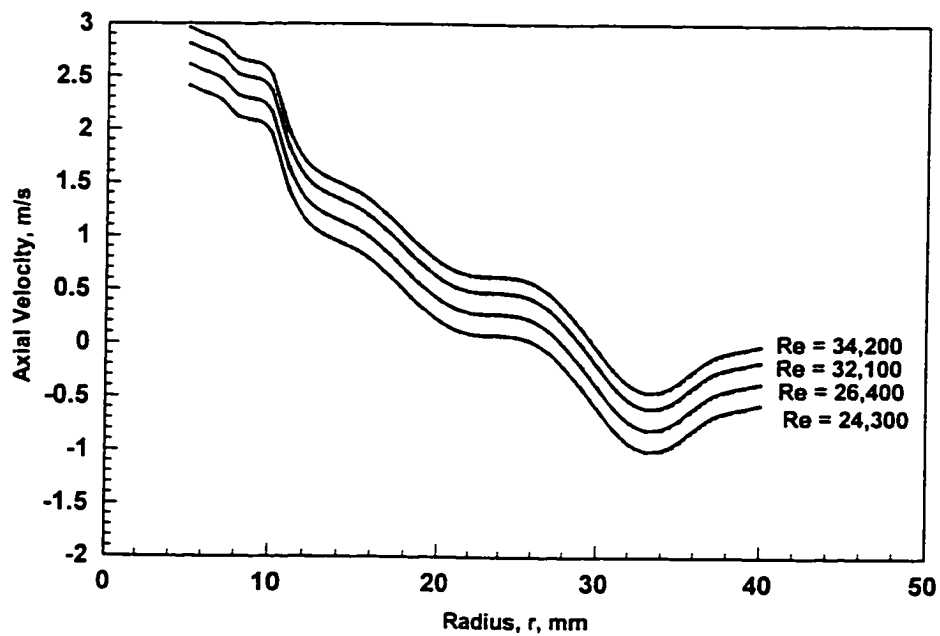


Fig. 5.15: A Family of Computed Axial Velocity Spectra at  $z = 60$  mm.

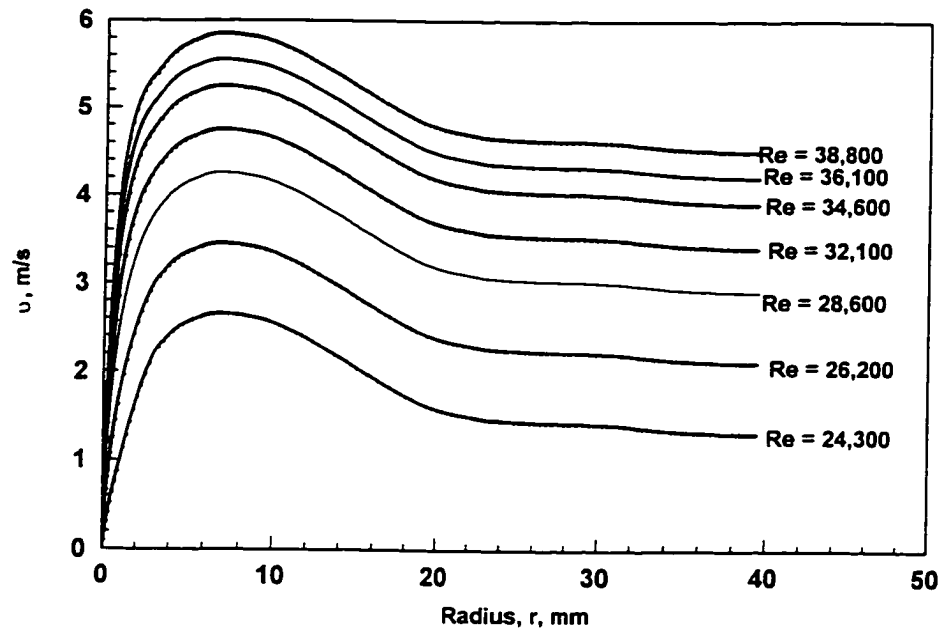


Fig. 5.16: A Family of Computed Tangential Velocity Spectra at  $z = 100$  mm.

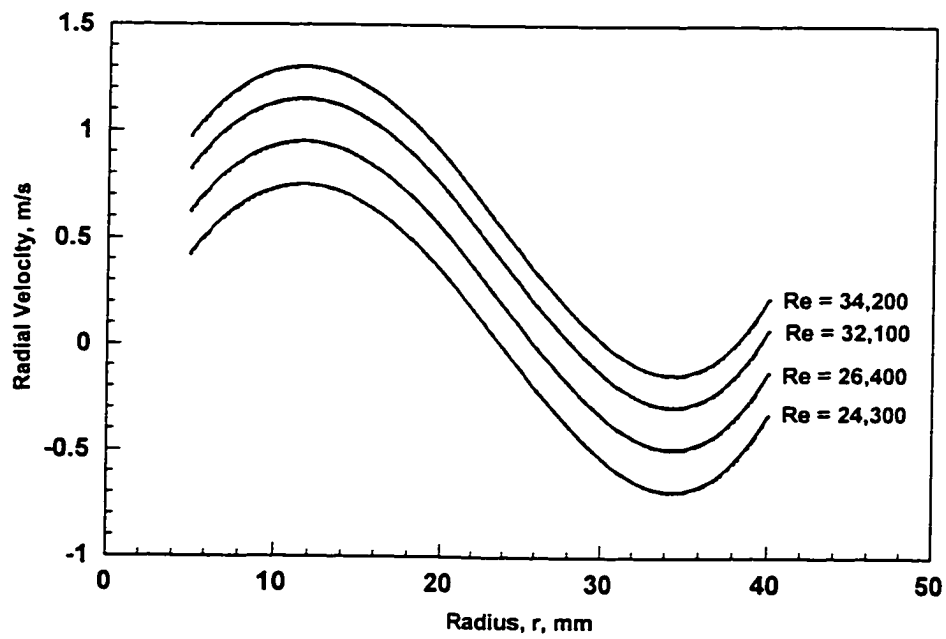


Fig. 5.17: A Family of Computed Radial Velocity Spectra at  $z = 80$  mm.

#### 5.4 Droplet/Particle Size Statistical Analysis

In order to characterise the dispersions, the droplet and particles size distributions were measured and statistically analyzed. Using samples obtained iso-kinetically, the distributions of droplets and solids in the feed and in the products were measured with a Malvern Droplet and Particle sizer 2600 series.

In order to analyze droplet/particle sizes, statistical analysis was performed. Goodness-of-fit tests (GOF) were done to fit distributions to oil droplets and sand particles. A goodness-of-fit test is a statistical hypothesis test (see Law and Kelton<sup>86</sup>) that is used to assess formally whether given data are an independent sample from a particular fitted distribution. That is, a goodness-of-fit test can be used to test the null hypothesis that given data are an independent sample from a known distribution. Some of the different goodness-of-fit tests for testing a null hypothesis are the chi-square, the Kolmogorov-Smirnov, and the Anderson-Darling tests. Details of the statistical analysis are provided in Appendix E.

The statistical analysis of the samples was carried out using UnifITII software<sup>87</sup>. For each experiment, oil and sand data in the feed and products were analyzed. The results are summarized and presented in Appendix A. Droplets and particles followed predominantly lognormal and gamma distributions whose parameters are part of the detailed statistical analysis provided in Appendix E. Svarosky<sup>88</sup> has discussed the distributions of particles and suspensions and recommends Lognormal distribution for oil and sand. The distribution is a two-parameter function, skewed to the right and it gives equal probability to ratios of sizes rather than to size differences.

The effect of droplet/particle size on efficiency is shown in Fig. 5.18 and particle distributions in the feed and transflow are shown in Figs. 5.19-20. The effect of droplet/particle was investigated by keeping the inlet feed constant. The increase in size increases efficiency for both cases. Crude oil increases to 81 % efficiency and drops. This is because the droplets were subjected to shear forces field tearing or breaking off. For the same size, in the range 19 to 62 $\mu\text{m}$ , sand has a higher efficiency of recovery

reaching an efficiency of 82%. This is because the separation of sand in the three-phase separator depends on how much of it is pushed to the boundary layer and this is dependent on their differential density with water. On the other hand, the oil-water differential density is very low for separation.

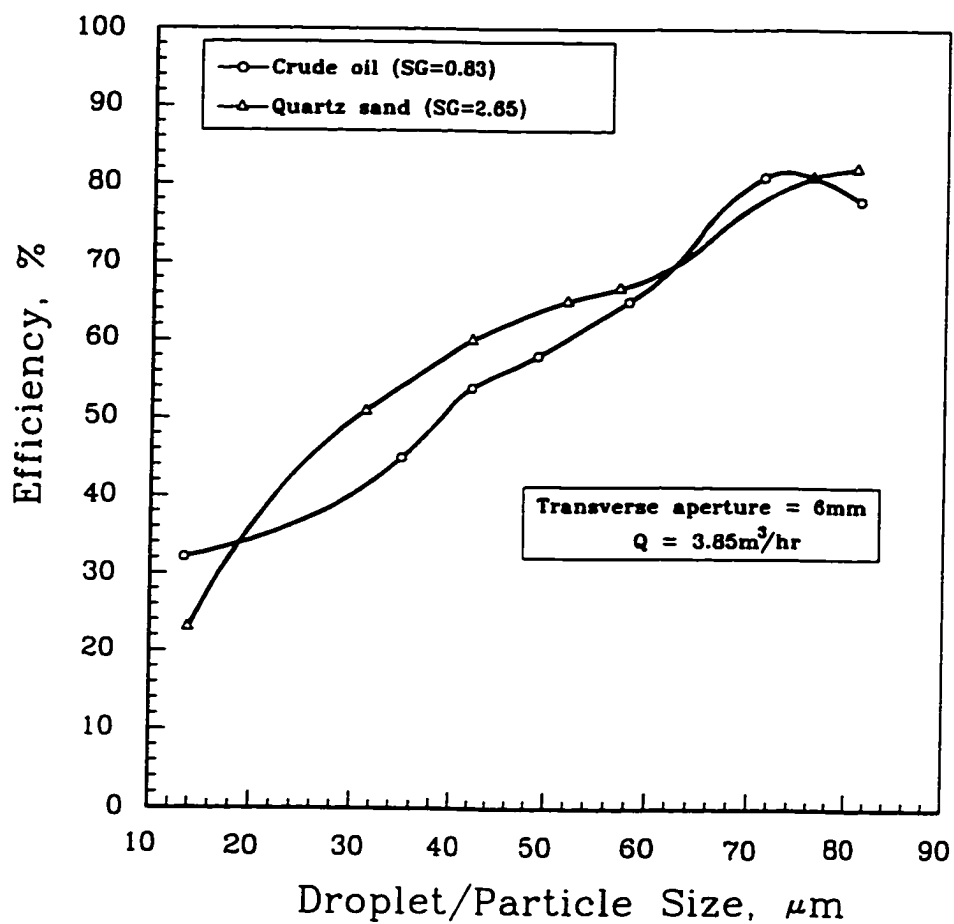


Fig. 5.18: The Effect of Droplet/Particle Size on Efficiency.



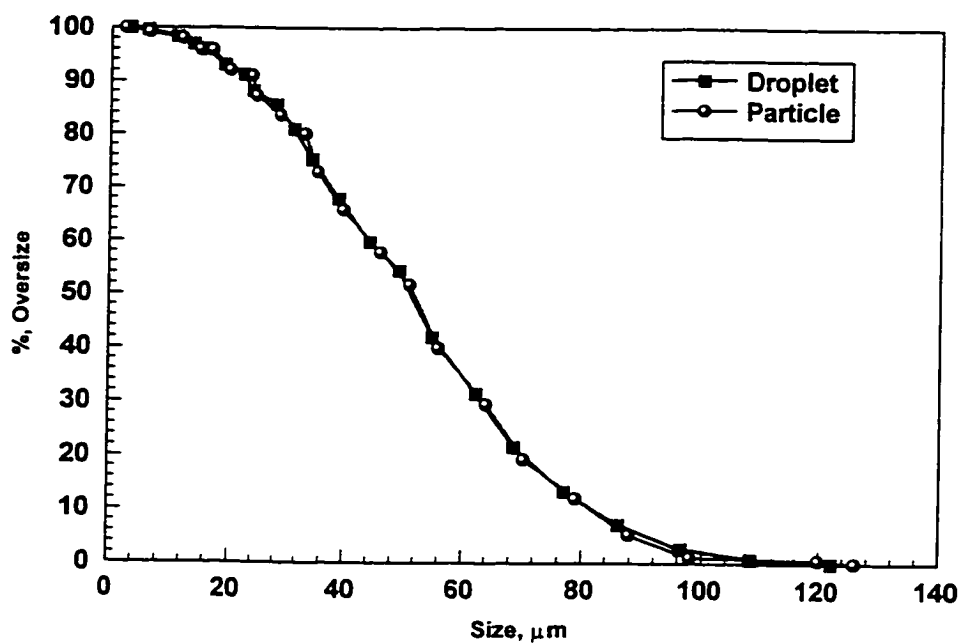


Fig. 5.19: Particle Distribution in the Feed.

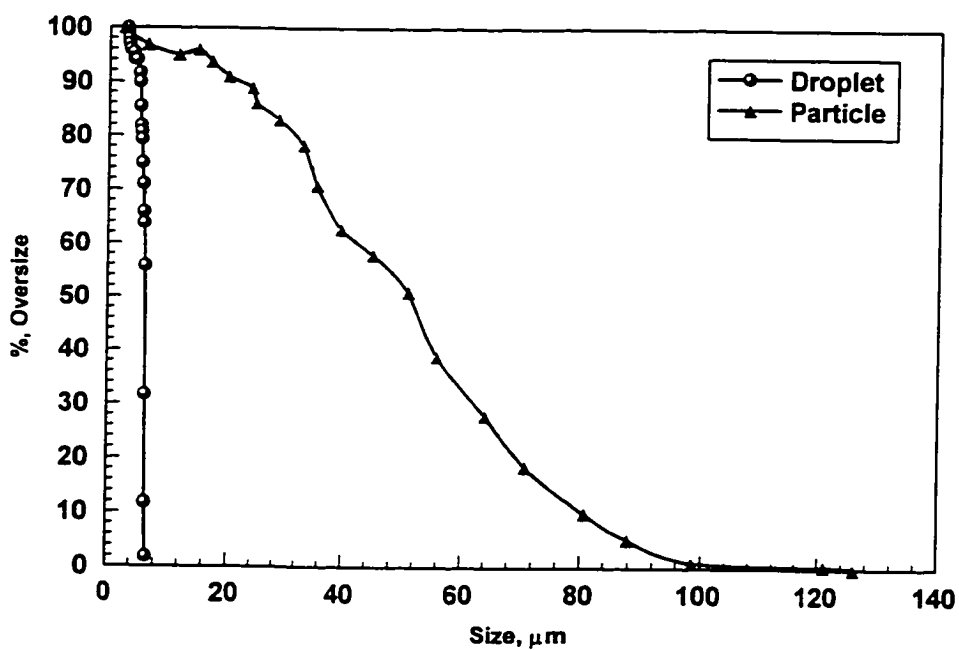


Fig. 5.20: Particle Distribution in the Transflow.

#### 5.4.1 Microscopic Examination of Droplets/Particles.

Feed and outlet stream droplet/particle sizes were required to determine the on-line performance of three-phase hydrocyclone. The droplets and particles were observed under an optical microscope. A close examination of these figures indicates that most of the particles were unchanged between the feed and trans-flow. The sand in the underflow stream had a fine and medium distribution.

#### 5.5 Comparison of Predicted and Experimental Results

Fig. 5.21 shows comparison of separation efficiency in the current design and that of Colman<sup>57</sup> for two-phase separation. The efficiencies in the current study compare well with his design giving confidence in operation of the three-phase design in two-phase mode

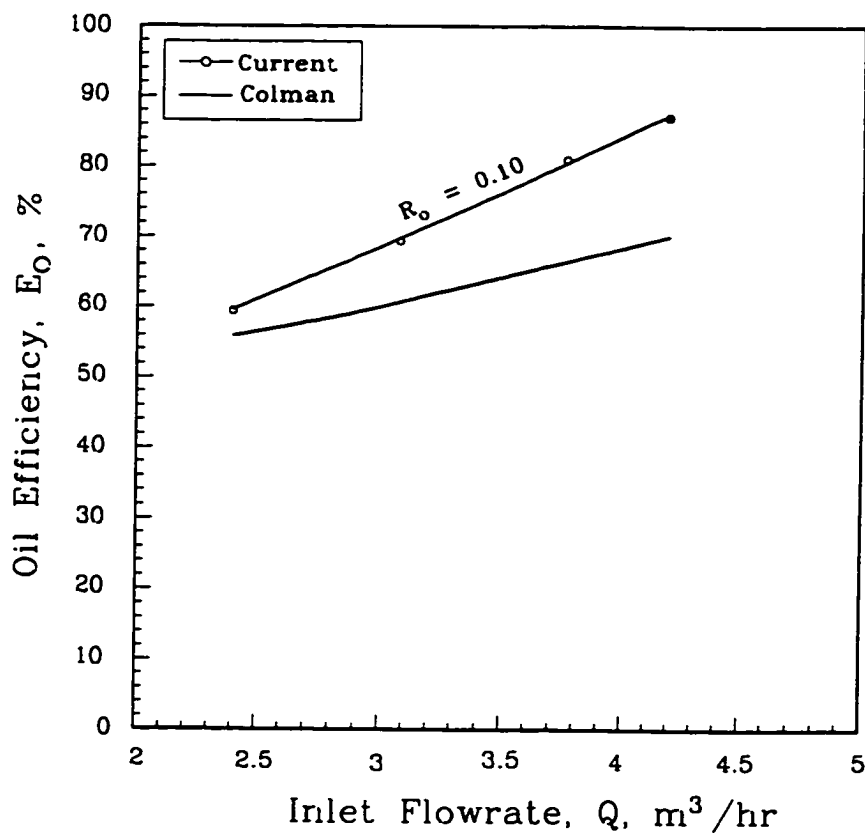


Fig. 5.21: Comparison of Experimental Separation Efficiency data with that of Colman<sup>57</sup>.

and three-phase mode too.

The pressure loss coefficients for the design by Colman<sup>57</sup> were replotted and is shown in Fig. 5.22. The curve indicates a higher pressure loss than was found in the current study, but this may have been due to the inclusion of pressure losses across a vortex breaker at the underflow orifice in his experiments. The vortex breaker was included to dissipate the fluid swirl, thus defining the separation length. In the current study, the underflow pressure was measured prior to the underflow valve. Observation of the flow downstream from the underflow valve showed no particles core, indicating that the valve had effectively dissipated the fluid swirl. The overflow pressure loss coefficients, not shown in Fig.5.22, are approximately twice as large as the  $C_{p_u}$  values given for the same design, suggesting that viscous losses are important for this smaller diameter orifice. This trend agrees with the observations of Colman<sup>57</sup>.

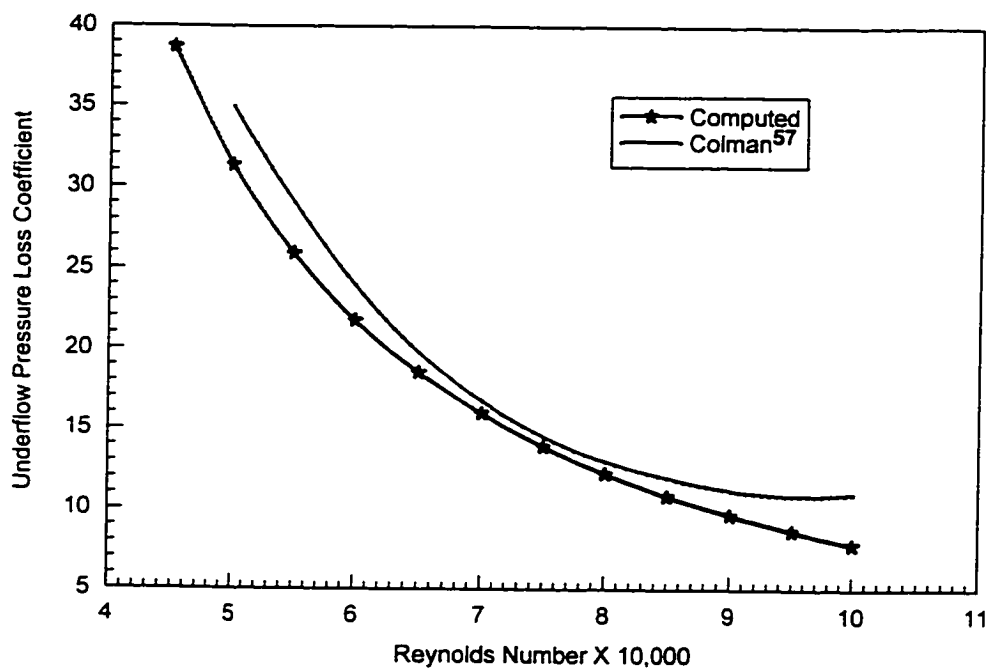


Fig. 5.22: Computed Underflow Pressure Drop Coefficients Compared with the data of Colman<sup>57</sup> at  $C=0.6\%$ .

The predicted and the experimental axial velocity profiles are compared in Fig. 5.23. In the inlet and the cylindrical section, it can be seen that the flow reversal and magnitude of

the axial flow are precisely predicted. In the conical part, however, some disturbances have been observed. This can be attributed to, first of all, a consistent lateral shift of locus of zero axial velocity. Secondly, the model predicts a thicker boundary layer at the oil core interface, which in turn varies the shape of the axial/velocity profile in that region. In the vicinity of apex, flows agreements between model predictions and experiments can be found again, which insures the accurate prediction of total volumetric flow through the apex.

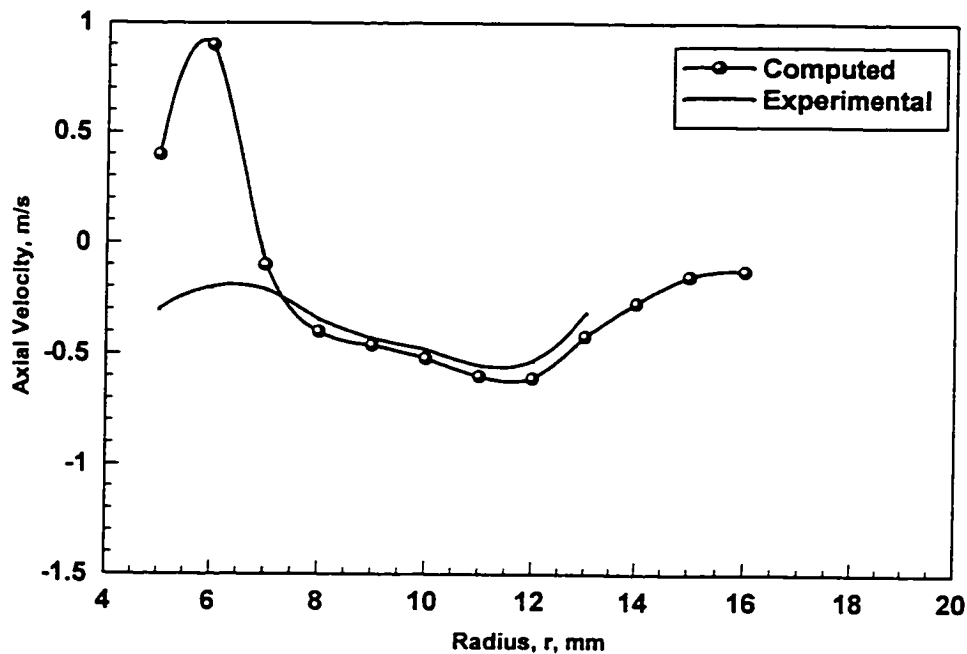


Fig. 5.23: Computed axial velocity profiles compared with the data of Dabir<sup>21</sup> at  $z=240$  mm and  $Re = 24300$ .

The hump in the computed velocity curve of the three-phase design can be attributed to the transitional free/forced behaviour at the attainment of reverse flow vortex stability at high flowrates.

The experimentally measured tangential velocity and the corresponding velocity profiles computed from the fluid/dynamic equation are shown in Fig. 5.24. The

experimentally observed force/free vortex is closely predicted by the model equations.

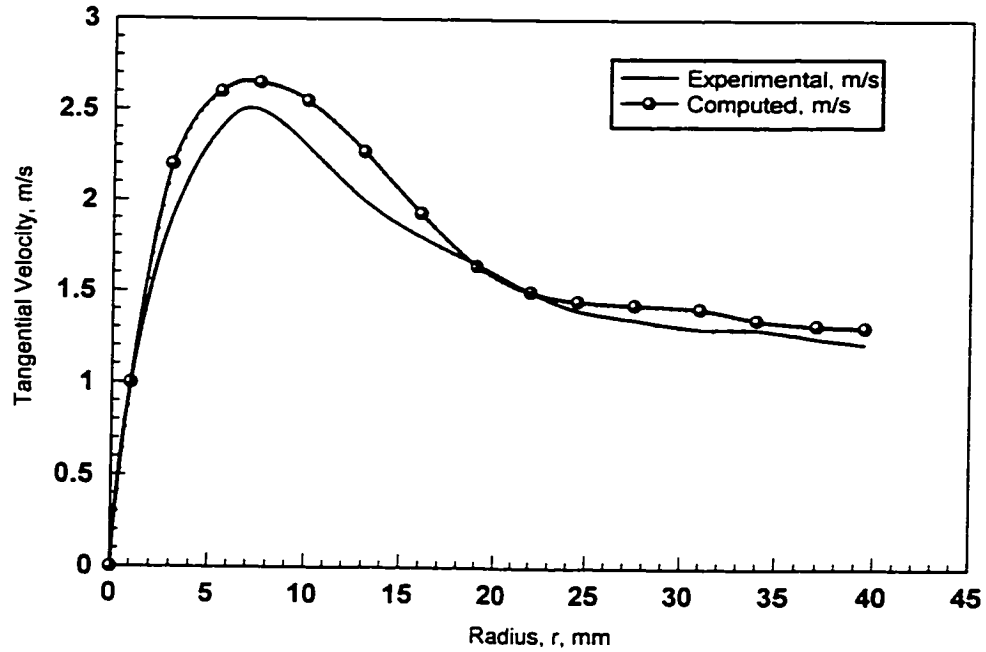


Fig. 5.24: Computed tangential velocity profiles compared with the data of Dabir<sup>34</sup> at  $z=60$  mm,  $Re = 24300$ .

Fig. 5.25 shows computed radial velocity profile with that of Hsieh<sup>17</sup>. The radial velocity profiles are in agreement with the values obtained by Hsieh<sup>17</sup>.

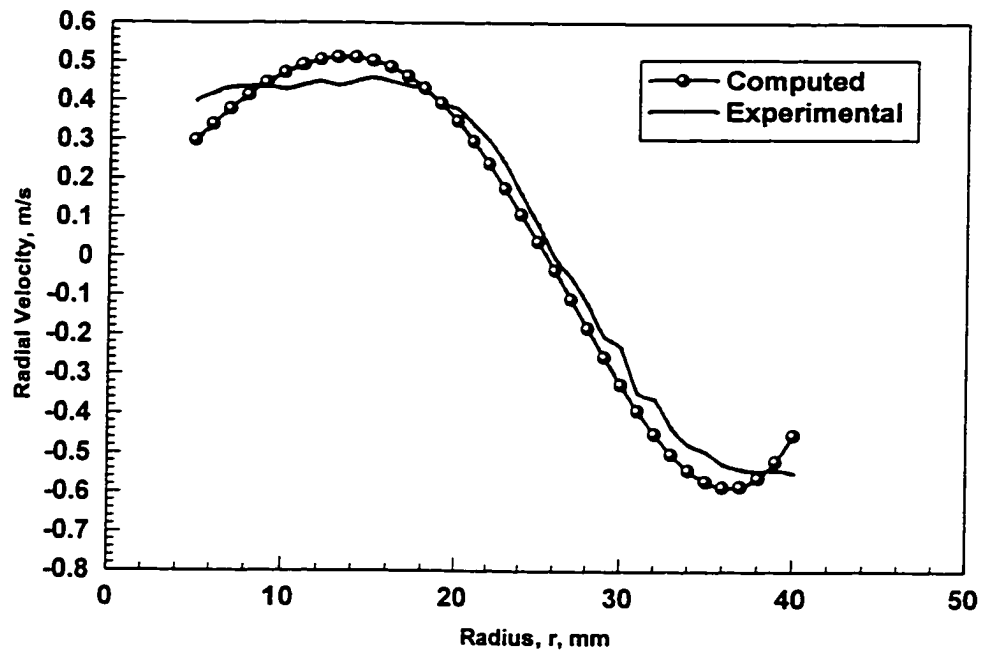


Fig. 5.25: Computed radial velocity profiles compared with the data of Hsieh<sup>17</sup> at  $z = 100\text{mm}$ .

## Chapter 6

### 6.0 CONCLUSIONS

Phenomenological separation in three-phase hydrocyclone is based on physics of the separation phenomena occurring. The theoretical and experimental modelling has given an insight into the operation and performance of the three-phase hydrocyclone. The design for testing this separation device has shown control and measurement of performance parameters to be fully adequate to produce results of good validity. The major conclusions of this study can be summarised as:

1. Feed concentration of the three-phase mixture influences performance. At the lowest Reynolds number (21,200), the pressure drop increases only marginally with both the feed concentration and the flow ratio. At higher Reynolds numbers, the pressure drop increases substantially with both, the feed concentration and the flow ratio.
2. The Reynolds number based on the intake flow rate data ranged from 21,000 to 98,000 providing part of the input data for computation of velocity spectra.
3. Within a Reynolds number range - 21,200-98,000; As the feed concentration of the three-phase mixture increases oil efficiency drops levelling from inlet Reynolds number ranging from 68,000 - 98,000. On the other hand, the sand efficiency increases slightly but plateuing in the Reynolds number range 41,000-67,000.
4. Flow visualization indicated that was incoherent thickening of the oil core and particle boundary layer thickening. At a concentration of 22% by weight the sand particles plugged the transverse aperture and thus interfering with the vortex stability. Vortex stability realized amplitudes that never reached the diameter of the overflow.
5. Separation tests with feed concentrations up to 2% by weight yielded a maximum efficiency of 89% for a 41- $\mu\text{m}$  oil droplet and 62% for a 46- $\mu\text{m}$  sand particle at

flow split ratio range,  $\Lambda = 2.5 - 4.0$ . For the same range, an increase in feed concentration to 22% realized a maximum efficiency of 65% for a 49- $\mu\text{m}$  oil droplet and 78% for 49- $\mu\text{m}$  sand particle. Theoretical and experimental separation efficiency results were in good agreement.

6. It was found that droplet/particle size influences three-phase separation efficiency. The bigger the droplets/particles the better the efficiency and vice versa. Droplets/particles above about 50-60 $\mu\text{m}$  were easily removed from mixtures with crude which shows the critical dependence of separation on oil drop and sand particle.
7. Statistical analysis using UnifitII shows that the droplets and particles were described by lognormal and gamma distributions for both influent and effluent droplets and particles.
8. Liquid-phase velocity profiles were predicted from the Navier-Stokes equations with a modified Prandtl mixing length model. They were found to compare well with other researchers Hsieh and Dabir.
9. The computed tangential velocity profiles behaved asymptotically as they approached the hydrocyclone wall yielding steep velocity gradients in that region and thus maximum effective viscosity. The computed and experimental velocity spectra results were in concordance.
10. A unique aspect during validation of the results was that the computed and experimental tangential velocity profiles compared well better than the axial velocity profiles. This indicated that the influence of viscosity fluctuation on axial velocity distribution was much greater than that on tangential velocity distribution.
11. Correlation between turbulence and Reynolds number was not established for vortical flows but the current study adopted the universal belief that turbulent conditions exist within the body of the hydrocyclone. In addition, the predicted and actual intake Reynolds numbers were of the order of  $10^5$  to  $10^6$  and hence the above closure applied to both turbulent and laminar flows.



## 6.1 RECOMMENDATIONS

The following work is recommended for further research:

1. The non-Newtonian behaviour of concentrated suspension should be examined and included in the model formulation to extend the applicability of the current model.
2. A ring inlet should be used to equalize tangential distribution of the feed slurry.
3. Most of the theoretical modelling were compared with experimental results from other researchers. LDV measurements are required to confirm the velocity profiles computed.
4. High industrial flowrates requires a large scale hydrocyclone or multiple parallel units of three-phase hydrocyclone. For good performance at low values of  $\Delta P$  multiple parallelled three-phase units can be used.
5. Effect of concentration on velocity profiles should explored. The particle interaction at high feed concentration is likely to transform the velocity profiles.

**7. REFERENCES**

1. K. Rietema, Performance and Design of Hydrocyclones, Parts I to IV, Chemical Engineering Science, 15: 298, 1961.
2. L. Svarovsky, Hydrocyclones, Technomic Publishing Co. Inc, New York, p140, 1984.
3. Ibid, p303.
4. R.M.M. Changirwa, Modelling of a Three-Phase Separation Hydrocyclone, M.A.Sc. Thesis, Dept. of Mining and Metallurgical Engineering, TUNS, Halifax, NS, Canada, 1994.
5. M. I. G. Bloor and D. B. Ingham, Theoretical Investigation of the Flow in a Conical Hydrocyclone, Trans. Inst. Chem. Engrs., Vol. 51, p36, 1973.
6. P. Bhattaryya, Theoretical Study Of The Flow Field Inside A Hydrocyclone With Vortex Finder Diameter Greater Than That Of Apex Opening, I. Laminar Case; II. Turbulent Case, Applied Science Research, 36: 197-212; 213-225, 1980.
7. K.R. Upadrashta, V.J. Ketcham and J.D. Miller, Tangential Velocity Profile for Pseudoplastic Power-Law Fluids in the Hydrocyclone - A Theoretical Derivation, International Journal of Mineral Processing, 20, 309-318, 1987.
8. A.J. Lynch, Mineral Crushing and Grinding Circuits, Elsevier, NY, 1976.
9. L.R. Plitt, A Mathematical Model of the Hydrocyclone Classifier, CIM Bulletin, 116, 1976.

10. M. I. G. Bloor and D. B. Ingham, The Flow in Industrial Cyclones, J. Fluid Mech. Vol. 178, p507-519, 1987.
11. D. F. Kelsall, A Study of the Motion of Solid Particles in a Hydraulic Cyclone, Trans. Inst. Chem. Eng. 30, 87, 1952.
12. C.C. Hwang, H.Q. Shen, G. Zhu, and M.M. Khonsari, On the Main Flow Patterns in Hydrocyclones, Journal of Fluids Engineering, vol.115, p21-25, March 1993.
13. Changirwa R.M.M and Rockwell M.C., An Optimization Model for Multiple Hydrocyclones Separation System, Paper WD3.1, Proc. 35th Conf. of the Canadian Operational Research Society (CORS), Halifax, May 25-27, 1993.
14. Changirwa R.M.M. and Rockwell M.C., A Mathematical Model for a Multiple-Cone Hydrocyclone Concurrent Three-Phase (CTP) Separation System, the Petroleum Society of CIM 45th Annual Technical Meeting and AOSTRA Annual Technical Conference, Calgary, Alberta, June 12-15, 1994.
15. M. D. Brayshaw, A Numerical Model of the Inviscid Flow of a Fluid in a Hydrocyclone to Demonstrate the Effect of Changes in the Vorticity Function of the Flow Field on Particle Classification, Int. Journal of Min. Proc., 29: 51-75, 1990.
16. N.Rhodes, K.A. Pericleous and S.N. Drake, The Prediction of Hydrocyclone Performance With a Mathematical Model., 3rd Int. Conference on Hydrocyclones, Oxford, England, 30 September - 2 October, p 51, 1987.
17. Hsieh, K.T., Phenomenological Model Of The Hydrocyclone, Ph.D Thesis, University of Utah, UT, 1988.

18. Hsieh, K.T. and R.K. Rajamani, A mathematical model of the hydrocyclone based on the physics of fluid flow, *AIChEJ.*, 37:5, 735-746, 1991.
19. T.C. Monredon, K.T. Hsieh and R.K. Rajamani, Fluid Flow Model of the Hydrocyclone, an Investigation of Device Dimensions, *Int. J. Min. Proc.*, 35: 65, 1992.
20. D. Bradley and D. J. Pulling, Flow Patterns in the Hydraulic Cyclone and their Interpretation in Terms of Performance, *Trans. Inst. Chem. Eng.* 37: 34, 1959.
21. Dabir B., Mean Velocity Measurements in a 3"-Hydrocyclone using Laser Doppler Anemometry, Ph.D Thesis, Department of Chemical Engineering, Michigan State University, East Lansing, MI, 1983.
22. T. Dyakowski and R. A. Williams, Prediction of High solids Concentration Region Within A Hydrocyclone, *Powder Technology*, 87: 43-47, 1996.
23. A. Malhotra, R. M. R. Branion and E. G. Hauptmann, Modelling the Flow in a Hydrocyclone, *The Can. Journal of Chemical Engineering*, Vol 72, Dec., 1994.
24. R.M.C. So, H.S. Zhang and C.G. Speziale, Near Wall Modelling of the Dissipation Rate Equation, *AIAA J.* 29: 2069-2076, 1991.
25. M. I. G. Bloor and D. B. Ingham, On The Efficiency Of The Industrial Cyclone, *Trans. Inst. Chem. Engrs.*, Vol. 51, 1973.
26. M. I. G. Bloor and D. B. Ingham, Turbulent Spin in A Cyclone, *Trans. Inst. Chem. Engrs.*, Vol. 53, 1975.

27. K.Y. Kim and M.K. Chang, Calculation of a Strongly Swirling Turbulent Round Jet with Recirculation by an Algebraic Stress Model, *Int. J. Heat Fluid Flow*, 9: 62, 1988.
28. D. F. Kelsall, The Theory and Applications of the Hydrocyclones, In Pool and Doyle (eds) *Solid-Liquid Separation*. HMSO, London, 1966.
29. J. G. Van Kooy, The Influence of the Reynolds' Number on the Operation of a Hydrocyclone, In K. Rietema and C. G. Verver (eds), *Cyclones in Industry*, Ch. 5, Elsevier, Amsterdam, 1961.
30. V. G. Renner and H. E. Cohen, Measurement and Interpretation of Size Distribution of Particles Within a Hydrocyclone. *Trans. Inst. Min. and Extr. Met.* 87: C139, 1978.
31. A. Mitzmager and J. Mizrahi, Correlation of the Pressure Drop Through Small Cyclones Operating With Dilute Pulps of Various Liquids, *Trans. Inst Chem. Eng.* 42: T152, 1964.
32. H. Trawinski Theory, Applications and Practical Operation of Hydrocyclones, *Engineering and Mining Journal*, 115 127, September 1976
33. S. Akaike, Collection Efficiency of the Hydrocyclone Without Underflow for the Separation of the Sand, 3rd Int. Conf. on Hydrocyclones, Oxford, England, 30 September - 2 October, p 35, 1987.
34. L. Svarovsky, Selection of Hydrocyclone and Design Using Dimensionless Groups, 3rd Int. Conf., on Hydrocyclones, Oxford, England, 30 Sept. - 2 Oct., p 1, 1987.

35. Gu Fanglu and Li Wenzhen, Measurement and Study of Velocity Field in Various Cyclones by Use of Laser Doppler Anemometry, 3rd Int. Conference on Hydrocyclones, Oxford, England, 30 September - 2 October, p 65, 1987.
36. S.W.Yopps, A Study of the Effect of Slurry Rheology on Hydrocyclone Performance, 3rd Int. Conf. on Hydrocyclones, Oxford, England, 30 Sept.-2 Oct. p 59, 1987.
37. S. Akaike, p 37, 1987.
38. J.W.J. Ferguson, Theoretical Aspects of a pulp Suspension Flowing in a Conventional Hydrocyclone, Tappi J., 71, 125, 1988.
39. K. Heiskanen and A. Vesanto, A High Performance Hydrocyclone Design - the twin vortex cyclone, 3rd Int. Conference on Hydrocyclones, Oxford, England, 30 September - 2 October, p 263, 1987.
40. J.R. Davidson et al., The Improvement of Cyclone Performance with a Special Spigot Design, 3rd Int. Conference on Hydrocyclones, Oxford, England, 30 September - 2 October, p 259, 1987.
41. G.A. Young, An Experimental Investigation of the Dimensional and Operating Parameters of a Hydrocyclone in a Drilling Mud, 3rd Int. Conference on Hydrocyclones, Oxford, England, 30 September - 2 October, p 221, 1987.
42. A.A. Turak, A Generalised Model for Classifying and Automedium Cyclones, 3rd Int. Conference on Hydrocyclones, Oxford, England, 30 September - 2 October, p 43, 1987.

43. R.D. Stoessner and E.A. Zawadzki, Selection of Dense Medium Cyclones for Low Gravity Fine Coal Cleaning, 3rd Int. Conference on Hydrocyclones, Oxford, England, 30 September - 2 October, p 111, 1987.
44. P.S. Jones, A Field Comparison of Static and Dynamic Hydrocyclones, SPE Production & Facilities, May 1993.
45. M.I.G. Bloor, On Axially Symmetric Flow Models for Hydrocyclone, 3rd Int. Conference on Hydrocyclones, Oxford, England, 30 September - 2 October, p 83, 1987.
46. D. F. Kelsall, A Further Study of the Hydraulic Cyclone, Chem. Eng. Sci., 2, 254, 1953.
47. S. R. Knowles, D. R. Woods and I. A. Feverstein, The Velocity Distribution Within a Hydrocyclone Operating Without an Air Core, Can. J. Chem. Eng. 51: 263, 1973.
48. Bradley, p123, 1965.
49. L. Svarovsky and B. S. Marasinghe, Performance of Hydrocyclones at High Feed Solids Concentrations, In Proc. Int. Conference on Hydrocyclones, Cambridge Paper 10: 127-142, 1980.
50. Sheng, H.P., Welkera, J.R. and Sliepcevich, C.M., Liquid-Liquid Separations in a Convectional Hydrocyclone, Canadian J. Chem. Eng. Vol. 52, August, 1974.
51. Bohnet, M., Separation of Two Liquids in the Hydrocyclones, Chem.Eng. Techn. 41., No. 5 & 6, 1969.

52. Tepe J.B and W.K. Woods, Design of Ether-Water Contacting System, United States Energy Commission, AECD-2864, 1943.
53. Hitchon J.W., Cyclones as Liquid-Liquid Contactor-Separators, AERE-CE/r 2777, 1959.
54. Simkin D.J and R.B. Olney, Phase Separation and Mass Transfer in a Liquid-Liquid Cyclone, AICHEJ,2, p 545, 1956.
55. Regehr H.U., The Use of the Hydrocyclone for Separation, Forsch, Ing. Wes. 28, 11-27, 1962.
56. Kimber, G.R. and Thew, M.T. Experiments on Oil/Water Separation With Hydrocyclone, Paper EI, Proc. 1st European Conf. on Mixing and Centrifugal Separation, Cambridge, Organised by BHRA, Pub. BHRA, Cranfield, 1975.
57. Colman D.A., The Hydrocyclone for Separating Light Dispersions, Ph.D. Dissertation, Dept. of Mechanical Eng., Southampton University, UK, 1981.
58. Meldrum N., Hydrocyclones, A Solution to Produced Water Treatment, Proc. 19th Annual Offshore Technology Conf., OTC5594, Houston, April 27-30, 1987.
59. K.N. Nezhati and M.T. Thew, Aspects of the Performance and Scaling of Hydrocyclones for Use with Light Dispersions, 3rd Int. Conference on Hydrocyclones, Oxford, England, 30 September - 2 October, p 167, 1987.
60. A. M. Gerrard and C. J. Liddle, The Optimal Selection of Multiple Hydrocyclone Systems, The Chemical Engineer, 295, May 1975



61. M.G. Dressen, Trans. Am. Inst. Min. (Metall.) Eng., p177, 1948.
62. L. Svarovsky and J.K. Potter, Counter-current Washing With Hydrocyclones, 3rd Int. Conference on Hydrocyclones, Oxford, England, 30 September - 2 October, p 235, 1987.
63. A. M. Gerrard and C. J. Liddle, How to Get the Most out of Your Hydrocyclone Systems. Process Eng. 105, June 1976
64. Colman, D.A. and Thew, M.T. Hydrocyclone to Give a Highly Concentrated Sample of a Lighter Dispersed Phase, Submitted to BHRA Hydrocyclone Conference Cambridge, October, 1980.
65. L.R. Plitt, Roping in Hydrocyclones, 3rd Int. Conference on Hydrocyclones, Oxford, England, 30 September - 2 October, p 21, 1987.
66. Bednarski S., Criteria of Granular Separation in a Hydrocyclone, Proc. 1st. European Conf. on Mixing and Centrifugal Separation, Cambridge, Sept. 1974.
67. J. R. Nebrensky, G. E. Morgan and B. J. Oswald, Cyclones for Gas/oil Separation, In Int. Conf. on Hydrocyclones, Paper 12: 167-178. BHRA, Cranfield, 1980.
68. Colman D.A.,and Thew M.T., Correlation of Separation Results From Light Dispersion Hydrocyclones, Chem. Eng. Res. Des., 61, July 1983, p. 233.
69. D. A. Colman, M. T. Thew and D. R. Corney, Hydrocyclones for Oil-water separation. In Int. Conf. on Hydrocyclones, Paper 11: 143-166. BHRA, Cranfield, 1980.

70. R.K. Duggins and P.C.W. Frith, Turbulence Effects in Hydrocyclones, 3rd Int. Conf. on Hydrocyclones, Oxford, England, 30 Sept. - 2 Oct., p 75, 1987.
  71. R.R. Horsley and D.W. Allen, The Effect of Yield Stress on Hydrocyclone Performance in the Mining Industry, 3rd Int. Conference on Hydrocyclones, Oxford, England, 30 September - 2 October, p 269, 1987.
  72. B.D. Rouse, Confirmation of Modelling Techniques for Small Diameter Cyclones, 3rd Int. Con. on Hydrocyclones, Oxford, England, 30 Sept. - 2 Oct., p7, 1987.
  73. I.C. Symth and M.T. Thew, A Comparison of the Separation of Heavy Particles and Droplets in a Hydrocyclone, 3rd Int. Conference on Hydrocyclones, Oxford, England, 30 September - 2 October, p 193, 1987.
  74. L. Svarovsky (ed.), Solid-Liquid Separation, 2nd edn. Butterworths, London, 1981.
  75. A. M. Gerrard and C. J. Liddle, Numerical Optimization of Multiple Hydrocyclone Systems, *The Chemical Engineer*, 107, February 1978.
  76. Hashmi, K.A., Hamza, H.A., Kar, K.L., Zalischuk, J.L. and Thew, M.T., Liquid-Liquid Hydrocyclone for Removing Oil from Produced Waters in Heavy Oil Recovery, Joint Technical Seminar, Arctic and Marine Oilspill Program (AMOP) and Chemical Spills, June 9, 1992.
  77. Bednarski S. and Listewnik J., Hydrocyclones for Simultaneous Removal of Oil and Solid Particles from Ship's Oil Waters, Int. Conf. on Hydrocyclones, Paper G2 181-185, Oxford, England, 1987.
-

78. R.M.M. Changirwa and M.C. Rockwell, Hybrid Simulation of Hydrocyclone Separation for Oil-Solids-Water, 3rd Canadian Conference on Computer Applications in the Mineral Industry, Montreal, Quebec, October 22-25, 1995.
79. R.M.M. Changirwa and M.C. Rockwell, An Experimental Investigation of a Three-Phase Separation Hydrocyclone, CIM '95 Conf., Halifax, NS, May 1995.
80. C.R. Wylie and L.C. Barret, Advanced Engineering Mathematics, M<sup>c</sup>Graw Hill, 5th Edition, p194, 1982.
81. K.A. Pericleous, Mathematical Simulation of Hydrocyclones, App. Math. Modelling, Vol. 11, p242, 1987.
82. J.F. Richardson and W.N. Zaki, The Sedimentation Of A Suspension Of Uniform Spheres Under Conditions Of Viscous Flow, Chem. Eng. Sci., Vol. 3, p65, 1954.
83. L.Davies, D. Dollimore and G.B. Mcbridge, Sedimentation Of Suspensions, Simple Methods Of Calculating Sedimentation Parameters, Powder Technology, Vol. 16, p45, 1977.
84. E.Barnea and J.Mizrahi, A Generalized Approach to the Fluid Dynamics of Particulate Systems; Part I, Chemical Eng. J. Vol. 5, p171, 1973.
85. G.K. Batchelor, An Introduction To Fluid Dynamics, Cambridge University Press, Cambridge, 615pp, 1973.
86. M. Rahman, Water Waves, Oxford University Press Inc, New York, p105, 1994.
87. K.A. Pericleous, N.Rhodes and G.W. Cutting, A Mathematical Model for

Predicting the flow Field in a Hydrocyclone Classifier, 2nd Int. Conference on Hydrocyclones, Bath, England, Paper B1, 1984.

88. P.J. Roache, Computational Fluid Dynamics, Hermosa, Albuquerque, New Mexico, 1972.
89. E.O. Lilge, Hydrocyclone Fundamentals, Trans. Instn. Min. Metall., 71, 285, 1962.
90. Law A.M. and Kelton W.D., Simulation Modelling and Analysis, McGraw-Hill, p232, 1991.
91. Law A.M. and Vincent S.G., UniFitII Software, 1993.
92. L. Svarovsky, Solid-Liquid Separation, Technomic Publishing Co. Inc, New York, p140, 1984.
93. L. Rosenhead, Laminar Boundary Layers, Oxford University Press, p128, 1963.
94. R. Arcs, Vectors, Tensors and the Basic Fluid Mechanics, Prentice-Hall Inc., Englewood Cliffs, NJ., p170, 1962.

**APPENDIX A**

**COMPUTED AND EXPERIMENTAL DATA ON THE DISKETTE INSIDE COVER**

**DATA (IN WORDPERFECT 6.1 FORMAT) CONTAINS SEPARATION TESTS,  
COMPUTED VELOCITY SPECTRA AND FLUID FLOW VISUALIZATION TESTS**

## APPENDIX B

## FORTRAN 77 PROGRAM FOR PERFORMANCE PARAMETERS

```

C*****
C PROGRAM TO SOLVE A SET OF HYDROCYCLONE PERFORMANCE PARAMETERS IN
C FORM OF LINEAR SYSTEMS OF EQUATIONS USING GAUSSIAN ELIMINATION.
C VARIABLES USED ARE:
C   LIMIT : PARAMETER GIVING MAXIMUM DIMENSION OF MATRIX
C   LIMAUG: PARAMETER (LIMIT +1) FOR MAXIMUM # COLUMNS IN AUG
C   N      : NUMBER OF EQUATIONS AND UNKNOWNNS
C   AUG    : AUGMENTED MATRIX FOR THE LINEAR SYSTEM
C   X      : SOLUTION VECTOR
C   I,J,K  : INDICES
C   MULT   : MULTIPLIER USED TO ELIMINATE AN UNKNOWN
C   PIVOT  : USED TO FIND NONZERO DIAGONAL ENTRY
C*****

C   SUBROUTINE GAUSS
      INTEGER LIMIT, LIMAUG
      PARAMETER (LIMIT = 10, LIMAUG =LIMIT +1)
      DOUBLE PRECISION AUG(LIMIT, LIMAUG), X(LIMIT),MULT
      INTEGER I,J,K,PIVOT

C READ NUMBER OF EQUATIONS, COEFFICIENT MATRIX AND CONSTANT VECTOR
C FROM A FILE

      OPEN(UNIT=15, FILE='HGF.DAT',STATUS = 'OLD')
      OPEN(UNIT=16, FILE='HGF.OUT',STATUS = 'UNKNOWN')
      WRITE(*,201) 'I','INFLOW','OFLOW','TFLOW'
      WRITE(16,201) 'I','INFLOW','OFLOW','TFLOW'
201  FORMAT(' ',A3,6X,A6,3X,A6,4X,A6)

```

```

DO 300 I1=1, 25

READ(15,*) N, ((AUG(I,J),J=1,N),I=1,N), (AUG(I,N+1),I=1,N)

C GAUSSIAN ELIMINATION

DO 170 I=1,N

C LOCATE NONZERO DIAGONAL ENTRY

IF (AUG(I,I).EQ.0) THEN
PIVOT = 0
J=I+1
130 IF ((PIVOT.EQ.0) .AND. (J.LE.N)) THEN
IF (AUG(J,I).NE.0) PIVOT=J
J=J+1
GO TO 130
END IF
IF (PIVOT.EQ.0) THEN
STOP 'MATRIX IS SINGULAR'
ELSE

C INTERCHANGE ROWS I AND PIVOT

DO 140 J =1, N+1
TEMP = AUG(I,J)
AUG(I,J) = AUG(PIVOT,J)
AUG(PIVOT,J) = TEMP
140 CONTINUE
END IF
END IF

C ELIMINATE ITH UNKNOWN FROM EQUATIONS I+1,..., N

```

```

        DO 160 J=I+1,N
MULT = -AUG(J,I)/AUG(I,I)
        DO 150 K=I,N+1
          AUG(J,K)=AUG(J,K) + MULT*AUG(I,K)

150      CONTINUE
160      CONTINUE
170      CONTINUE

C FIND THE SOLUTIONS

      X(N)=AUG(N,N+1)/AUG(N,N)
        DO 190 J = N-1, 1, -1
          X(J)=AUG(J,N+1)
            DO 180 K = J+1,N
              X(J)=X(J)-AUG(J,K)*X(K)
180          CONTINUE
          X(J)=X(J)/AUG(J,J)
190        CONTINUE
C        PRINT*
C        PRINT*,'SOLUTION VECTOR IS'
C        DO 210 I=1,N
C          PRINT 200,I,X(I)
          WRITE (*,203) I1,((X(I)),I=1,3)
          WRITE (16,203) I1,((X(I)),I=1,3)
203        FORMAT (' ',1X,I2,3X,3(F8.3,2X))
C 200        FORMAT(1X,'X(',I2,')=',F6.3)
C210        CONTINUE
300        CONTINUE

      END

```



**Table B1: Input Data For Computer Program HGF.FOR**

N	Dispersed Phase Fractions									Feed Fractions		
3	1	1	1	0.8	0.6	0.7	0.45	0.42	0.53	1	0.68	0.34
3	1	1	1	0.78	0.56	0.57	0.45	0.62	0.53	1	0.78	0.38
3	1	1	1	0.48	0.16	0.27	0.45	0.52	0.35	1	0.88	0.23
3	1	1	1	0.58	0.46	0.51	0.43	0.64	0.59	1	0.69	0.51
3	1	1	1	0.41	0.6	0.57	0.48	0.62	0.75	1	0.56	0.43
3	1	1	1	0.38	0.56	0.45	0.38	0.61	0.53	1	0.47	0.39
3	1	1	1	0.29	0.16	0.27	0.35	0.52	0.35	1	0.38	0.27
3	1	1	1	0.19	0.34	0.31	0.43	0.61	0.59	1	0.39	0.21
3	1	1	1	0.78	0.6	0.77	0.65	0.52	0.53	1	0.69	0.38
3	1	1	1	0.78	0.56	0.57	0.45	0.62	0.53	1	0.78	0.38
3	1	1	1	0.49	0.18	0.28	0.47	0.57	0.36	1	0.98	0.43
3	1	1	1	0.59	0.49	0.51	0.45	0.64	0.57	1	0.59	0.50
3	1	1	1	0.43	0.6	0.59	0.48	0.64	0.76	1	0.58	0.41
3	1	1	1	0.28	0.66	0.47	0.38	0.61	0.54	1	0.48	0.42
3	1	1	1	0.81	0.6	0.7	0.55	0.52	0.43	1	0.48	0.36
3	1	1	1	0.38	0.36	0.37	0.35	0.72	0.63	1	0.78	0.58
3	1	1	1	0.28	0.26	0.37	0.45	0.42	0.55	1	0.68	0.13
3	1	1	1	0.58	0.56	0.61	0.33	0.64	0.39	1	0.29	0.21
3	1	1	1	0.71	0.8	0.77	0.58	0.67	0.78	1	0.76	0.63
3	1	1	1	0.88	0.86	0.75	0.88	0.81	0.73	1	0.77	0.89
3	1	1	1	0.9	0.7	0.8	0.65	0.52	0.58	1	0.78	0.74
3	1	1	1	0.9	0.36	0.67	0.35	0.42	0.73	1	0.68	0.58
3	1	1	1	0.23	0.26	0.37	0.55	0.42	0.35	1	0.58	0.33
3	1	1	1	0.68	0.26	0.31	0.43	0.44	0.52	1	0.65	0.54
3	1	1	1	0.71	0.8	0.67	0.58	0.62	0.85	1	0.76	0.43

**OUTPUT DATA****Table B2: Output Data from Computer Program HGF.FOR**

<b>I</b>	<b>INFLOW</b>	<b>OFLOW</b>	<b>TFLOW</b>
1	0.884	1.084	0.968
2	0.961	0.812	0.851
3	1.938	1.846	0.908
4	1.111	5.156	7.267
5	0.377	1.678	1.055
6	1.560	1.174	1.734
7	2.912	0.471	1.441
8	5.417	24.333	-28.750
9	1.217	0.399	1.818
10	0.961	0.812	0.851
11	2.795	1.131	0.664
12	1.313	1.250	1.562
13	0.214	2.418	1.632
14	1.374	1.427	1.801
15	1.224	0.854	1.370
16	-19.158	-60.158	80.316
17	-123.571	98.286	26.286
18	8.476	1.314	8.790
19	0.444	0.556	0.000
20	2.623	2.918	1.295
21	17.200	17.400	33.600
22	0.262	0.162	0.575
23	1.025	3.213	3.189
24	0.768	1.114	1.346
25	1.309	0.290	0.598

## APPENDIX C

### DETERMINATION OF OIL AND SAND CONCENTRATIONS

The concentrations of the dispersed phases in the feed, trans-flow and underflow streams were determined gravimetrically using a filtration technique. To separate the crude oil and quartz sand from the sample fluid, Whatman #42 filters (passing  $2.5 \mu\text{m}$  particles and below) were used in a multiple funnel-beaker arrangement (see Fig. C1). Three ten-funnel-beaker arrays were used to facilitate concurrent analysis.

#### Procedure:

Weigh the sample and divide into ten parts.

Weigh and fold ten filter papers into cones.

Place them with the cone apex to funnel-beaker arrays.

Add the sub-divided samples to the filters and air dry the filters and residue.

Transfer the dried filters and samples to a fume chamber and add chloroform.

Dry the filters and residue and weigh them. Each stream sampled had each rack it enabled concurrent analysis.

#### Reporting Results:

1. Weight of sample (crude oil + sand + water) = \_\_\_gm
2. Weight of filters = \_\_\_gm
3. Weight of filters and dry residue (crude + sand) = \_\_\_gm
4. Weight of filters and dry residue treated with chloroform (sand) = \_\_\_gm
5. Weight of sand = (4) - (2) gm
6. Weight of crude oil = (3) - (4) gm

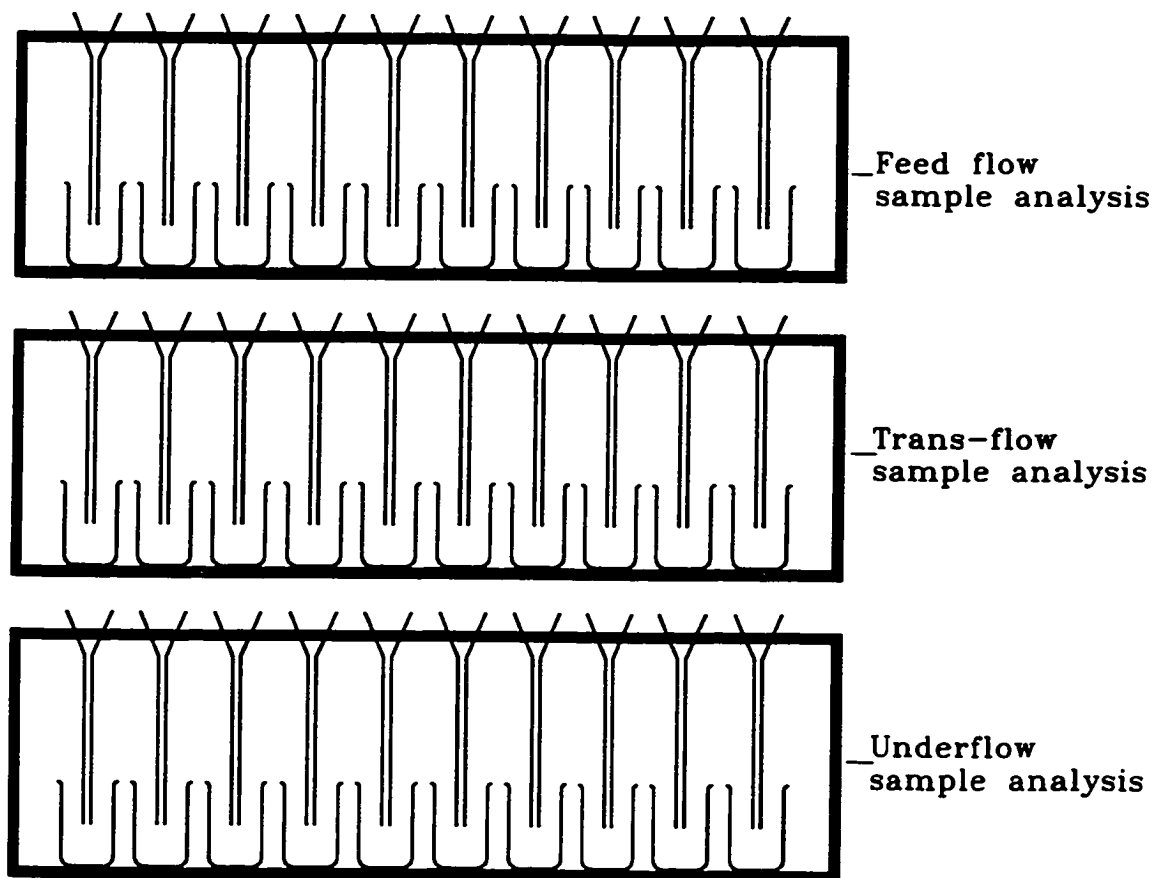


Fig. C1: Concurrent Gravimetric Sample Analysis of the Three-Phase Hydrocyclone Feed and Products.

Thus, the concentration of crude oil is given by;

$$\text{Oil Conc.} = \left\{ \frac{(4) - (3)}{(1)} \times 10^6 \right\} \text{ppm} \dots\dots\dots (C1)$$

The concentration of sand is given by;

$$\text{Sand Conc.} = \left\{ \frac{(3) - (2)}{(1)} \times 10^6 \right\} \text{ppm} \dots\dots\dots (C2)$$

## APPENDIX D

### DROPLET/PARTICLE SIZE DETERMINATION

Droplet/particle analysis was performed by a Malvern droplet/particle coupled to a PC. The quartz sand analysis was using the regular LASER cell but required oil droplet size analysis required a special cell. Therefore, a 50 by 25 by 75mm top-open rectangular glass cell (see Fig. D1) was constructed from 75 by 50mm metallurgical glass slides. Two parallel sides 25mm maintained to prevent the Laser beam distortion. The cell was filled with the sample to be tested and placed in between the LASER torch and the receiver. A sketch arrangement is given in Fig 4.8.

The rectangular cell was calibrated using a sample with a known size distribution (solids used) in the regular cell and also in the designed cell. They all followed a Lognormal distribution. Feed samples of 500mls were divided into 10 samples for measurements. 20mls of the overflow was also measured. The subdivided quartz sand and crude oil samples were placed in the rectangular cell. A small magnetic stirrer bar, in the cell, was used to stir the sample to expel air and to assist keep droplets and particles in buoyancy for LASER radiation scanning.

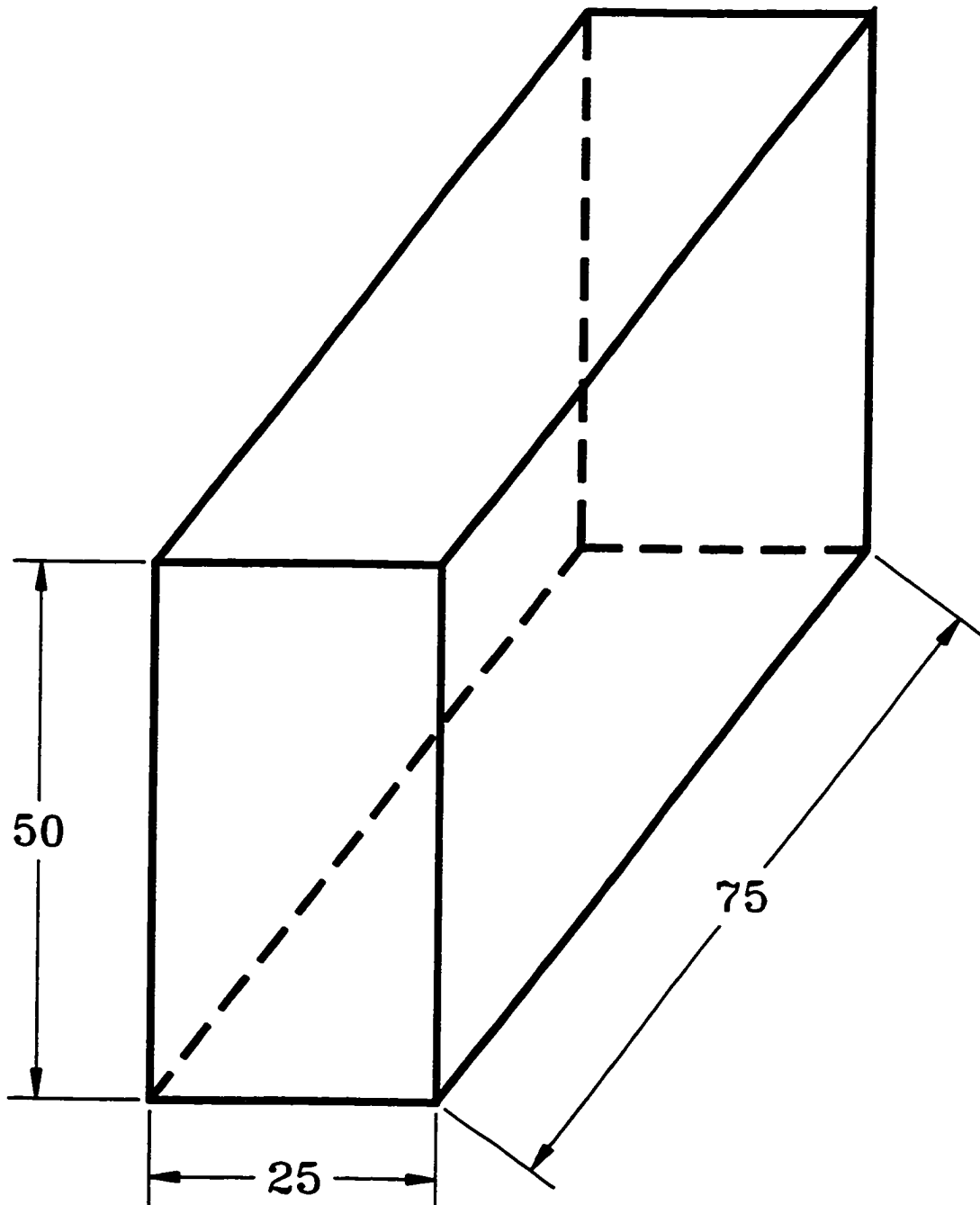


Fig. D1: A Rectangular Sample Cell for Laser Droplet/Particle Sizer (Glass thickness is 1.5mm. All dimensions are in millimetres).

## APPENDIX E

### STATISTICAL ANALYSIS OF OIL DROPLET AND SAND PARTICLES

In order to analyze droplet/particle sizes, statistical analysis was performed. Goodness-of-Fit Tests were done to fit distributions to oil droplets and sand particles. A goodness-of-fit test is a statistical hypothesis test (see Law and Kelton<sup>86</sup>) that is used to assess formally whether given data are an independent sample from a particular fitted distribution. That is, a goodness-of-fit test can be used to test the null hypothesis that your data are an independent sample from a fitted distribution. There are three different goodness-of-fit tests for testing a null hypothesis, namely, the chi-square test, the Kolmogorov-Smirnov test, and the Anderson-Darling test. For a test of level  $\alpha$ , each of these tests has the following form:

If  $T$  is greater than  $t(\alpha)$ , reject the null hypothesis otherwise, do not reject the null hypothesis, where  $T$  is a statistic computed from your data and  $t(\alpha)$  is a critical value (which depends on  $\alpha$ , the sample size  $n$ , and the test itself) that is chosen so that the probability that  $T$  is greater than  $t(\alpha)$  is equal to  $\alpha$  when the null hypothesis is true. For each of the tests, the statistic  $T$  is some measure of the "distance" between the fitted distribution and a sample distribution computed from your data. Typically, an analyst chooses the level  $\alpha$  to be 0.05 or 0.1.

When one performs a hypothesis test, two types of errors can be made. If one rejects the null hypothesis when in fact it is true, this is called a Type I error. The probability of a Type I error is equal to the level  $\alpha$  and is thus under your control. If one "accepts" the null hypothesis when it is false, this is called a Type II error. For a fixed level  $\alpha$  and sample size  $n$ , the probability of Type II error, which can be denoted by  $\beta$ , depends on what distribution is actually true (as compared to the hypothesized distribution), and may be unknown.  $1 - \beta$  is called the power of a test, and it is equal to the probability of rejecting the null hypothesis when it is false. Clearly, a test with high power is required.

Here follows some general properties of goodness-of-fit tests. First, failure to reject the null hypothesis should not be interpreted as "accepting the null hypothesis as being true." These tests are often not very powerful for small to moderate sample sizes  $n$ ; that is, they are not very sensitive to subtle disagreements between the data and the fitted distribution. Instead, they should be regarded as a systematic approach for detecting fairly gross differences. On the other hand, if  $n$  is very large, then these tests will almost always reject the null hypothesis. Since the null hypothesis is virtually never exactly true, even a minute departure from the hypothesized distribution will be detected for large  $n$ . This is an unfortunate property of these tests, since it is usually sufficient to have a distribution that is "nearly" correct.

The following is a brief discussion of the three goodness-of-fit tests.

### **Chi-Square Test**

The chi-square test is applicable to both continuous and discrete distributions, as long as the parameters of the fitted distribution are estimated by the method of maximum likelihood. It can be performed with equal-probable or equal-width intervals, with the former approach being recommended. There is no definite prescription for choosing the test intervals, which is a major drawback of the test. In some situations entirely different conclusions can be reached from the same data set depending on how the intervals are specified.

### **Kolmogorov-Smirnov Test**

The Kolmogorov-Smirnov test is only applicable to certain continuous distributions, namely, exponential, normal, lognormal, Weibull, extreme value type A, extreme value type B, logistic, and log-logistic. (For the non-negative distributions, the location parameter cannot be estimated from the data.) On the other hand, the Kolmogorov-Smirnov test does not have the troublesome interval specification of the chi-square test, and is often more powerful.



**Anderson-Darling Test**

The Anderson-Darling test is applicable to the same continuous distributions as the Kolmogorov-Smirnov test, as well as the gamma and Pearson type 5 distributions. (For the non-negative distributions, the location parameter cannot be estimated from the data). It is also often more powerful.

## APPENDIX F

### ISO-KINETIC SAMPLER

In order to determine the concentrations of the dispersed phases in the feed and underflow by gravimetric method such as filtering, small samples were needed for analysis. The large volumetric flowrates of the feed and underflow streams (about 4.5m<sup>3</sup>/hr) prevented the total diversion of each stream for sampling. Thus, two iso-kinetic sampling probes were used to take representative samples from these streams.

According to Svarovsky<sup>88</sup> sampling should be governed by the following rules:

1. Sampling should be done from a moving stream.
2. A sample of the whole of the stream should be taken for many short periods rather, part of the stream for the whole of time.

Applying Bernoulli Principle at points 1 and 2;

$$P_1 + \frac{1}{2}\rho_w u_1^2 = P_2 + \frac{1}{2}\rho_w u_2^2 \quad (F1)$$

At iso-kinetic conditions,  $u_1 = u_2$ , thus  $P_1 = P_2$ . Therefore, the streams should be sampled when the manometer levels are the same.

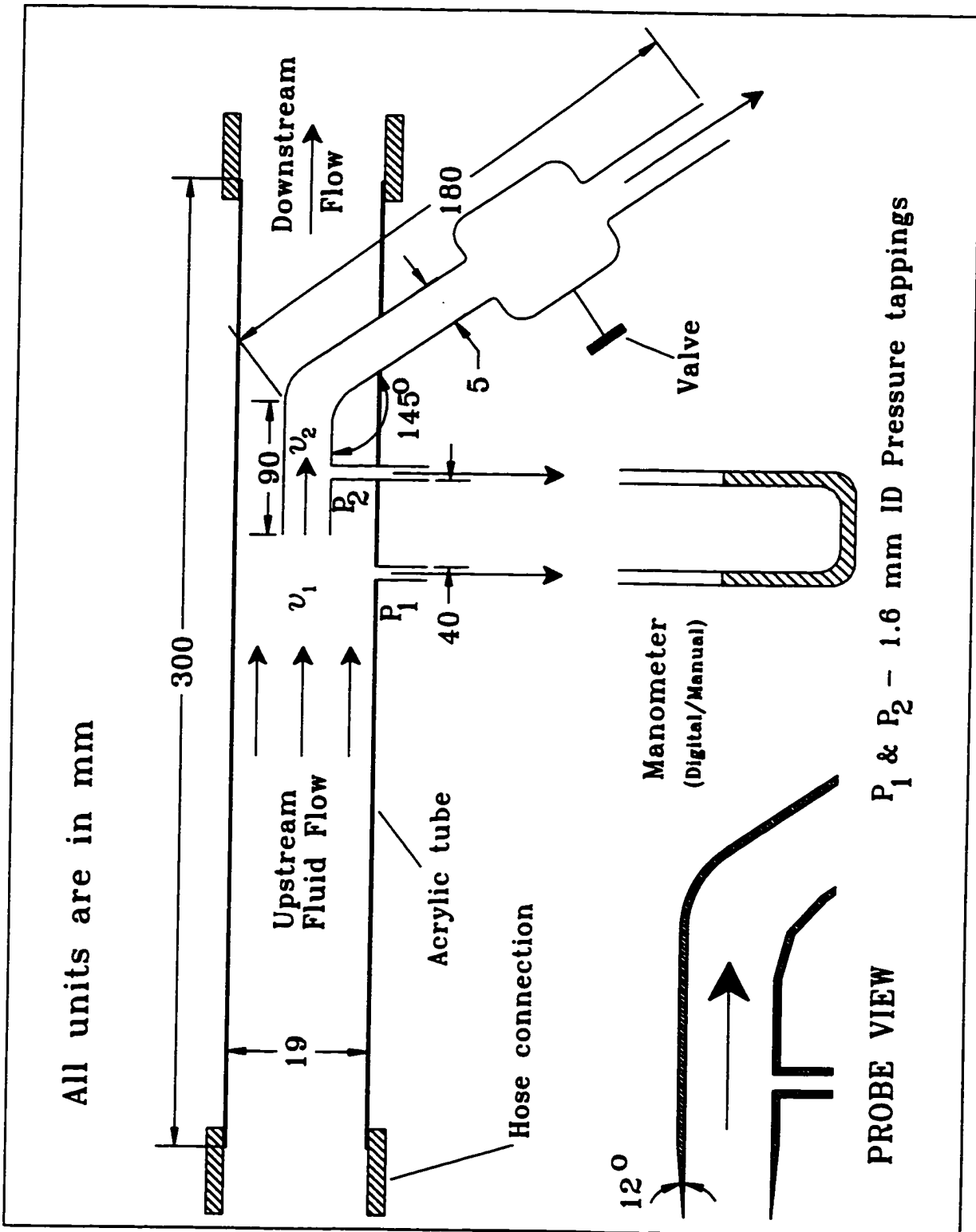


Fig. F1: Iso-kinetic Sampler.

Table F1: Calibration of Iso-kinetic Samplers (all values are in ppm by weight).

Record	Feed Concentration		Underflow Concentration	
	Oil	Sand	Oil	Sand
1	841	874	852	978
2	866	970	826	897
3	881	810	914	904
4	761	890	816	861
5	750	843	902	788
6	850	889	906	806
7	940	928	749	901
<b>Mean</b>	<b>840</b>	<b>886</b>	<b>852</b>	<b>876</b>

Comparing the concentrations in the feed and underflow (see Table F1) the oil and sand concentrations have deviations of 12 and 10ppm respectively.

## APPENDIX G

### GENERAL ORTHOGONAL COORDINATES ( $x_1, x_2, x_3$ )

The following general orthogonal coordinates<sup>93,94</sup> were employed in the current study.

1.

$$\mathit{div} \mathbf{a} = \frac{1}{h_1 h_2 h_3} \left\{ \frac{\partial}{\partial x_1} (h_2 h_3 a_1) + \frac{\partial}{\partial x_2} (h_1 h_3 a_2) + \frac{\partial}{\partial x_3} (h_1 h_2 a_3) \right\} \quad (\text{G1})$$

In cylindrical coordinates: ( $r, \theta, z$ ) matrix elements:  $h_1 = 1, h_2 = r, h_3 = 1, \mathbf{a} = (a_1, a_2, a_3)$

$$\mathit{div} \mathbf{a} = \frac{1}{r} \left\{ \frac{\partial}{\partial r} (r a_1) + \frac{\partial}{\partial \theta} (a_2) + \frac{\partial}{\partial z} (r a_3) \right\} \quad (\text{G2a})$$

$$= \frac{1}{r} \frac{\partial (r a_1)}{\partial r} + \frac{1}{r} \frac{\partial a_2}{\partial \theta} + \frac{\partial a_3}{\partial z} \quad (\text{G2b})$$

2.  $\mathbf{b} = \text{curl } \mathbf{a}$       $\mathbf{b} = (b_1, b_2, b_3)$

$$b_1 = \frac{1}{h_2 h_3} \left\{ \frac{\partial}{\partial x_2} (h_3 a_3) - \frac{\partial}{\partial x_3} (h_2 a_2) \right\} \quad (\text{G3})$$

$$b_2 = \frac{1}{h_1 h_3} \left\{ \frac{\partial}{\partial x_3} (h_1 a_1) - \frac{\partial}{\partial x_1} (h_3 a_3) \right\} \quad (\text{G4})$$

In cylindrical coordinates:

$$b_3 = \frac{1}{h_1 h_2} \left\{ \frac{\partial}{\partial x_1} (h_2 a_2) - \frac{\partial}{\partial x_2} (h_1 a_1) \right\} \quad (\text{G5})$$

$$b_1 = \frac{1}{r} \left\{ \frac{\partial(a_3)}{\partial \theta} - \frac{\partial(r a_2)}{\partial z} \right\} = \frac{1}{r} \frac{\partial a_3}{\partial \theta} - \frac{\partial a_2}{\partial z} \quad (\text{G6})$$

$$b_2 = \frac{\partial(a_1)}{\partial z} - \frac{\partial(a_3)}{\partial r} = \frac{\partial a_1}{\partial z} - \frac{\partial a_3}{\partial r} \quad (\text{G7})$$

$$b_3 = \frac{1}{r} \left\{ \frac{\partial(r a_2)}{\partial r} - \frac{\partial(a_1)}{\partial \theta} \right\} = \frac{1}{r} \frac{\partial(r a_2)}{\partial r} - \frac{1}{r} \frac{\partial a_1}{\partial \theta} \quad (\text{G8})$$

3.

$$\text{grad} \phi = \left\{ \frac{1}{h_1} \frac{\partial \phi}{\partial x_1}, \frac{1}{h_2} \frac{\partial \phi}{\partial x_2}, \frac{1}{h_3} \frac{\partial \phi}{\partial x_3} \right\} \quad (\text{G9})$$

In cylindrical coordinates:

$$\mathit{grad}\phi = \left\{ \frac{\partial\phi}{\partial r}, \frac{1}{r} \frac{\partial\phi}{\partial x_2}, \frac{\partial\phi}{\partial z} \right\} \quad (\text{G10})$$

4.

The Laplacian  $\nabla^2$  in general orthogonal coordinates:

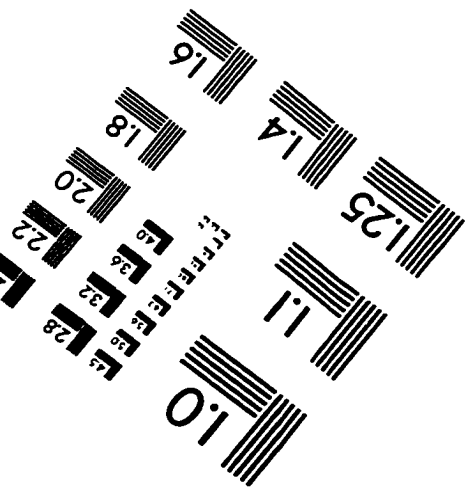
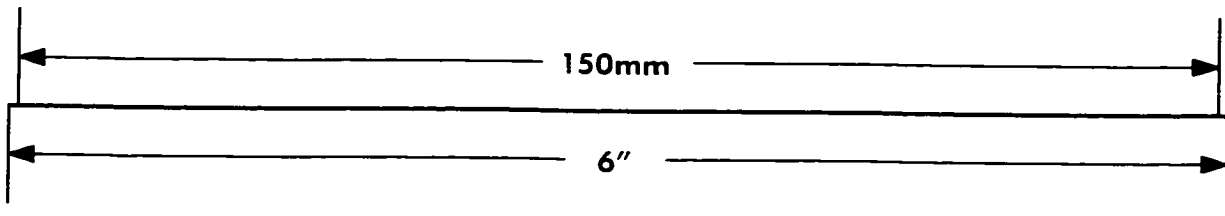
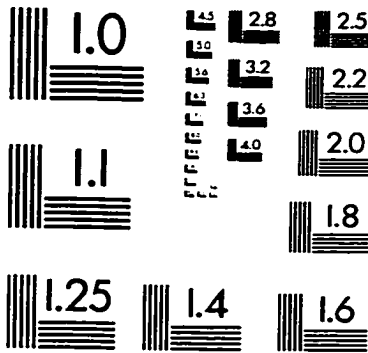
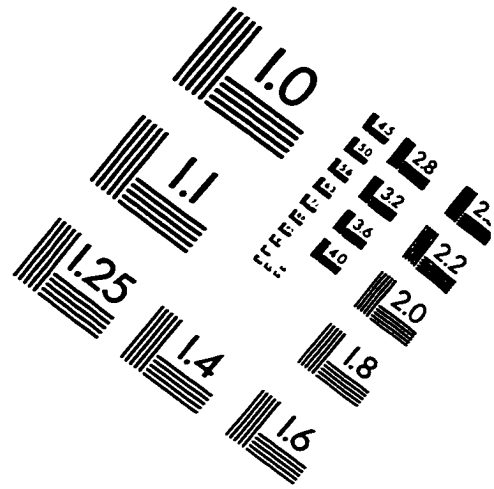
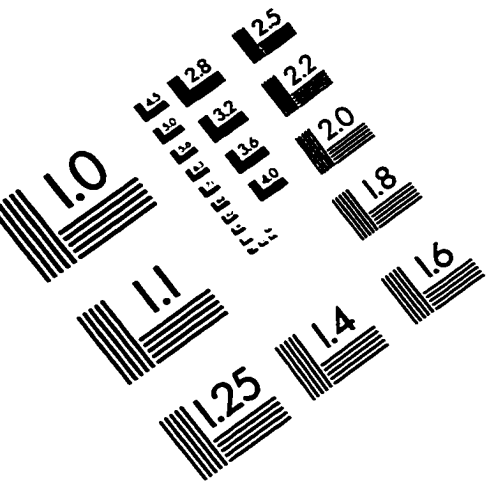
$$\nabla^2\phi = \frac{1}{h_1 h_2 h_3} \left[ \frac{\partial}{\partial x_1} \left( \frac{h_2 h_3}{h_1} \frac{\partial\phi}{\partial x_1} \right) + \frac{\partial}{\partial x_2} \left( \frac{h_1 h_3}{h_2} \frac{\partial\phi}{\partial x_2} \right) + \frac{\partial}{\partial x_3} \left( \frac{h_1 h_2}{h_3} \frac{\partial\phi}{\partial x_3} \right) \right] \quad (\text{G11})$$

$$\nabla^2\phi = \frac{1}{r} \left[ \frac{\partial}{\partial r} \left( r \frac{\partial\phi}{\partial r} \right) + \frac{\partial}{\partial \theta} \left( \frac{1}{r} \frac{\partial\phi}{\partial \theta} \right) + \frac{\partial}{\partial z} \left( r \frac{\partial\phi}{\partial z} \right) \right] \quad (\text{G12})$$

Equation G12 can be expressed as:

$$\nabla^2\phi = \frac{1}{r} \frac{\partial}{\partial r} \left( r \frac{\partial\phi}{\partial r} \right) + \frac{1}{r^2} \frac{\partial^2\phi}{\partial \theta^2} + \frac{\partial^2\phi}{\partial z^2} \quad (\text{G13})$$

# IMAGE EVALUATION TEST TARGET (QA-3)



APPLIED IMAGE, Inc  
1653 East Main Street  
Rochester, NY 14609 USA  
Phone: 716/482-0300  
Fax: 716/288-5989

© 1993, Applied Image, Inc.. All Rights Reserved

